



A review on Machine learning aspect in physics and mechanics of glasses

Jashanpreet Singh^{a,*}, Simranjit Singh^b

^a Mechanical Engineering Department, Thapar Institute of Engineering and Technology, Patiala 147001, Punjab, India

^b Department of Computer Science and Engineering, Bennett University, Greater Noida 201310, Uttar Pradesh, India



ARTICLE INFO

Keywords:

Glass
Glass design
Glass composition
Artificial intelligence
Machine learning

ABSTRACT

The glass science and technology is a rapidly developing field which is focused on development of new glasses with excellent properties. Glasses are the non-crystalline materials with inherent stoichiometry i.e. non-disordered structure of atoms and molecules, thus inherently unpredictable. The ineffective trial-and-error methods are typical to glasses design. The classical computational methods such as ab initio and classical molecular dynamics simulation techniques are costly, time consuming and provide limited data of results. To overcome from such problems, the machine learning (ML) replaces the classical experimental and simulation techniques to produce results more precisely. In the recent years, a lot of studies are carried out on AI to develop new compositions of glasses based on the different types of input parameters. Researchers developed new glasses by improving the various properties of glass like edge strength, shear strength, tensile strength, delamination, etc. In this paper, an effort has been made to explore recent developments in glass manufacturing and technology by the implementation of ML techniques. In this paper, the development of glass of new composition, prediction of glass properties, and various inspection methods are discussed on the basis of application of ML techniques.

1. Introduction

Glasses are the non-crystalline solids that take their shape while supercooled spontaneously [1]. Apart from crystals, there are no stoichiometry rules for the structure of glasses. These can be supposed of as continuous solutions of various elements. Every one of the elements of the periodic table may be melted down which is quite enough to be transformed into a glass [1]. A wide array of glasses can be produced in various compositions of chemical elements. For instance, eighty chemical elements added together at separate quantities of 1 mol% would be capable of producing 1052 potential forms of the glass [2]. Though, only about 106 types of organic glasses have been found, which suggests that a significant range of new glass-forming compounds may be recorded on in the future. Few typical types of glasses with applications are summarized in Table 1. Glass has a wide range of application in pharmaceutical science, construction, electronics, chemical, and automobile industry [3], as shown in Fig. 1.

Glass is a complex disordered substance and thus difficult to model with accurate prediction of state-dependent properties of glass e.g., liquidus temperature, dissolution kinetics, fracture toughness, etc. [4]. However, the use of “brute-force” atom-dynamics methods like molecular dynamics enabled the researchers to get the glass properties more

precisely and an alternate to the experimental methods [5]. Due to such considerations, the scope for utilizing these methods is constrained (e.g., shorter timescale, few atoms, high cooling rate, high computational cost), as the investigators unable to investigate all the possible outcomes in a comprehensive manner [5,6].

Glass science and technology is a rapidly developing field and passed through the physics based model, classical molecular dynamics (MD), ab initio MD, and implementation of machine learning on the traditional techniques. Fig. 2 shows the evolution of glass science and technology. From the perspective of glass science and technology, the artificial intelligence (AI) is a more advanced technology to predict the various properties and designing the glass. AI has reached almost all industries globally and is projected to revolutionise not just business, but also other civil, legal and medical disciplines, since it is a rapidly increasing technology. In this context, a literature review is carried out to enlighten the application of machine learning (ML) in the glass science and technology. In the following sections, the comprehensive review is presented which highlights the various researches conceded out in the area of glass science and technology.

* Corresponding author.

E-mail address: jashanpreet.singh@thapar.edu (J. Singh).

2. Historical background and description of molecular dynamics (Md)

In the early 1950 s, MD was established after previous Monte-Carlo simulations that dated back to the 18th century however, it was famous for statistical mechanics in the Los Alamos National Laboratory by Rosenbluth and Metropolis and recognised as Metropolis–Hastings algorithm at present [7,8]. In 1957, the IBM 704 machine was used by Alder and Wainwright [9] for simulating perfectly elastic collisions between the rough spheres. Gibson et al. [10] simulated the damage to solid copper by radiation with the use of a repulsive Born-Mayer contact form and a coherent surface force in 1960 (possibly the first practical simulation of matter). In 1964, Rahman [11] delivered liquid argon simulations using Lennard-Jones potential and device property estimates, for example the self-diffusion coefficient, well contrasted with experimental results. Molecular dynamics (MD) is a computer simulation tool for the analysis of physical atom and molecular activity [5]. Due to the fact that molecular systems are usually made up of several particles, the properties of such complex systems cannot be analytically determined; MD simulation by utilising computational methods circumvents this issue. Multicomponent glass has traditionally focused on costly and time-consuming trial-and-error experimentation to develop glasses with different properties and applications. However, Molecular dynamics (MD) simulation techniques are less time consuming, cost-effective, and widely used for designing the network structure of glass as well as give information (diffusion coefficients and vibrational density) which is thereby provide a more knowledge about glass forming materials.

2.1. Design constraints

The architecture of a simulation of molecular dynamics is required to represent the computing power available. In order for the measurement to be finished within a suitable time frame, optimal simulation dimensions (n) that denotes the no. of particles, time-step and overall time span needed to be chosen. However, the time ranges of the natural processes should be long enough to produce accurate results. The time period could correspond to the kinetics of the natural process in order to draw statistically relevant results from the simulations. Typical time spans used for MD simulations are nano- and micro-seconds (i.e. 10^{-9} s and 10^{-6} s respectively). The most CPU-intensive activity in classical MD simulation is to assess the potential according to the internal coordinates of the particles. The non-bound or non-covalent component of the energy assessment is the most expensive.

In Big O Notation, both pair-sided electrostatic and van der Waals interactions must be directly accounted for by the scale $O(n^2)$ of common molecular dynamics simulation. The cost of the computation can be minimised by using the electrostatic methods like Strong spherical

methods of cutting off $O(n)$, Ewald Particle Mesh i.e. $O(n\log(n))$ or Particle-particle-mesh (PPPM) [11]. The Coulombic interactions between atoms can be calculated by using particle–particle particle-mesh (PPPM) solver algorithm [6]. The size of the integration time-step (i.e. amount of time between potentials evaluation) is another aspect that affects the overall CPU time required by simulation. The time must be selected limited enough to prevent errors of discretion (i.e., less than the fastest vibrational frequency time in the machine). The classical MD has a typical time frame of 1 fs (10^{-15} s). This can be increased by the use of algorithms like the SHAKE constraint algorithm, which establishes the motions of the fastest atoms (for example, hydrogen atoms). There has also been the development of several time scale processes, allowing prolonged periods between the slower long-range forces updates [12].

An option between implicit [13] and explicit [14] solvents is needed to simulate molecules in a solvent. Explicit solvent particles must be measured at a higher cost using force field, while implicit solvents are calculated using mean-field approach [14]. An explicit scheme that requires approximately ten times the number of particles used in the simulation thus computationally costly. However, to replicate some properties of the solution molecules the granularity and viscosity of the explicit solvent is important. This is particularly important for the reproduction of chemical kinetics. The simulation box size must be wide enough to eliminate boundary conditions objects in all kinds of MD simulations. The use of periodic boundary conditions or fixing values on the edges (which can produce antiquities) is done to treat the boundary conditions [15]. In periodic boundary conditions, one direction of the simulation loop lay on the opposite side imitating a bulk stage is also handled by selecting the limit conditions which may produce antiquities too. In MD simulations, four types of ensembles can be adopted, discussed follows:

2.1.1. Microcanonical ensemble (NVE)

The mechanism is separated by variations in moles (N), volume (V), and energy (E) in the microcanonical ensemble [16]. It is a mechanism without heat exchange that refers to adiabatics. In NVE ensemble, an exchange of potential and kinetic energy (K.E.) with conservation of total energy may be considered as a microcanonical MD trajectory. The following first order differential equations can be written in newton notation for a system of N particles with coordinates (X) and velocities (v) [17]:

$$F(X) = -\nabla U(X) = M\dot{v}(t) \quad (1)$$

$$\dot{v}(t) = \dot{X}(t) \quad (2)$$

The particle coordinates (X) decided the potential energy feature of system i.e. $U(X)$. The initial equation comes from Newton's motion laws, which can be measured as the negative gradient ($U(X)$) calculated by using force (F) on the system. A symplectic integrator method can provide

Table 1
Nominal compositions of various glasses with applications [3].

Glass Type	Application	SiO ₂	Al ₂ O ₃	B ₂ O ₃	Na ₂ O	K ₂ O	MgO	CaO	PbO
Soda-lime glasses	Containers	66–75	0.7–7		12–16	0.1–3	0.1–5	6–12	
	Float	73–74			13.5–15.0	0.2	3.6–3.8	8.7–8.9	
	Sheet	71–73	0.5–1.5		12–15		1.5–3.5	8–10	
	Light bulbs	73	1		17	4	5		
	Tempered ovenware	75	1.5		14			9.5	
Borosilicate	Chemical apparatus	81	2	13	4				
	Pharmaceutical	72	6	11	7	1			
Lead glasses	Tungsten sealing	74	1	15	4				
	Colour TV funnel	54	2		4				23
	Neon tubing	63	1		8	6			22
	Electronic parts	56	2		4	9			29
	Optical dense flint	32			1	2			65

the location of each particle (X) and the velocity (v) at each point, for example, Verlet integration. Trajectory is referred to as a time evolution between X and v . By utilizing the original locations (theoretical knowledge) and velocities (randomized Gaussian), all the previous and future positions and velocities can be calculated.

The definition of temperature in MD is a common source of misunderstanding. The small amount of atoms used in MD simulations raises a temperature-related phenomenon. We usually have macroscopic temperature knowledge, which includes a large amount of particles however a temperature is referred as a statistical quantity. Where sufficient number of atoms exist, statistical temperature from the instantaneous temperature may be calculated, where n is the number of degrees of

freedom (DOF) of system by equating the K.E. of system with $nkBT/2$.

2.1.2. Canonical ensemble (NVT)

Substance (N), volume (V) and temperature (T) are preserved in the canonical ensemble. Often it is also called molecular dynamics at constant temperature (CTMD) [18]. In NVT, the energy is exchanged with a thermostat for endothermic and exothermic cycles. A number of thermostat algorithms are usable to add and subtract energy from the boundaries of the MD simulation which are more or less practical in their approximation to the NVT ensemble. Velocity rescale, Nosé–Hoover [19], Nosé–Hoover strings [20], Thermostat of Berendsen [21], Thermostat of Andersen [22], and Langevin dynamics [23] are common



Fig. 1. Application of various types of glasses.

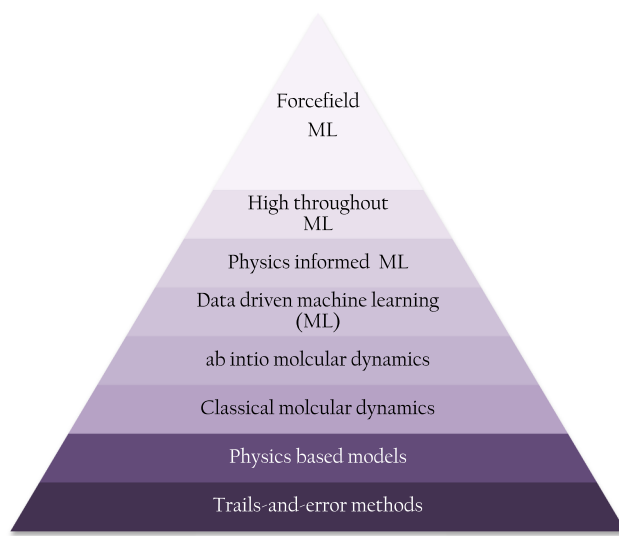


Fig. 2. Evolution of glass science and technology (bottom to top).

methods of temperature regulation. The NVT ensemble distribution of conformations and velocities with these algorithms is not trivial.

2.1.3. Isothermal-isobaric (NPT) ensemble

The quantity of material (N), pressure (P) and temperature (T) is preserved in the isothermal-isobaric ensemble [24]. A barostat is needed in addition to a thermostat. The lab environments with a flake open to atmospheric temperature and pressure are strongly corresponded to them.

2.1.4. Generalized ensembles

A generalized ensemble were originally developed to study the slow dynamics of disrupted spin systems have been developed [25]. It is also known as the replica exchange molecular dynamics (REMD) and parallel tempering. The REMD formulation attempts to solve the multiple minima problems by utilizing the temperature knowledge. The REMD serves the exchange of temperature between non-interacting replicas of system having the multiple temperatures.

2.2. Potentials in MD simulations

A MD simulation needs to define a possible purpose or the terminology under which the particles interacts in the simulation [26]. It is literally called the *potential* or the *force field* in science field of physics or chemistry, respectively. Potential may be described in several physical levels; those more widely found in chemistry are focused on molecular mechanics and represent a traditional mechanics treatment of the interactions of particles and may replicate structural and conformational modifications, but typically do not reproduce chemical reactions.

2.2.1. Empirical potentials (Force field)

Empirical potential used in chemistry is also referred to as ‘force fields’ whereas referred as ‘interatomic potentials’ in the mechanics of materials. Most force fields are empirically linked to chemical bonds, connecting angles and bond dihedrals, as well as unbonded forces related to van der Waals forces and electrostatic charging [27]. Empirical potential is a restricted representation of quantum mechanical effects through ad hoc functional approximations. They are made by fitting with the comprehensive electronic computations (i.e. quantum simulations) or experimental physical properties like elastic constants, grid parameters, and spectroscopic measurement parameters such as free parameters such as atomic charge, van der Waals parameters which represent estimates of the atomic radius, and equilibrium bond’s length,

angle, and dihedral [28]. Due to the non-local character of unbonded interactions, the weak interactions of all atoms of the system exist. The holdup of the pace of MD simulations is usually calculated. Force fields use numerical approximations including moved cut-off radii [29], Reaction field method [30], Ewald summation [29], or the new particle-particle particle-mesh (PPPM) [11] to reduce calculation costs. In reaction field method [30], the effective pairwise potential is given by:

$$U_{AB} = q_A q_B \left[\frac{1}{r_{AB}} + \frac{(\epsilon_{RF} - 1)r_{AB}^2}{(2\epsilon_{RF} + 1)r_c^3} \right] \quad (3)$$

In the above equation, symbol r_c represents the cut-off radius. The ϵ_{RF} represents the reaction field at the cavity centre which is given by:

$$\epsilon_{RF} = \frac{2(\epsilon_{RF} - 1)}{(2\epsilon_{RF} + 1)} \frac{\vec{M}}{r_c^3} \quad (4)$$

In the above equation, the symbol $\vec{M} = \sum \mu_i$ represents the sum of the dipole moment of molecules present in the cavity. The potential energy (P.E.) of molecule (i) also contribute at the centre of cavity which is equals to the $-1/(2\mu_i \cdot \epsilon_{RF})$. The torque acting on the molecule (i) is equals to the $\mu_i \times \epsilon_{RF}$.

2.2.2. Pair and many-body potentials

The potential functions of non-bonded energy are expressed as a total of interactions between the system’s particles. In several common force field areas the most convenient alternative is the “pair potentials,” in which the amount of the energy inputs between pairs of atoms can be computed to measure the total potential energy. Due to the reason, they are called “additive force fields”. For example, a Lennard-Jones potential [31] which is also termed the 6–12 potential. A non-bonded Lennard-Jones potential [31] is used to calculate the van der Waals forces, which is given by:

$$U(r) = 4\epsilon \left[\left(\frac{\sigma}{r} \right)^{12} - \left(\frac{\sigma}{r} \right)^6 \right] \quad (5)$$

The Born (atomic) model for the ionic grid is another case, an example is Columbus law [32]. In general, a simulation only contains the dipolar term, but also the quadrupolar term sometimes [33].

$$U_{ij}(r_{ij}) = \frac{z_i z_j}{4\pi\epsilon_0} \frac{i}{r_{ij}} + A_i \exp \frac{-r_{ij}}{p_i} + C_i r_{ij}^{-n_i} + \dots \quad (6)$$

In the above equation, the first term in the next equation is the rule of Coulomb for a pair of ions, and the second duration is the short-range repulsion described by the exclusion theorem of Pauli. In the above equation, while the value of n_i equals to the 6, this potential is referred as Coulomb-Buckingham potential [34]. In the case of many-body potentials, the P.E. accounts the influence caused by the mutual interactions of 3 or more particles whereas global pairwise interactions in the system also exist in case of pairwise potentials [33]. The theoretical energy of many-body potentials does not exist over pairs of atoms and these relations are directly measured as a combination of higher orders terms by explicit scheme. The dependence among the variables cannot generally be represented only with products of pairs of DOF in statistical terms. Examples of pair-wise potentials is Tersoff potential [35] which was initially used for carbon, silicon and germanium simulation and has since been used in a broad variety of other products, requires a total of 3 atom groupings with angles between the atoms as a significant factor in potential. Examples of many-body potentials are Tight-Binding Second Moment Approximation (TBSMA) potentials [36], embedded-atom method (EAM) [37], and the EDIP [35]. In the Ref. [35–37], a total of the contributions from the surrounding atoms is measured for the electron density of states in the area of an atom, and the contribution of potential energy then depends on the total number of the contributions.

2.2.3. Semi-empirical potentials

The semi-empirical potential, known as tightly bound potentials, is

large and varies depending on the atoms modelled [38,39]. The matrix representation of quantum mechanics is used for semi-empirical potentials. Matrix element values can thus be established using analytical formulas which estimate the extent by which specific atomic orbits are overlapped. The matrix is then diagonalized such that the occupation of the various atomic orbitals is established and mathematical formulas are again used to calculate the energy contribution of the orbitals.

2.2.4. Polarizable potentials

Polarizable potentials are the most classical implicit force-fields. These force-fields account the effects of polarisation by increasing the partial charges obtained by quantum chemical measurements [40]. The partial charges in relation to the atom's mass are stationary. But the MD simulations directly model the polarizability as induced dipole is introduced by using various approaches, including Drude particles or fluctuating charges. Dynamic redistribution of charge between the atoms that respond to the local chemical condition is possible in this way. Increased precision has been obtained for homogenous liquids like water by using polarisation [41,42].

2.2.5. Potentials in ab initio methods

A theoretical ground surface of P.E. is described as the area of force fields in classical MD. This is a significance of the Born–Oppenheimer approximation [43]. Electronic characteristic in excited states can be achieved by utilising a quantum mechanical technique, such as the density functional theory, where chemically reacts or where a more exact depiction is desired. It was named as Ab Initio Molecular Dynamics (AIMD). The computational costs of these simulations are far higher than traditional MD simulations due to their costs of handling the electronic DOF. This means the AIMD is restricted to smaller and shorter time spans. Mechanical and chemical techniques of the ab initio quantum methods can be used to quantify a fly system's P.E. as needed for trajectory conformations. In the immediate vicinity of the reaction coordination, this approximation is normally used. While different approaches may be used, they are dependent not but analytical fits but theoretical considerations. A large volume of knowledge, such as the density of electronic states or other electronic properties, is not accessible from analytical methods of the ab initio calculations. The opportunity to observe reactions involving the breaking or forming of covalent bonds, corresponding to different electronic states, is a major benefit of ab initio approaches. Furthermore, the ab initio methods enable recovery of effects over or beyond the approximation Born–Oppenheimer using techniques such as mixed classical quantum mechanics [43].

2.2.6. Coarse-graining (CG) and reduced representations

Instead of describing each device atom explicitly, “pseudo-atoms” are used to describe classes of atoms. However, the time scales of description are coarse-grained and lattice models. MD simulations on very large structures might need such large computing resources that conventional all-atom approaches cannot efficiently study them. Likewise, long time-scale simulations of processes (over 10^6 s), since they take such long measures, is prohibitively costly. Often the dilemma may be tackled by utilising decreased demonstrations, often called gross grain models [44]. Examples of CG methods are discontinuous MD (CG-DMD) [45] and Go-models [46]. CG models are widely used to examine a structure of biology, liquid crystal organization, and polymer glasses.

2.3. Long-range forces

This is a type of interaction in which doesn't increase over the value of r^d for a decrease of spatial interaction (d represents the dimensionality of the system) [47]. This type of example involves two types of molecular interactions that are used to demonstrate charge-charge and dipole–dipole molecular interactions. Physically simulating these forces poses a substantial challenge since they could stretch the box duration of half of the computational box from the thousands of particles. Instead of

double the box length, though, the brute-force technique will have a big impact on computing costs [48].

2.4. Molecular dynamics algorithms

2.4.1. Integrators and Short-range interaction algorithms

The commonly used integrators in MD are Symplectic integrator [49], Verlet–Stoermer integration [49], Runge–Kutta integration [50], Beeman's algorithm [51], and Constraint algorithms [52]. The short-range interaction algorithms include cell lists, bonded interactions, and Verlet list [49]. The data structure to locate all pairs of atoms inside a certain cut-off distance in MD simulations is called a cell list [53]. These pairs are used to calculate the short distant interactions in a system that are unbonded, for instance the Van der Waals forces or the short distance of the electrostatic interaction in the use of Ewald summation (Ref. [29]). A Verlet list is a molecular dynamic simulation data structure that efficiently keeps a list of all particles inside a defined cut-off space (named on Loup Verlet) list [49]. Verlet list approach can effectively be used for simulations of Monte Carlo. A cut-off radius, which is called ‘close-to-zero’ to be acceptable to ignore, is normally used for interacted within short-range interactions.

2.4.2. Long-range interaction algorithms

The long range interaction algorithms includes Ewald summation [29], Particle mesh Ewald summation (PME) [54], Particle–particle–particle–mesh (PPPM) [11], and Shifted force method [55]. Ewald summation was established well before the advancement of computers as a tool for theoretical physics. Since the 1970 s, the Ewald approach [56] has been widely used in the simulation of particulate systems using computers and particularly for the particles interact via the reverse square force law. Ewald summation [29] is the interaction potential which is given as:

$$\phi(r) = \overset{\text{def}}{\phi_{sr}(r)} + \phi_{lr}(r) \quad (7a)$$

$$E_{lr} = \frac{1}{\Omega} \sum_{m_1, m_2, m_3} \tilde{\Phi}_{lr}(k) |\tilde{\rho}(k)|^2 \quad (7b)$$

In the above equations, the sum of $\phi_{sr}(r)$ is quickly converges in real space and used as a short range term. The sum of $\phi_{lr}(r)$ is quickly converges in Fourier space and used as a short range term. The value of k is equals to the $m_1 b_1 + m_2 b_2 + m_3 b_3$ in the final summation. PPPM is a similar to the Ewald summation [29] but it is used to calculate potentials in N-body simulations. It is also called as Fourier-based Ewald summation method [56]. The Particle mesh Ewald summation (PME) was also recently used in the calculation of the Lennard-Jones potentials of the r^6 component to remove truncation objects [54]. Examples of PME simulations are galaxies, plasmas and molecules. The fundamental principle of the Ewald summation of particular mesh is to substitute the direct sum of energy interactions between particles.

$$E_{TOT} = \sum_{i,j} \phi(r_j - r_i) = E_{sr} + E_{lr} \quad (8a)$$

The E_{sr} is the direct sum of short range potentials in real space which is given by:

$$E_{sr} = \sum_{i,j} \phi_{sr}(r_j - r_i) \quad (8b)$$

The above equation represents the particle part of PME. The overall sum of Fourier space of the long-ranged potentials is given by:

$$E_{lr} = \sum_k \tilde{\Phi}_{lr}(k) |\tilde{\rho}(k)|^2 \quad (8c)$$

In the above equation, the $\tilde{\Phi}_{lr}$ the Fourier transforms of the potential and $\tilde{\rho}$ is the charge density (Ewald part). Since both summations converge very rapidly in their own real and Fourier spaces, the

computing time needed may be reduced with little loss of precision and a great improvement. In order for an effective evaluation of the Fourier transformation $\tilde{\rho}(k)$ in the charge density region, Fast Fourier is used. This means that the density field must be assessed on a discrete grid (this is the mesh part).

2.4.3. ab initio molecular dynamics

The ab initio molecular dynamics technique is also known as Car-Parrinello MD (CPMD). The Car-Parrinello system, introduced by Roberto Car and Michele Parrinello in 1985, is a form of MD that uses regular boundary conditions, planewave basis sets, and DFT. CPMD or Car-Parrinello approach is applied either to a process utilised in MD or to the software packages for computational chemistry [57]. The CPMD approach refers to the most general Born-Oppenheimer MD method (BOMD). In the computation of energy and forces for classical nuclei motion, the quantum mechanical influence of electrons is incorporated. For CPMD, the pseudopotential density function theory (DFT) is implementation, particularly for the purpose of initial molecular dynamics. CPMD uses electronic DOFs as dynamic constraints to explicitly discretise and expand the Lagrangian for the system that provides all ions and electrons with a system of combined motion equations. In this way, there is no need of explicit electronic minimizations at each point (i.e. time), as in Born-Oppenheimer MD, because the fictitious dynamics of electrons remain in the electronic ground state after initial normal electro-minimization, corresponding to each new ionic formulation visited along the dynamics, resulting in exact ionic forces.

The electronic density of the ground state fixed nuclei is automatically determined using the DFT. Then forces can be calculated with this density on the nuclei, to change the pathways using algorithm like Verlet integration [49]. Additionally, the trajectories for electronic (e^-) orbitals are determined in this sense, and the coefficients used to achieve the electronic orbital pathways may be viewed as an extra spatial dimension package.

Born-Oppenheimer MD (BOMD) form is an approximation to CPMD. The wave function of the electrons must be reduced at each phase of the pathway by diagonalization of the matrix. In order to hold electrons near the ground, CPMD uses fictitious dynamic [58], which prevents the need for costly autonomous iterative reduction at each stage. Fictional dynamics rely on flat masses of electrons (usually 400 to 800 AU) that confirm very little electron propagation, e.g. for adiabasis. The unit will leave the surface of the BOMD in the ground when the fictitious electron mass has risen. The expended langrangian equation for the system is given by:

$$L = \frac{1}{2} \left(\sum_I^{nuclei} M_I \dot{R}_{I+\mu^2} \sum_I^{nuclei} \int dr |\dot{\psi}_i(r, k)|^2 \right) - \left| \left\{ \dot{\psi}_i \right\}, \{R_I\} \right| \quad (9a)$$

In the above equation, the $E[\dot{\psi}_i(r, k)]$ represents the Kohn-Sham energy density function (EDF) [59]. Kohn-Sham EDF determines the value of energy according to the Kohn-Sham orbits and nuclear position. The orthogonality constraint is given by:

$$\int dr \dot{\psi}_i^*(r, t) \dot{\psi}_j^*(r, t) = \delta_{ij} \quad (9b)$$

In the above equation, the δ_{ij} represents the Kronecker delta [59]. The equation of motion is written as:

$$M_I \ddot{R}_I = -\nabla_I E \left[\left\{ \dot{\psi}_i \right\}, \{R_I\} \right] \quad (9c)$$

$$\mu \dot{\psi}_i^*(r, t) = -\frac{\delta E}{\delta \dot{\psi}_i^*(r, t)} + \sum_j A_{ij} \psi_i(r, t) \quad (9d)$$

In the above equation, the A_{ij} represents the Langrangian multiplier matrix to comply with the orthogonormality constraint.

3. Overview of classical approaches used for the development of new glasses

Researchers make much of their attempts to evaluate the properties of modern glasses by empirically-based simulations and only succeed in few predictions. However, a strong interest in designing better glasses with new and updated features is important in addressing some of the great challenges and difficulties [60,61]. In the context of glass development, the physics-based simulation can help to design different glasses. A variety of studies were performed on numerical simulations and experimental models to develop a variety of glasses on the basis of different properties (e.g., edge strength, hardness, stiffness, glass transformation or transition temperature, etc.) [3,60,62–65]. Most commonly used traditional approaches for the development of new glasses were trial-and-error experiments, classical MD, and ab initio molecular dynamics.

3.1. Experimental techniques applied in glass formation

Glass composition designers commonly used to measure the diffraction data in structure refinement methods such as RMC (Reverse Monte Carlo) [66,67] and EPSR (Empirical Potential Structure Refinement) [68]. The methods are used for the transformation of atoms in 3-D starting model to form configurations that match diffraction patterns, subject to imposed constraints including density measured number and incapability to overlap neighbouring particles and type and quantity of local physical units provided by spectroscopy experiments like nuclear magnet resonance (NMR), extended X-ray absorption fine structure (EXAFS), Raman spectroscopy, or etc. The use of additives and whiskers affects the crystallization of glasses so they are added to design the new composition of glass then tested the feasibility of glass formation by using spectroscopy techniques.

A typical example of new glass development with trial-and-error method by using $1\text{Li}_2\text{O} \cdot 1\text{Al}_2\text{O}_3 \cdot 4\text{SiO}_2$ is given in study [69]. Zandona et al. [69] studies the presence of $\text{TiO}_2(\text{B})$ nano-crystals in by annealing the three different aluminosilicate glasses like $1\text{Li}_2\text{O} \cdot 1\text{Al}_2\text{O}_3 \cdot 4\text{SiO}_2$, $1\text{Li}_2\text{O} \cdot 1\text{Al}_2\text{O}_3 \cdot (6.5\text{SiO}_2)$ and $1\text{Li}_2\text{O} \cdot 1\text{Al}_2\text{O}_3 \cdot 9\text{SiO}_2$. Around 4 mol% TiO_2 was used as nucleating agent in all compositions. They used Raman spectroscopy and transmission electron microscopy for the phase identification and found that the monoclinic $\text{TiO}_2(\text{B})$ appears after phase separation during the first stages of crystallization. Afterwards the temperature was gradually increased, the aluminosilicate glass undergo to a gradual transformation into anatase $\text{TiO}_2(\text{B})$ however, the Si enriched samples showed a long perseverance of anatase $\text{TiO}_2(\text{B})$. The anatase $\text{TiO}_2(\text{B})$ seen in Raman spectra (Fig. 3) confirmed the strong formation of the new glass. They also mentioned that the anatase $\text{TiO}_2(\text{B})$ disappeared in the volume crystallization done with the addition of high quartz and keatite solid solution. Sen et al. [70] investigated the effect of Al_2O_3 and Y_2O_3 on the $\text{Yb}_3 +$ luminescence and crystallization of $\text{P}_2\text{O}_5 \cdot \text{SrO} \cdot \text{Na}_2\text{O}$ glass. They used a standard melting method and $(95 - x)(0.50\text{P}_2\text{O}_5 \cdot 0.40\text{SrO} \cdot 0.10\text{Na}_2\text{O}) - 5\text{Yb}_2\text{O}_3 - x(1.5\text{Y}_2\text{O}_3 \cdot 2.5\text{Al}_2\text{O}_3)$ glass system (mol%). They mentioned that the both of these additives results in formation of highly configured phosphate network. Moreover, they mentioned that the increase in T_g and decrease in the glass crystallization rate with the addition of additives. Fig. 4 shows the SEM micrographs of the glasses post-heat treatment. SEM images depicts that there is absence of volumetric crystallization and the shape of large crystals seems like needles. However, the shape of crystals was observed independent of value x . it can be said the specific additives can be used to construct new glasses without disturbance of crystal shapes.

However, the essence of their structure makes RMC or EPSR models unavailable, i.e. refining methods do not have predictive ability in this context of particle dynamics, and because the modelling methods are guided by experimental evidence, they should not be utilised if this knowledge is inaccessible.

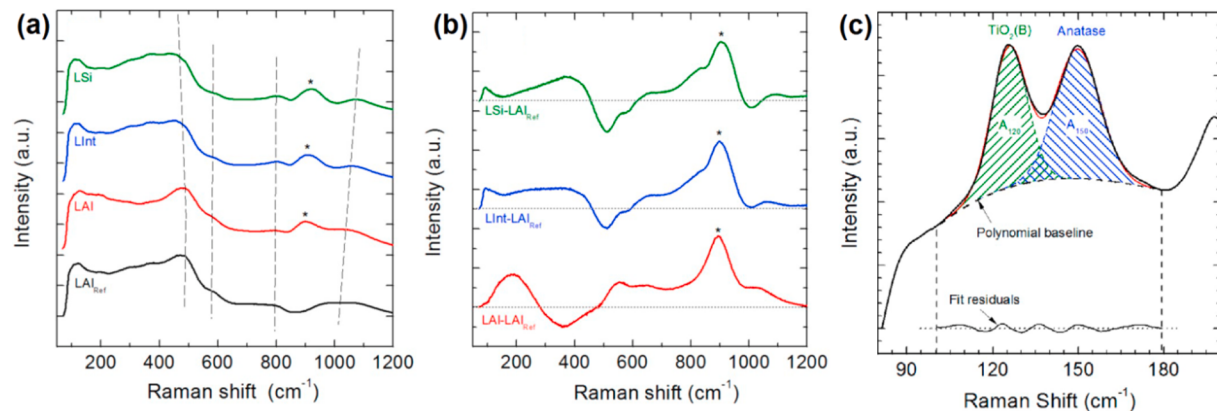


Fig. 3. Raman spectra of the untreated glasses (a) and after subtracting the spectrum of LAl_{Ref} from those of the three TiO₂-bearing samples (b), and Hatched lines mark the main bands associated with the aluminosilicate glassy network, while asterisks (*) flag the most intense Raman feature associated with Ti[IV], playing the role of a network former, and (c) Result of the fitting procedure applied to the Raman spectrum of sample LSi, after “ramp” ceramization to 825 °C [69] {Permissions under ©Creative Commons CC-BY license}.

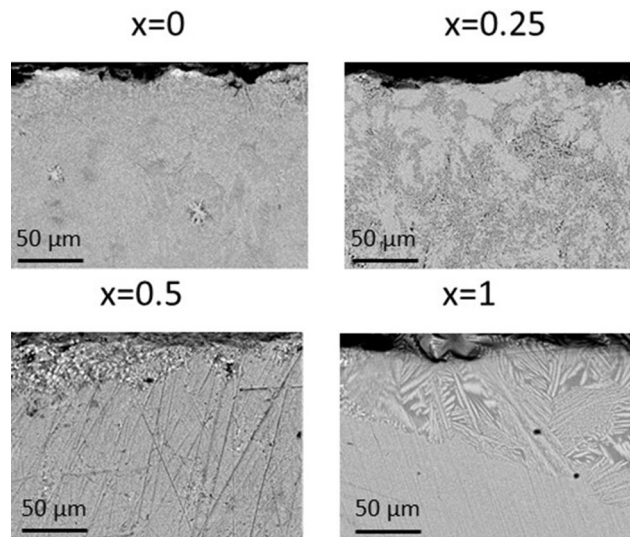


Fig. 4. SEM micrographs of the cross-section of the glasses heat treated at crystallization temperature (T_p) = 40 °C for 1 h [70] {Permissions under ©Creative Commons CC-BY license}.

3.2. Molecular dynamics (MD) applied in glass formation

Glass composition with few elements (i.e. < 5) can be solved with analytical computational methods such as *ab initio* and *classical molecular dynamics*. Various studies performed by the MD simulations are summarised in Tables 2a and 2b. In this section, classical MD techniques used for the prediction of the structure and properties of various glasses is discussed. The commonly used tool for the MD simulations is Large-scale Atomic/Molecular Massively Parallel Simulator (LAMMPS) package [6,71]. Li et al. [6] used MD simulation by using the Teter potential to predict the structure of sodium silicate glasses and studied the effect of cooling rate. The MD simulation showed a good agreement mentioned that the experimental data, as shown in Fig. 5. They used the pair distribution function i.e. neutron pair in order to compare the neutron diffractions of simulated and experimental data of glass, as given by:

$$g_N(r) = \left(\sum_{i,j=1}^n c_i c_j b_i b_j g_{ij}(r) \right)^{-1} \sum_{i,j=1}^n c_i c_j b_i b_j g_{ij}(r) \quad (10)$$

In the above equation, the $g_{ij}(r)$ is the partial pair distribution functions, c_i and b_i are the fraction of i atoms and neutron scattering length of

the species respectively. The subscript $i = \text{Na}, \text{Si}, \text{or O}$ and the value of $b_i = 3.63, 4.1491, \text{ and } 5.803 \text{ fm}$ for Na, Si, and O atoms, respectively. The structure of the glass was simulated by using Fourier transformation of the partial pair distribution function. The partial structure factors $S_{ij}(Q)$ was computed by:

$$S_{ij}(Q) = 1 + \rho_0 \int_0^R 4\pi r^2 (g_{ij}(r) - 1) \left(\frac{\sin(Qr)}{Qr} \right) F_L(r) dr \quad (11a)$$

$$F_L(r) = \frac{\sin(\pi r/R)}{\pi r/R} \quad (11b)$$

In the above equation, the Q , ρ_0 , and R is the scattering vector, average atomic number density, and half of the simulation box length, respectively. To decrease the effect of the finite cutoff of r , the Lorch-type window function ($F_L(r)$) was used in the integration [72]. Equation 2a is simplified into the total neutron structure factor, as given below:

$$S_N(Q) = \left(\sum_{i,j=1}^n c_i c_j b_i b_j g_{ij}(r) \right)^{-1} \sum_{i,j=1}^n c_i c_j b_i b_j S_{ij}(Q) \quad (12)$$

3.3. Density function theory

Atta-Fynn et al. [73] used the *Ab initio molecular-dynamics* (AIMD) simulations to optimize the atomic structure of Ni₄₀Pd₄₀P₂₀ glass. They used density functional theory (DFT) code SIESTA for performing the subsequent geometry relaxations. They used a ball and stick model of Ni₄₀Pd₄₀P₂₀ glass is given in Fig. 6(a). Fig. 6(b-e) shows that the simulated structure of Ni₄₀Pd₄₀P₂₀ glass matches the ideal structure. This was also confirmed form the results data, as shown in Fig. 6(f). The static structure factor $S(q)$ was calculated for the position of the atoms in the network:

$$S(q) = \frac{\left\langle \sum_{j=1}^N \sum_{k=1}^N f_j(q) f_k(q) \exp(-1q \cdot r_{jk}) \right\rangle}{\sum_{j=1}^N (f_j(q))^2} \quad (13)$$

In this equation, $\langle \cdot \rangle$ indicates the rotational averaging of magnitude (q) over a solid angle of 4π for $N = 10$ configurations, r_{jk} represent the position of vector r_k and r_j , f_j represents the atomic form factor of the j^{th} atom, q is wave-vector transfer of magnitude. The atomic form factor value of q was calculated by the Gaussian approach:

$$f_j(q) = \sum_{j=1}^N a_j \exp\left(-b_j \left(\frac{q}{4\pi}\right)^2\right) + c \quad (14)$$

Table 2a

Molecular dynamics (MD) simulation techniques applied to the glasses.

S. No.	Technique	Simulation tool and theory	Materials	Results	Ref.
1	MD simulations	<ul style="list-style-type: none"> LAMMPS package Particle-particle particle-mesh (PPPM) solver algorithms 	Sodium silicate glass: $(\text{Na}_2\text{O})_{30}(\text{SiO}_2)_{70}$	<ul style="list-style-type: none"> Structure and properties bond angle 	[6]
2	<i>ab initio</i> MD simulations (AIMD)	Density functional theory (DFT) code SIESTA package	$\text{Ni}_{40}\text{Pd}_{40}\text{P}_{20}$ glass	<ul style="list-style-type: none"> Ideal atomic structure Bonds and pairs 	[73]
3	Classical MD simulations	<ul style="list-style-type: none"> Temperature dependent topological constraint theory (TCT) $2\langle r \rangle_3$ rule 	$x\text{Na}_2\text{O} 0.1 \text{CaO} (0.89-x) \text{B}_2\text{O}_3 0.01 \text{Fe}_2\text{O}_3$ glasses (Soda lime glass)	<ul style="list-style-type: none"> Glass hardness 	[65]
4	Classical MD simulations	Mauro-Gupta topological constraint theory (TCT)	Borate glass (B_2O_3) + 65 mol% of L_2O	<ul style="list-style-type: none"> Glass transformation temperature (T_g) 	[74]
5	Classical MD simulations	<ul style="list-style-type: none"> Topological constraint theory (TCT) LAMMPS package PACKMOL package (for atom placing) 	Silicate ($\text{CaO-Al}_2\text{O}_3-\text{SiO}_2$) glass system	<ul style="list-style-type: none"> Young's modules Stiffness 	[64]
6	Combined <i>ab initio</i> MD & classical MD simulations	<ul style="list-style-type: none"> <i>ab initio</i>: Car-Parrinello (CP) MD 	Silica glass	<ul style="list-style-type: none"> Bond angles Structure Potentials 	[75]
7	<i>ab initio</i> MD simulations + classical MD	<ul style="list-style-type: none"> Van Beest-Kramer-van Santen (BKS) empirical potential function DFT density functional theory Topological constraint theory (TCT) 	Amorphous silica	<ul style="list-style-type: none"> Energy density difference Pair distribution Bond angles Dissolution kinetics Effect of Mg modifier 	[76]
8	Classical molecular dynamics (MD) simulations and vertical scanning interferometry (VSI)		Glassy aluminosilicates		[77]
9	Classical MD simulations	Topological constraint theory (TCT)	Aluminoborate glasses	<ul style="list-style-type: none"> Chemical durability Field strength Structural properties 	[78]
10	Physics based theory	FIRE algorithm	Kob-Andersen Lennard-Jones glass		[79]
11	Physics based theory	Radial density function	Super cooled liquids	<ul style="list-style-type: none"> Heterogeneous activation Local structure Softness 	[80]
12	<i>ab initio</i> MD simulations	Atomistic computer simulations	Multi component oxide glasses	<ul style="list-style-type: none"> Development of Boron oxide potentials 	[26]
13	Classical MD	LAMMPS package	Calcium Aluminosilicate	<ul style="list-style-type: none"> Structure Vibrational Elastic (role of potential) 	[81]
14	<i>ab initio</i> MD simulations	Vienna <i>ab initio</i> package (VASP) /Kohn-Sham (KS) formulation of the DFT	Oxide glasses	<ul style="list-style-type: none"> Optimization scheme to obtain interaction potentials 	[82]
15	MD simulations	LAMMPS package	Borosilicate glass	<ul style="list-style-type: none"> Potential Structure Shear viscosity 	[71]
16	<i>ab initio</i> MD simulations	CPMD simulation	Amorphous silica	<ul style="list-style-type: none"> Potentials 	[83]
17	MD Simulations	CPMD simulation	Silica	<ul style="list-style-type: none"> Effective potential 	[84]

Table 2b

Commonly used loss functions for the validation of models.

S. No.	Model name	Equation	Equation No.	Ref.
1	Log loss	$L = -\frac{1}{N} \sum_{j=1}^N \log(p_j)$	6	[97]
2	Mean Square error (MSE)	$MSE = \frac{1}{N} \sum_{j=1}^N (O_j - p_j)^2$	7	[97]
3	Mean absolute error (MAE)	$MAE = \frac{1}{N} \sum_{j=1}^N O_j - p_j $	8	[117]
4	Mean Absolute Error Root Mean Square Error (RMSE)	$RMSE = \sqrt{\frac{1}{N} \sum_{j=1}^N (O_j - p_j)^2}$	9	[117]
5	Coefficient of determination (R^2)	$R^2 = 1 - \frac{E(S)}{T(S)}$	10	[118]
6	Mean absolute percent error (MAPE)	$MAE = \frac{1}{N} \sum_{j=1}^N \left \frac{ O_j - p_j }{p_j} \right $	11	[97]

Value of N is the total number of observations, p_j represents the predicted values, O_j represents the original values, and $E(S)$ is the sum of squares of the errors, and $T(S)$ is the total sum of squares.

In the above equation, a_j , b_j , and c are atom-type specific empirical constants.

3.4. Topological constraint theory (TCT)

TCT has shown itself to be a powerful tool for the explanation of amorphous behaviours. The theory predicts a transformation between a rigid over-constrained network and a loose under-constrained network (i.e. floppy network) on the basis of connectivity or average value of coordination number i.e. $\langle r \rangle$ [86]. TCT has been very effective in terms of describing and forecasting actions in covalently bonded networks is one of the several theories postulated for *ab initio* systems [87,88]. According to the models proposed by Phillips and Thorpe [88], the mechanical properties of amorphous glasses were explored to comprehend the atomic constraints [89]. Researchers [88,89] demonstrated that rigidity can be measured from the constraints of degree of freedom (DOF) in the amorphous network and constraints of bond-stretching and -bending forces. Rigidity is determined by the network's coordination no. $\langle r \rangle$ and DOF approaches to the dimensionality of amorphous network. The TCT model can predict the rigidity transition at a critical $\langle r \rangle$ in 3D covalent networks while DOFs equals the number of atomic constraints by a threshold (-2.4) between a floppy and rigid network [90]. In the application of glasses, Smedskjaer et al. [65] used the temperature dependent topological constraint theory for the quantitative prediction of hardness in $x\text{Na}_2\text{O}-\text{CaO}(0.01\text{Fe}_2\text{O}_3(0.99-x)\text{B}_2\text{O}_3$ (i.e.

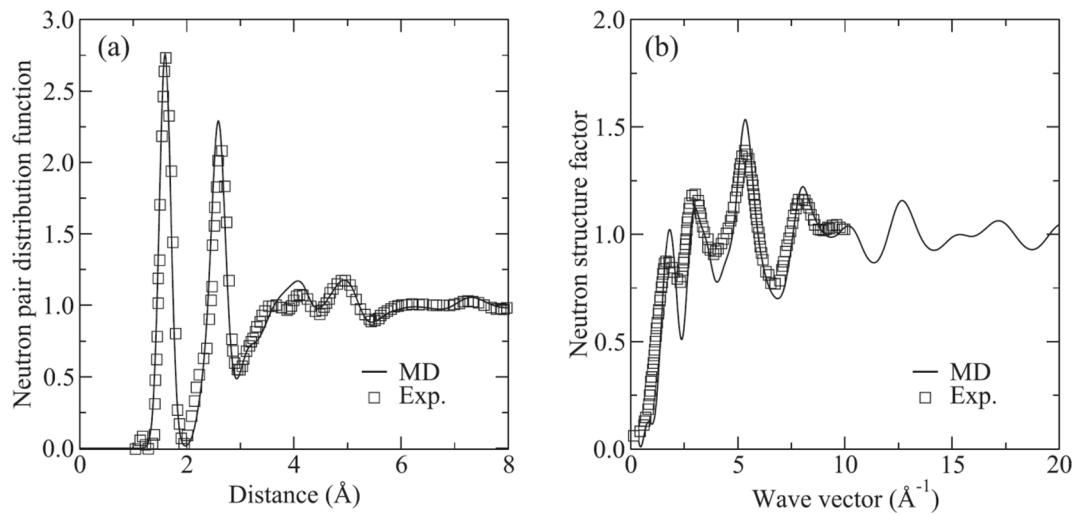


Fig. 5. Experimental vs. MD computed results of (a) neutron pair distribution function and (b) structure factor of a $(\text{Na}_2\text{O})_{30}(\text{SiO}_2)_{70}$ glass prepared [Cooling rate = 0.01 K/ps] [6] {Permissions of ©Elsevier}.

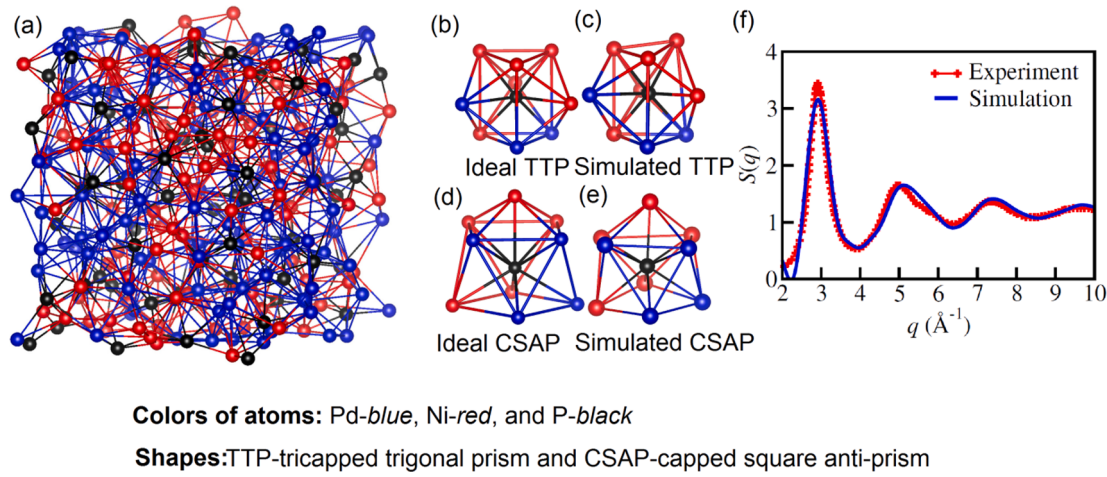


Fig. 6. (a) A ball-and-stick representation of a 300-atom model of Ni₄₀Pd₄₀P₂₀, (b, c) Comparison of P-centered ideal TTP geometry with a distorted version from simulations, (d, e) Comparison of P-centered ideal CSAP geometry with a distorted version from simulation [73], (f) A comparison between the experimental data from differential scanning calorimetry measurements at 313 K by Lan et al. [85] and static structure factors of Ni₄₀Pd₄₀P₂₀ between from AIMD simulations at 300 K by Atta-Fynn et al. [73] {Permissions under ©Creative Commons CC-BY license}.

soda lime borate) glass systems. They calculated the average atomic no. of constraints at a room temperature ($T < T_g$) and stretching constraints were assignment to O in order to ease the calculation. The bond bending constraints yields were calculated by 2(r)-3 rule, given by:

$$n(x, y) = 5N(B^4) + 3N(B^3) + 3N(O) + \frac{4x}{2x + y}N(M^{NB}) \quad (15)$$

In the above equation, the symbols N(B⁴), N(B³), N(O), and N(B^{NB}) represents the fractions of 4-coordinated boron, 3-coordinated boron, Oxygen (i.e. bridging and nonbridging varieties), and network modifiers (Na and Ca that create nonbridging O), respectively. Symbol μ represents the constraints. The hardness of soda lime glasses was predicted by using following equation:

$$H_v(x, y) = \left(\frac{dH_v}{dn} \right) [n(x, y) - n_{crit}] = \left(\frac{dH_v}{dn} \right) [n(x, y) - 2.5] \quad (16)$$

In this equation, the $dH_v = dn$ is the proportionality constant and its value is determined from the load of the indenter. This model showed good agreement with the experimental data, as seen in Fig. 7(a, b). The results of H_v and T_g are shown in Fig. 7(c, d).

Mauro et al. [92] proposed a correlation for the calculation of glass transformation temperature (T_g) and fragility of alkali borate glasses. The model equation for T_g calculation is given by:

$$\frac{T_g(x)}{T_g(x_R)} = \frac{f[T_g(x_R), x_R]}{f[T_g(x), x]} = \frac{d - n[T_g(x_R), x_R]}{d - n[T_g(x), x]} \quad (17a)$$

$$n(T, x) = \sum_i N_i(x) \sum_\alpha w_{i,\alpha} q_\alpha(T) \quad (17b)$$

$$q_\alpha(T) = \theta(T_\alpha - T) \quad (17c)$$

In the above equations, the value of d was taken as 3 that denotes the dimensionality of the network and $n(T, x)$ represents the average no. of constraints per atom. Numbers of constraints per unit node of network were evaluated by taking types of constraints (α) and an average of overall network structuring species (i). Symbol $q_\alpha T$ represents the information about cooling rate dependence of the glass transition. Symbol $w_{i,\alpha}$ is the number of α -type constraints related to species. The mole fraction of network structuring species (i) is denoted by $N_i(x)$. Fragility in terms of $f(T,x)$ is evaluated by using following equation:

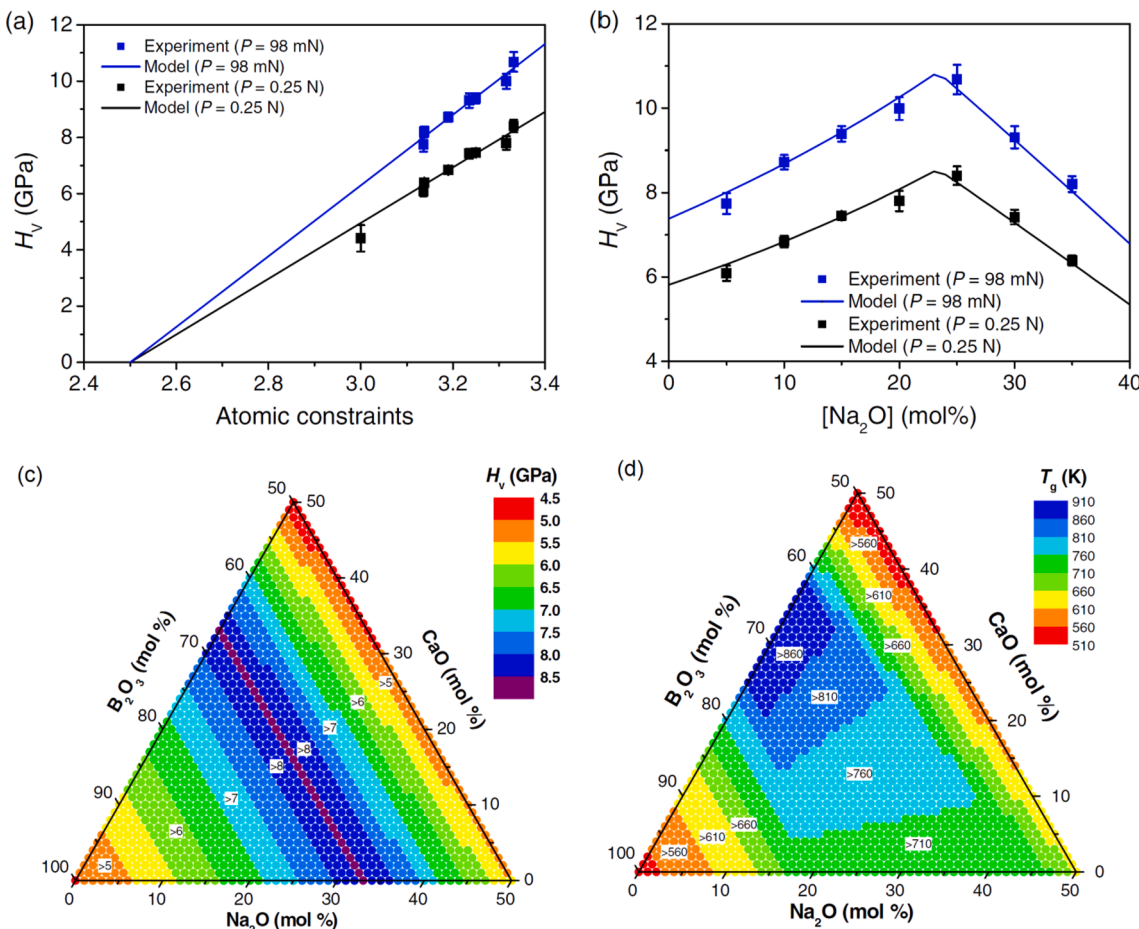


Fig. 7. (a, b) Measured Vickers hardness (H_V) at two different loads (98 mN and 0.25 N) with respect to [(a) average number of atomic constraints for $T < T_g$ and (b) concentration of Na_2O in the $xNa_2O_yCaO_0.01Fe_2O_3(0.99-x-y)B_2O_3$. $\{dH_V/dn\}$ was calculated as 12.6 and 9.9 GPa for $P = 98$ mN and 0.25 N, respectively], (c) Model predicted (a) $H_V(x, y)$ at a $P = 0.25$ N, and (d) $T_g(x, y)$ [91] for $xNa_2O_yCaO_0.01Fe_2O_3(0.99-x-y)B_2O_3$ glass system {Permissions of ©APS Physics}.

$$m(x) = m_0 \left(1 + \frac{\partial \ln f(T, x)}{\partial \ln T} \Big|_{T=T_g(x)} \right) \quad (17d)$$

Takeda et al. [74] used a Mauro-Gupta topological constraint theory (TCT) to predict the glass transformation temperature (T_g) based on atomic structure. TCT model is given by:

$$\frac{T_g(R)}{T_g(R_r)} = \frac{S_c[Tg(R_r), R_r]}{S_c[Tg(R), R]} \quad (18)$$

In this equation, the S_c and R_r are the configurational entropy and reference composition respectively. By following the Feller model, they predicted T_g for borate glass (B_2O_3) by adding the 65 mol% of Li_2O . They mentioned that by the addition of the structure of B_2O_3 changes (i) the formation of non-bridging O atom in 3-coordinated B atoms and (ii) conversion of coordinates of B from 3D to 4D with a -ve charge. The atomic structures predicted by the MD simulations are given in Fig. 8(a-d). For the validation purpose, they compared the Mauro-Gupta TCT model with the Mauro model proposed by Mauro et al. [92], modified Mauro model without the assumption of μ constraints and Affatigato and Feller experiments for T_g done by Koritala et al. experiments [93] for Li^+ molar ratios. They computed the following correlation for the transition temperature of glass:

$$T_g(R) = \frac{f[T_g(0), 0]}{f[T_g(R), R]} T_g(0) \quad (19)$$

In the above equation, $T_g(0) = 533$ K. The proposing model showed the R^2 as 0.8672, as seen in Fig. 8(f). By using the Mauro et al. [92] and

Smedskjaer et al. [65] models, Yang et al. [64] proposed a new model for predicting the young's modulus. They used the statement of hardness, according to which, hardness is a linear function of the number of constraints (n_c) per atom. They simulated the volumic density of bond-bending (BB) and bond-stretching (BS) constraints with respect to change in composition of the $CaO-Al_2O_3-SiO_2$ glass system, as seen in Fig. 9.

4. Basics of Machine learning (ML)

Machine learning (ML) offers a new way to leverageable dataset data-driven methods for the exploration of novel glasses in the areas of physics-based simulation. A significant achievement of the AI and ML techniques is the development of new glasses. Focusing on structural glass, numerous projects have been undertaken like switchable glass, including sun protection [94], time and temperature-related material behaviour in polymeric layered glasses in context of undamaged and post-failure glass [95]. Machine learning is beneficial in terms of analysing the vast collections of existing data and understanding the configuration of data which is not possible by human [96]. Schematic view of the broad range area of the artificial intelligence and its similarities between various fields is illustrated in Fig. 10 [97].

Machine learning is similar to statistics (e.g., regression models), patterns recognition (e.g., structure failure analysis), data mining (e.g., composition analysis models, CNNs), and Knowledge Discovery in Databases i.e. KDD techniques. Fig. 11 presents a schematic sketch of typical ML application in glass science and technology. Firstly, a dataset is generated by conducting the actual experiments, simulation or mining

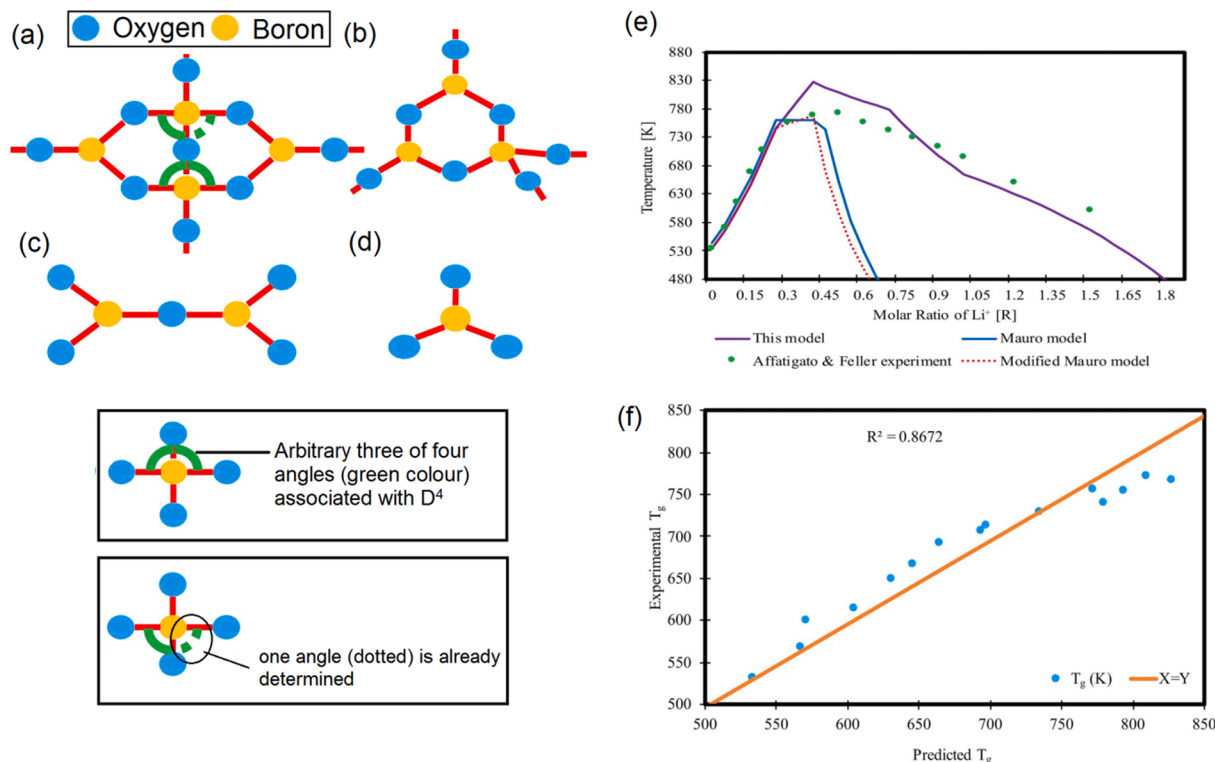


Fig. 8. (a-d) Atomic structure [(a) Diborate ring includes two 4-coordinated borons (D^4) and two 3-coordinated borons (D^3), (b) represents triborate ring with two T^3 and one T^4 , (c) is the combination of three-coordinated boron with two N-B-Os (P^3), namely pyroborate. (d) three-coordinated boron with three N-B-Os (O^3) namely orthoborate], (e) Comparison of Li^+ molar ratios between Takeda et al. [74], Mauro model proposed by Mauro et al. [92], modified Mauro model without the assumption of μ constraints and Affatigato and Feller experiments for T_g done by Koritala et al. [93] experiments, and (f) is experimental versus Takeda et al. [74] model predicted T_g . {Permissions under ©Creative Commons CC-BY-NC-ND license}.

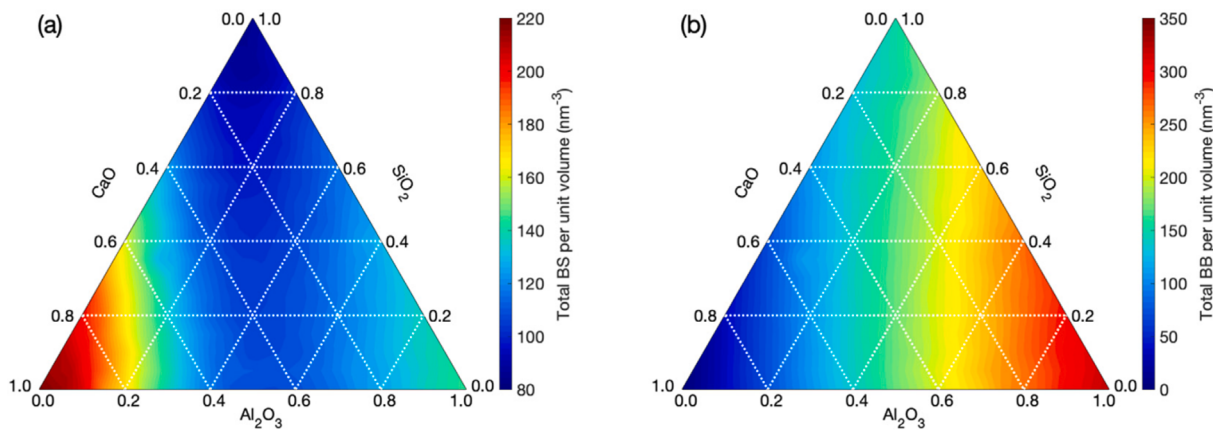


Fig. 9. Simulated volumic density of (a) bond-stretching (BS) and (b) bond-bending (BB) constraints with respect to change in composition of the CaO-Al₂O₃-SiO₂ glass system [64]{Permissions of ©Elsevier}.

in order to perform the ML technique. The dataset has a set of individual inputs e.g., glass composition, density, hardness, etc. Thus, a database containing properties (components or substances) can provide glass composition, synthesis process, or other details. Once correlations have been developed inside the dataset, then the ML is used to build a predictive model [96]. However, the machine learning algorithms are of two kinds supervised and unsupervised ML. The detailed discussion on supervised and unsupervised ML techniques is done in next sections. The supervised learning uses the regression and classification models whereas the unsupervised learning utilises the clustering models for the prediction of results. The use of AI ML techniques involves a number of key steps that one have to follow for the prediction of accurate results.

ML application involves the functional steps like problem formation, data, model and loss function, data splitting, and under/over-fitting. The detailed discussion on these functional steps is given in next sections. Data, algorithms and models used in machine learning are discussed follows.

4.1. Problem formulation

Prediction models are foundational to functional applications of AI, where a model is characterized as a defined collection of distinct rules applied to the AI algorithm to guide it to learn by itself [98]. The computer program learns with respect to a certain set of tasks and is

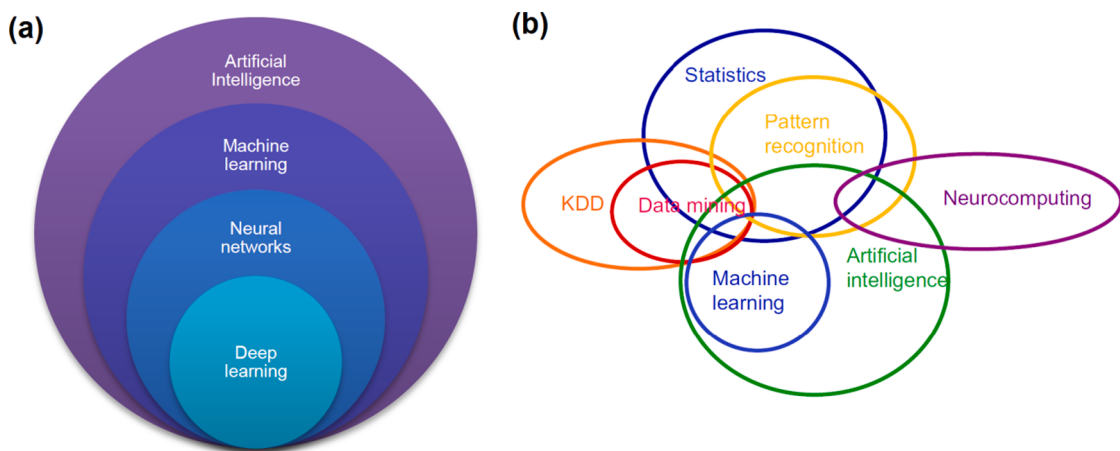


Fig. 10. Schematic view of (a) the broad range area of the artificial intelligence, and (b) similarities between various fields [97] {Fig. 10(b)'s permissions by ©Elsevier B.V.).

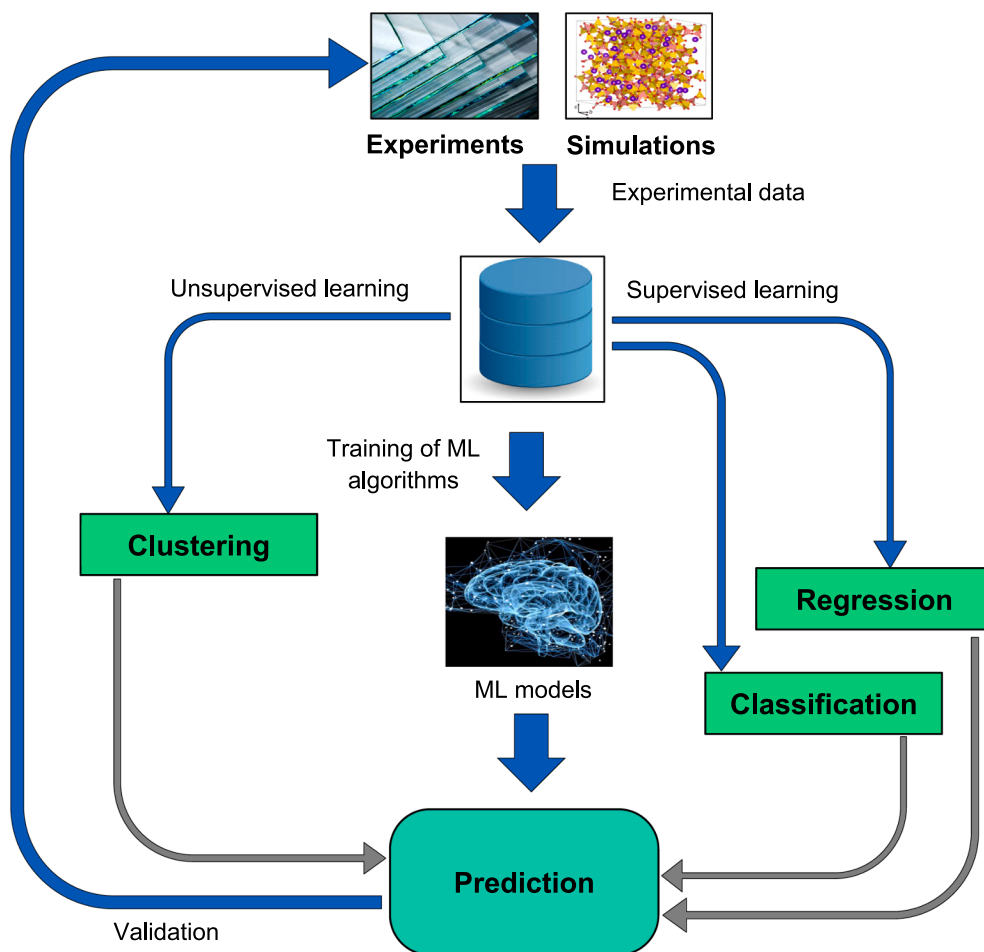


Fig. 11. Schematic sketch of ML application in glass design.

more proficient with respect to other tasks. This spectrum covers a lot of interactions and activities, and it's tolerant of a variety of success metrics. However, in this article, activities of varying complexity and supervised learning with specific examples are discussed. Finally, we have also discussed the effect of assignment and performance. The features of a data point is defined as \times which belongs to R^n which denotes the n -dimensional space [99,100]. These features are referred to as independent variable in linear regression. These features belong to a specific

class which is called as targets. These defined features are given as input to various AI algorithms, which is able to find the relations between the features and the targets. The prediction models are built with the help of training the neural network. By using hyperparameter tuning, the performance of the prediction model can be increased. Other techniques namely L2 regularization also help in building an effective AI prediction model [101].

4.2. Dataset

For processing the dataset effectively, it should be refined and pre-processing techniques like normalization and standardization should be performed [98–100,102–105]. Studies [98,105] listed the following for characterizing a dataset: *variety, value, volume, velocity, and veracity*. The three characteristics of “variety, volume and velocity” applicable on data creation, capture and storage process, the accuracy and use of the data to the task in question are characterized by the “veracity” and “value” aspects and are thus vital to obtain handy and relevant knowledge from the input. In the case of a certain expansion of all five definitions of the suggested list, the term “big data” is satisfied, which for this publication is of partial importance. Technically speaking, “big data” refers to massive, complicated volumes of knowledge requiring “intelligent methods” to process it. Structured data are the knowledge that has a predefined data model, i.e., the position of each data part and the material is accurately known [98,105,106]. Semi-structured data referred to as kind of structured data that does not adhere to the organizational framework of tables or data structures, but nevertheless separates structural components into identifiable components, and attributes into hierarchies [98,106]. There is data that does not fit into predefined structures, or does not have structure [98,106]. Organized data include databases stored in the form of tables, while images and videos should be in the form shown in Fig. 12.

Additionally, several notes on field-of-use details for structural glass engineering applications are eventually addressed about the data structure. On this particular area, data is thought of as being either a structured, semi-structured and unstructured data. In next section, it is defined how quantitative data from unstructured data in photograph forms are used to check the consistency, and quality. The structured data extracted from mechanical investigations and simulations are used to distinguish trends and model parameters to assist in quality control. It is shown in literature that an accurate and relevant mix of data and structure results in effective solution [98–100,102,103]. Numerical engineering relies on exploratory data mining in the development of various simulations, especially in the sense of glass engineering [98,108,109]. There is a wide range of outcomes obtained when constructing models to help in structural glass engineering, and there is a significant gap in price between the different methods that are applied to the spectrum of results and the whole dataset consists of only a few observations. Nevertheless, for a finite element simulation, the feature and goal numbers are usually high. This will enable hardware requirements and feature decisions to be made in experimental strategy. Most statistical data sets only contain a few observations due to cost problems and design problems with the experiments [110,111]. For functional implementations of ML, a decision must be made based on the essence of the problem and the assignment and the variety, veracity and

volume of data required on a case.

4.3. Identification of key inputs and reduction of dimensionality

Mostly, though for structured data is fairly straightforward [104] however for unstructured data the generation of features is critical and this phase is called feature engineering [96]. The data dimensionality in general can be managed by employing current highly effective algorithms, but many features can create complexity consequently it is considered the curse of dimensionality [98–100]. To fix the problem, feature selection and dimensional reduction techniques can be employed. More information is presented in the previous works [104,112]. Feature engineering is a significant way in supervised and unsupervised learning to identify the relevant key inputs (glass structure, temperature during annealing, etc.) [96]. Variable factors that have the greatest effect on the performance of system must be identified by user. This is called function engineering, which may be extended from to either an interpretation of the problem or the observed effect i.e. the statistical correlation analysis between input and output [113]. In actual, one can eventually identify the relevant inputs and measure their features by using evaluation technique such as the correlation matrix calculation [113]. Even, there are several input variables that may be used for each point of data, and such high-dimensional input spaces would be counterproductive for machine learning models in terms of computational efficiency [114]. Dimensionality reduction techniques like Non-negative factorization (NMF) [115], Linear discriminant analysis (LDA) [114], and Principal component analysis (PCA) [114] can be used to assist in the training of the model to overcome from the expletive dimensionality [116]. In brief, this concept of using these methods is to use various existing sources of input information to create informative inputs and substitute any of the original input sources [96,114]. To that is the manner in which it is possible to integrate multiple inputs into one model dimensions metrics, these strategies can improve the computing ability or efficiency of machine learning model. Assuming the need of effective machine learning, an input requires more than 5 points for training purpose. As the dataset volume increases, the no. of data points in the training set also increases i.e. dimensionality. Moreover, this increase is related to the type of machine learning algorithm, and the expected property.

4.4. Model and loss function

We refer to assignment ‘T’ when describing how an AI is expected to process data points. A role of assignment *T* is to label research specimens in order to assess their intactness or loss. Often, a success in the task assessment measure *P* is a reasonable indicator for how effectively an AI algorithm will operate on the particular task at hand. Efforts to improve

		Dataset of fractured glass			
Properties		Dataset			
		Point 1	Point 2	Point N
Fracture area		P_{11}	P_{12}	P_{1n}
Fracture thickness		P_{21}	P_{22}	P_{2n}
Fracture height		P_{31}	P_{32}	P_{3n}
Desired strength		P_{m1}	P_{m2}	P_{mn}

Fig. 12. Typical examples of the (a) unstructured data [107] and (b) structured data{Permissions of ©Elsevier}.

classification precision as previously defined in example may be considered “a potential measure” [102–104]. Setting the correct success measures is much more complicated than just applying a formula to a set of criteria. As this paper focuses data science scenarios, the assignment T pertains to using models only. When dealing with the performance measure P , the AI does a new math model that improves performance over time. This gain computed by P is achieved by (numeric) optimization, which can render P the “objective, loss or cost function” in alternative nomenclature in ML or DL contexts. This article uses the notation for an objective function i.e., a statistical perspective, a function that we want to minimize or maximize [102,103]. In particular where an AI algorithm’s mathematical model has parameters and learns from data set training (or short: data) K , this is formulated as a minimal cost function M :

$$\alpha = \operatorname{argmin} M(\theta|K) \quad (20)$$

Where, $\operatorname{arg min}$ represents the minimum argument.

The commonly used loss functions for the validation of models are listed in Tables 2a and 2b. The loss function is essential to modeling, and has a major impact on the performance [98,102,103]. For various assignments, several loss functions are always yield multiple optimum parameters, but it is difficult to decide the option of loss function to use prior to beginning a simulation exercise whether or which ones would be better.

4.5. Data splitting

After data cleaning and visualization, various AI models are contrasted against each other. The goal of glass designer is to obtain a well-working ML model with a significant general-purpose knowledge of the extracted data [102,103]. There should be a close overall match with previously unknown results, but the final model must be able to make predictions. Inadequate generalization effects will arise from overfitting the model’s previously learned data [98–100,102,103]. Two distinct and interrelated problems are known as the Bias and Variance [98]–[100]. There are some different approaches for evaluating models [101] are leave-one-out cross validation (LOOCV) [112], k-cross validation [95], holdout [119] and stratified K-fold cross validation [97].

4.6. Underfitting and overfitting

Underfitting meant from the lower complexity in model. The model doesn’t adequately explain the connection between the input variables and the device performance. By comparison, to combat overfitting dataset “noise” is remembered [120]. As it comes to models, a common rule of thumb is that the complexity of the build model is quantified by the sum of numeric value that are other than 0., the total

inputs, and the amount of words used [96]. Fig. 13 shows over and underfitting by learning (i.e., training collection, refer to the sections below) Thus, the interaction between input and output in this example cannot be captured by a linear model of $p = 1$. A model with $p = 15$ is adequate to describe random data points in the training set, which means it has little predictability for outlying points that don’t have been tested (i.e. validation set). A polynomial regression model having $p = 3$ can represent the general pattern of the results, although excluding noise from the dataset may not provide enough statistical power.

4.7. Training, validation, and test sets

A dataset is normally segregated into training, validation, and testing set to elude overfitting and to assess the model accuracy [97]. Modelling is done by training the model with training examples. At this stage, the model is unable to distinguish between training and test data and test results. After that, the model is re-trained on the validation range, which further fine-tunes its sophistication. So long as the model can handle more complicated input data, additional detail (higher p in this case) generally leads to better interpolation, although at the cost of decreased capacity to predict the training set, as seen in Fig. 14. Overall, the highest balance of difficulty is achieved when the validation set includes the fewest number of potential solutions [120]. Finally, in order to achieve the optimum amount of sophistication, the test set uses a fraction of the data points that is unfamiliar to the model as the goal.

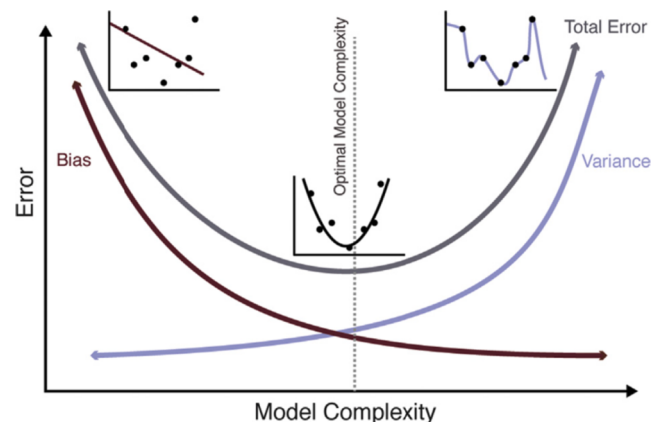


Fig. 14. Errors versus model complexity (optimal model shows lowest complexity and bias) [122] {Permissions of ©Elsevier}.

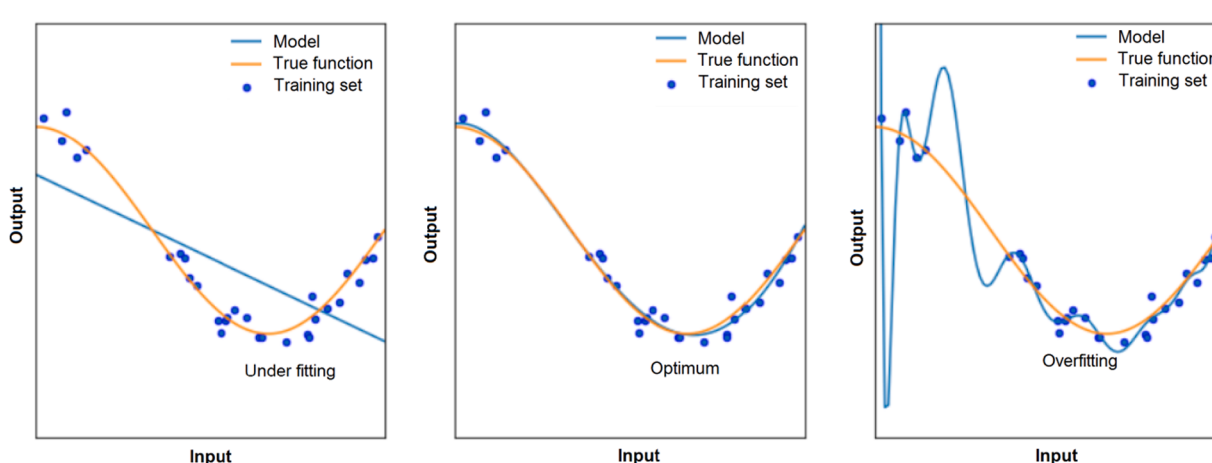


Fig. 13. Illustration of underfitting, optimum, and overfitting [121] {Permitted by authors to cite as a permission}.

4.8. Cross-validation

In practical scenarios, dataset size is minimal and leave so much of the data unnoticed can impede the model training. This can be solved by the use of validation methods. Hyperparameter tuning and model selection can be addressed by using cross validation (CV). CV is a mathematical methodology used to estimate the generalizability of the results [101]. One-way validation method of any dataset is to use holdout the training and test set at a fixed value [98,102,103]. While using the very large samples, it is appropriate to apply the holdout method [101], as shown in Fig. 15(a). However, three-way validation has advantages even in spite of that fact. In the three-way holdout strategy, more preparation datasets can be found [99,100,123]. To guarantee that the whole data set is from the same distribution, all data should have an equal frequency distribution. Some typical quantization of data amounts [98–100].

While the problem seems very difficult, this can be solved by the use of k -fold cross-validation method or k -CV (partitioning data into k subsets and testing each against each other, where we depend on k -CV) [95]. Similarly, each group of samples is evaluated using a k -fold cross validation has only has one criterion, k . This way, it is sometimes called as k -fold validation. Fig. 15(b, c) shows two typical k -fold cross validation methods namely leave-one-out cross validation (LOOCV) for total

k samples and k -fold forward cross-validation (k -fold FCV). It partitions the training into k iterations, and training is performed on $k-1$ of the folds, and validation is performed on the remaining folds. It is repeated k times until each validation set. The model's overall accuracy is calculated by taking the mean of the results on all k validation folds.

4.9. Methods of regularization

An alternate means of minimizing the difficulty of a model consists of filtering non-important modelling words that can be done by regularization methods [120] such as, for example, LASSO [125], Ridge [126] or Elastic Net [120,127]. A costing feature, consisting of (i) ability of the model to forecast established data and (ii) supplementary concept, which imposes a penalty on complicated models, is the key concept of regularisation. This reduction of the cost feature results in a nil reduction of non-important words (i.e., that do not substantially increase the precision of the model). The degree to which the model's sophistication can be adjusted can be determined by changing the punitive weight to ensure an optimum prediction of the validity range [128].

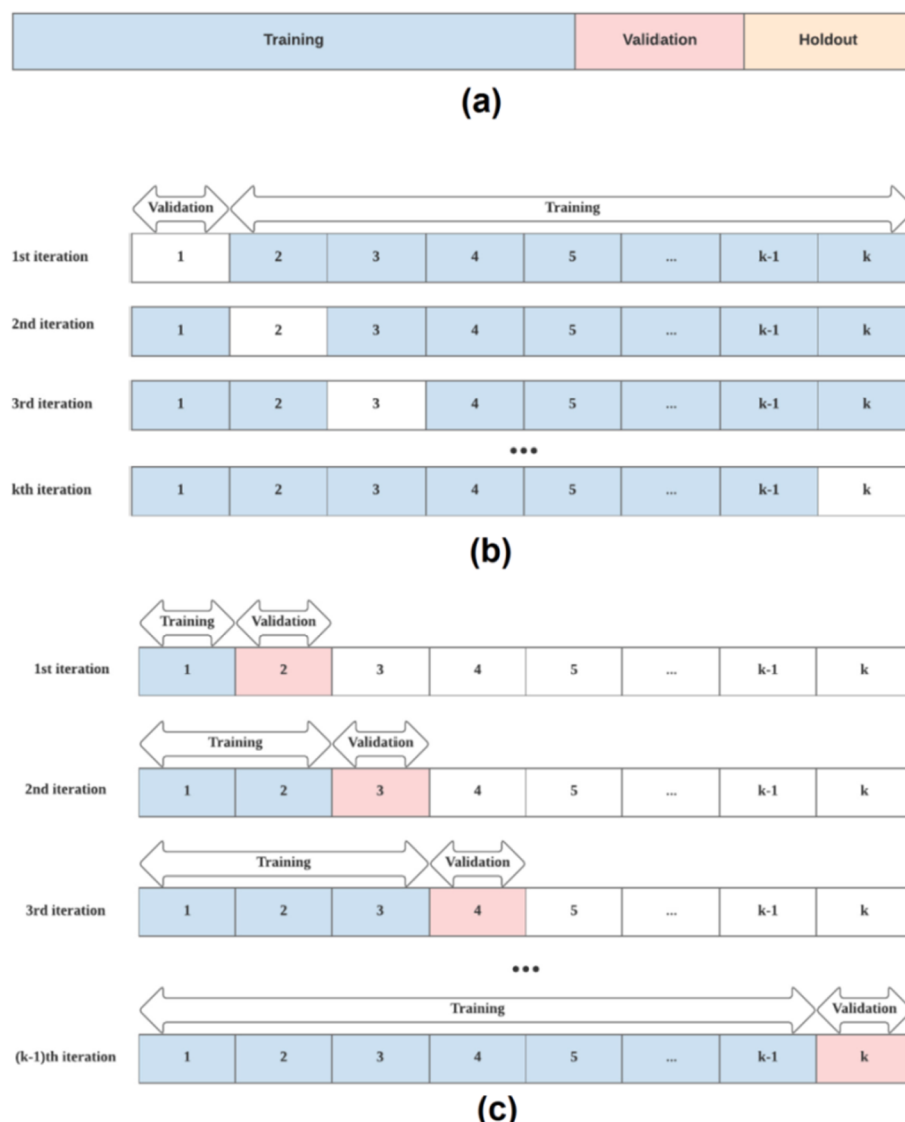


Fig. 15. Evaluation methods used in ML techniques (a) hold-out method (b) leave-one-out cross validation (LOOCV) for total k samples (c) k -fold forward cross-validation (k -fold FCV) [124] {Permissions of ©Elsevier}.

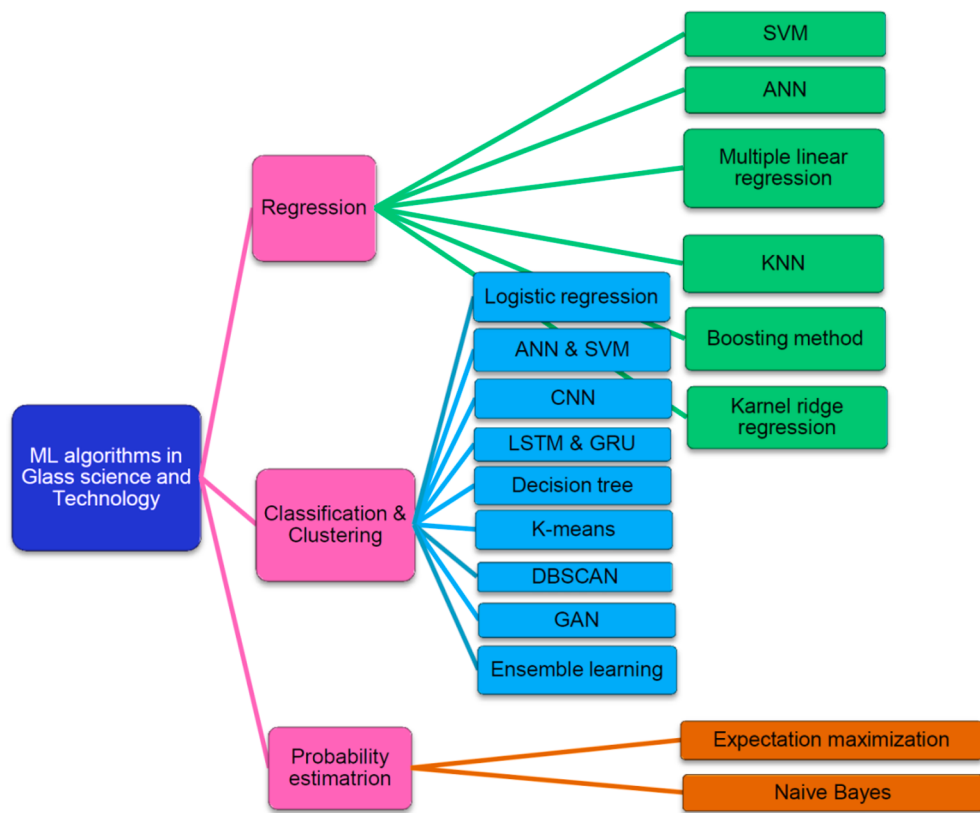


Fig. 16. Various types of ML techniques used in glass science.

4.10. ML algorithms

ML techniques are divided into three categories namely regression, classification & clustering, and probability estimation which are further divided into different subcategories as shown in Fig. 16. The best and validated ML algorithm is selected on the basis of the lower percentage of error. The machine learning methods are validated and underfitting/

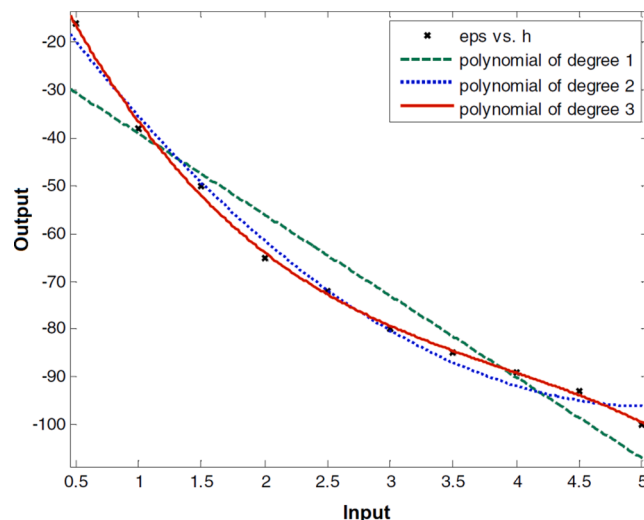


Fig. 17. Example of the polynomial regression model applied to the data points (eps vs. h), dotted lines represents the degree (p) of polynomial model (for green line, $p = 1$, for blue line, $p = 2$ and for red line, $p = 3$) [138] {Permissions under ©Creative Commons CC-BY-NC-ND license}. (For interpretation of the references to color in this figure legend, the reader is referred to the web version of this article.)

overfitting is avoided.

4.10.1. Regression techniques

The interaction between inputs and outputs can be evaluated by regression [129]. For a more detailed analysis see the Fig. 17, which illustrates how regression models will learn from a dataset [129] (e.g., linear [130], polynomial [131], or nonlinear functions [132]). In parametric regression, output is calculated using the input variables, whereas in nonparametric regression is provided by a kernel function for nearby points [133].

One other representation of a nonparametric regression is the k-nearest neighbours (KNN) approach [134,135]. The fundamental principle for the KNN approach is to estimate the output for a certain input location by employing the k value which is calculated taking the mean of the nearby points of the input position. However, a typical GPR approach [136] perform calculations for each input location the Gaussian-type probability distribution dependent on the multi-variant normal association between the input location and all other established points [115] — in that the degree of correlation decreases depending on the distance between them [136]. The GPR approach is able to provide substantial benefits in terms of volatility of the expected performance values, which is important for determining the predictions' reliability [137].

Parametric regression, unlike nonparametric regression, is focused on an explicit analytical formulation involving inputs and outputs of problem [129], in which the components of the formulation have been modified in accordance with familiar points and objective function (cost) is described and minimised. It should be remembered that more sophisticated machine learning algorithms can be used for classification and regression.

Except for kernel-dependent functionality [139], for example, artificial neural network (ANN) [140], support vectored machine (SVM) [141], random forest [142] and gradient boosting [143] basically are

based on complicated nonlinear parametric formulas. These types of models have also been quite effective in interpolating data [143], but the complicated organization of the parametric formula [140] and restricted hypothesize ability [144] are typically poor in interpretation. The phases of studying models and making projections generally are: (i) preparation and (i.e., configuring and validation) and (ii) evaluation. In the fitting or learning process, it is important to modify the complications of the model to give accurate predictions (e.g. the maximum degree of polynomial regression) [145,146]. The stepwise procedure to optimize the model complexity is listed below.

4.10.2. Classification techniques

Specific case of regression may be regarded as classification [147]. In classification problems the model is trained on the features (input) and classes (output), while each condition refers to separate groups of classes, unlike in a regression, when the output value is constant. In binary classification there are only two classes. The output can either belong to Class 1 or Class 2. The trained model are formed in the end has the capability to classify the features in classes on which the model is trained (for example, glass is transparent or not transparent, glass composition, etc.). The optimum hyperground in the input area that better separates the various groups may be achieved by defining (see Fig. 18) [147,148]. Fig. 18 shows the linear and linear non-separable case classifier. The straight lines shown in Fig. 18(a) represent a linear hyperplane for a set of training data (x_i) is written as:

$$w^T + b = 0 \quad (21a)$$

The above equation accounts data of $i = 1, 2, 3, \dots, n$ points. In the above equation, w and b represents the n -dimensional vector and bias term respectively. The hyperplane used for linear separable case accounts two criteria (i) there should be least percentage of error in separation data and (ii) distances between clustered (class) data must be maximal [148]. In this case, the classes are classified by means of boundary i.e. left ($y = 1$) and right ($y = -1$) sides of the hyperplane. Therefore, the separation is controlled in following manner:

$$w^T + b \begin{cases} \geq 1 & \{y_i=1\} \\ \leq -1 & \{y_i=-1\} \end{cases} \quad (21b)$$

However, the optimal classification depends on distance (ξ_i) between the bad classifier which can be minimized by penalty function (Fig. 18b), given by:

$$F(\xi) = \sum_{i=1}^N \xi_i \quad (21c)$$

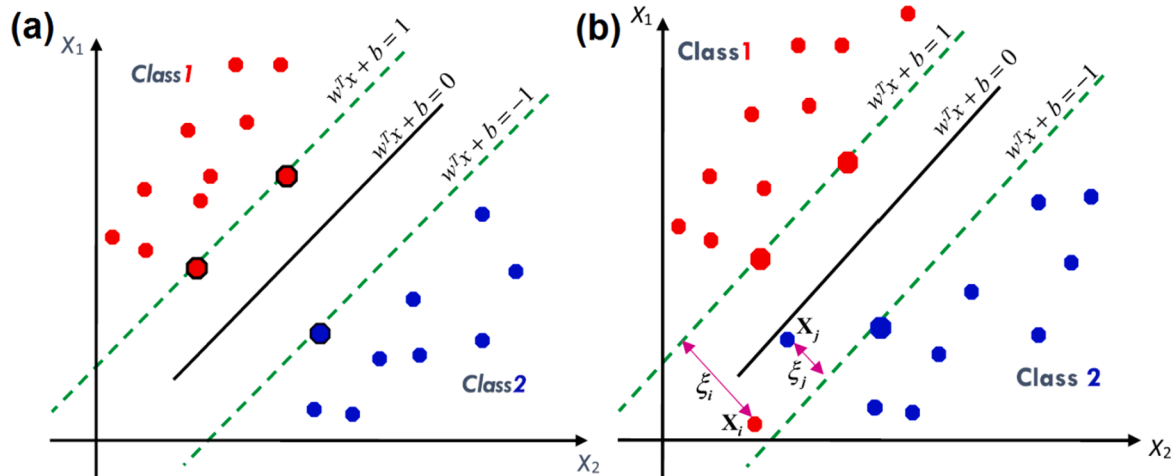


Fig. 18. (a) Support vectors (bold points) showing the maximum margins from each class of linearly separable data, and (b) slack variables defined to minimize the error of misclassification of linearly non-separable data [148] {Permissions of ©Elsevier}.

A term ‘classification accuracy (CA)’ enables to evaluate the model for the classification problems [116].

$$CA = \frac{S}{N} \quad (22)$$

In the above equation, the symbol S is the no. of correctly classified samples and N is the total number of samples.

4.11. Supervised machine learning algorithms

Given known example [149], the supervised ML discovers the association by making sense of input features with discrete or continuous output. It also covers regression algorithms which generates the results based on the inputs e.g., compositional models [129] that identify classes of glasses e.g., automatic classifiers [147] that assign the appropriate mark to each one. Here, the label of the data is lacking (i.e., the label is missing).

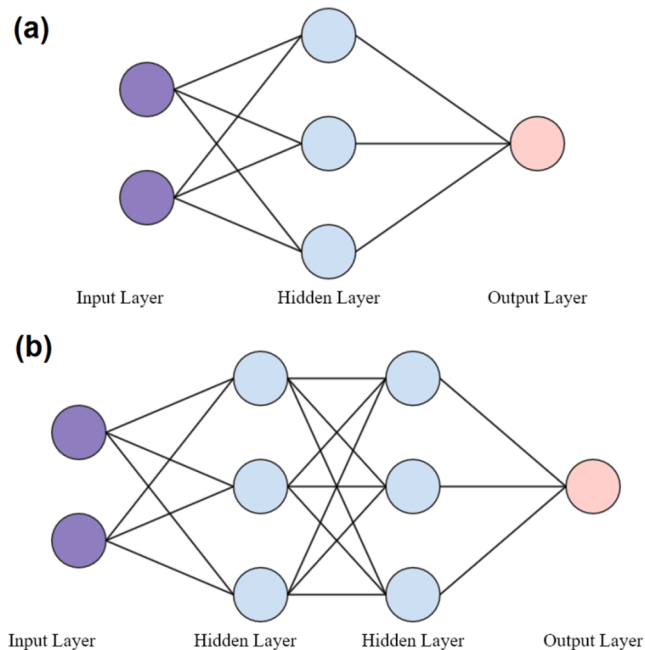
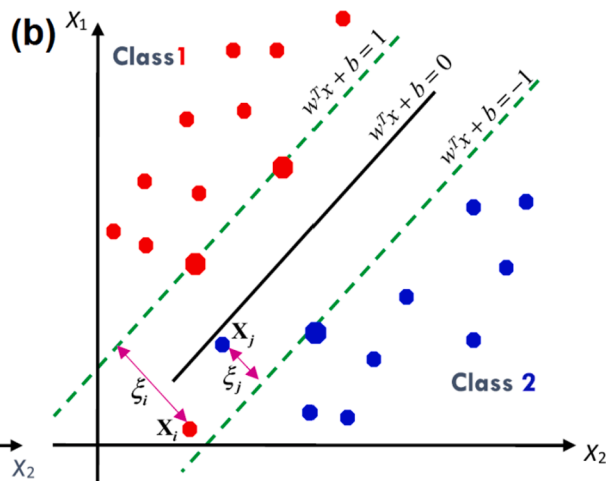


Fig. 19. Structure of the ANN model with (a) one hidden layer, and (b) multiple hidden layers.



4.11.1. Artificial neural network (ANN)

ANN is the network of neurons which are arranged in such a way that it imitates the human characteristic of learning. Neurons are connected to each other via edges. The weight is assigned to these neurons and edges which changes as the learning process happens. A simple ANN with one hidden layer is shown in Fig. 19(a). It has input, hidden and output layer. The obtained output in the end is compared with the actual output and based on the difference weights are adjusted which contribute to the learning process. However, ANN with multiple layers is also employed to solve many problems. More hidden layers increase the number of parameters which takes more time to solve the problems. That is why this network arrangement is used to solve complex problems. ANN with multiple hidden layers is shown in Fig. 19(b).

4.11.2. Recurrent neural network (RNN)

Recurrent Neural Network (RNN) is a class of artificial neural network which typically form meaningful connections in the temporal domain and takes sequential data as input. It performs better on the sequential data when present inputs depend on the previous. A typical RNN is shown in Fig. 20. Theoretically, RNN can be used to remember long term dependencies, but in practice, it cannot be able to learn it due to the problem of vanishing gradient [150].

4.11.3. Support vector machine (SVM)

The architecture of a SVM model is illustrated in Fig. 21(a). The Linear SVM [141] classifies problems by mapping features into groups using a hyperplane, and a kernel hyperplane [151–153] separates features by mapping details to a subclass, as shown in Fig. 21(b). It uses straight lines to segment the input space into distinct regions, which is precisely the form of mathematical feature of the linear SVM models. The linear functions are computed by seeking the coefficients that maximizes the separation or margin on each hyperplane's side [141]. The employed kernel describes correlation between feedback and test positions (i.e., known class). In this case, the equation produces non-linear hyperplanes for classification so that to have the maximum volume of space for maneuver [151–153].

4.11.4. Long Short-Term Memory network

Long Short-Term Memory Network (LSTM) [155] is the extended form of RNNs, as shown in Fig. 22 that solves the problem of vanishing gradient. It is best suited for sequential problems like stock prediction, signal analysis, time series, speech analysis, etc. The presence of forget gate in LSTM enables it to selectively remember a degree of the previous information due to which it easily maintains long term as well as short term dependencies. The gate operations are:

- o Input operation: $P_t = \sigma(e_p \cdot [U_{t-1}, k_t] + a_p)$ (23a)
- o Forget operation: $O_t = \sigma(e_o \cdot [U_{t-1}, k_t] + a_o)$ (23b)
- o New candidates: $N_t = \tanh(e_N \cdot [U_{t-1}, k_t] + a_N)$ (23c)
- o Cell state: $S_t = O_t \circ S_{t-1} + P_t \circ N_t$ (23d)
- o Output operation: $Q_t = \sigma(e_Q \cdot [U_{t-1}, k_t] + a_Q)$ (23e)
- o Next hidden state: $U_t = Q_t \times \tanh(S_t)$ (23f)

Where \circ is the Hadamard product, e is the weight assigned, symbol a is the bias, t is the present state, σ and \tanh are the activations employed.

4.11.5. Gated Recurrent unit (GRU)

GRU is another category of RNN which is very similar to LSTM as they both works well with the sequential input. The difference lies in the number of gates. It has less gate operations as compared to LSTM and the new gates operations are update and reset. Due to low number of operations GRU is able to perform the same task faster as compared to LSTM. It is show in Fig. 23. The gate operations are:

- o Update operation: $pd_t = \sigma(e_{pd} \cdot [U_{t-1}, k_t] + a_{pd})$ (24a)
- o Reset operation: $es_t = \sigma(e_{es} \cdot [U_{t-1}, k_t] + a_{es})$ (24b)
- o Candidate activation: $N_t = \tanh(e_N[est \circ [U_{t-1}, k_t] + a_N)$ (24c)
- o Next hidden state: $U_t = (1 - pd_t) \circ U_{t-1} + pd_t \circ N_t$ (24d)

Where pd_t and es_t denotes the update and reset operation.

4.11.6. Convolutional neural network

Nowadays, the concept of ANN evolved from MLP [156] into advanced deep convolutional neural network [153], are based on an input multiple layer configuration consisting of a hidden structure, and a single output. Convolutional Neural Network (CNN) is a class of neural network which forms meaningful connections when image data is given as input. It is similar to the human brain in that it has several layers, which emulate the connectivity of the nervous system. Activation functions such as sigmoid function connects the signal from the previous layer's neurons to an answer signal sent to the neurons of the subsequent layers. The relationship between inputs and outputs is a fluid, non-linear functional mapping [149]. CNN can able to learn spatial and temporal dependencies if the filters are exploited properly. A convolution operator [157] is performed by placing the relevant filter on an image and adding the multiplication of the coincided values of filter and image values. The filters can be placed directly on images. CNN can learn and classify images [158]. The application of CNN applied to detection of glass fracture is shown in Fig. 24.

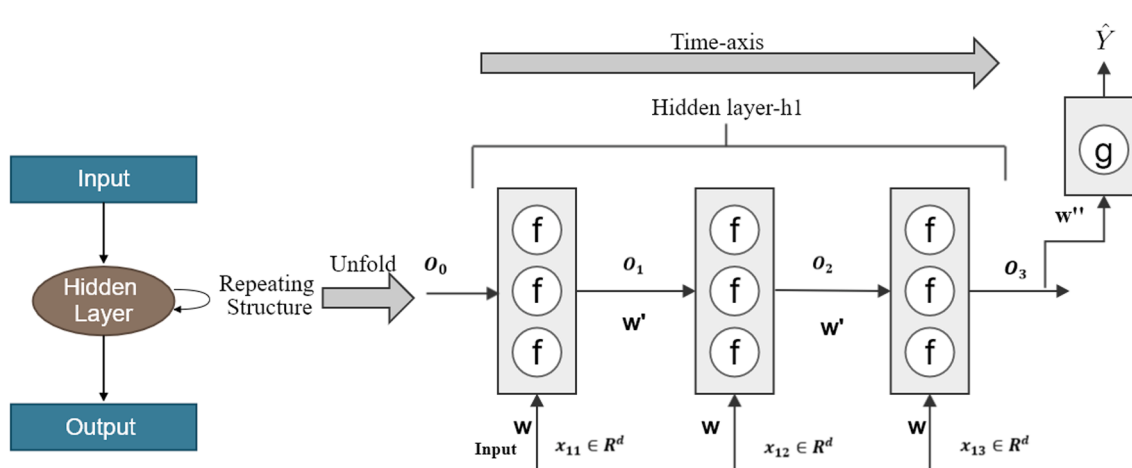


Fig. 20. Structure of a Recurrent Neural Network (RNN) unrolled.

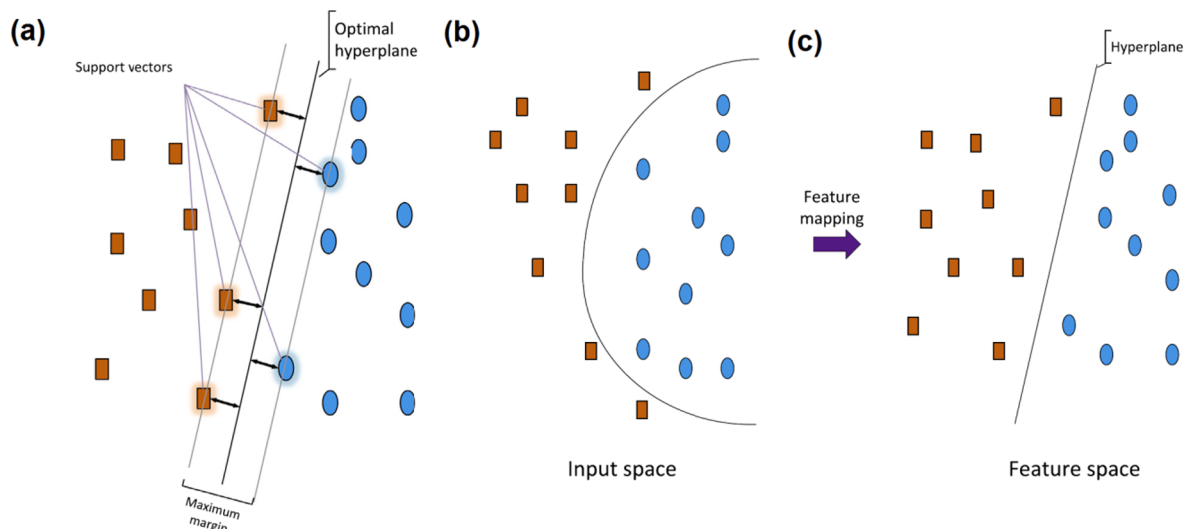


Fig. 21. (a) Structure of a Support vector machine (SVM) and (b, c) classification by a SVM [154] {Permissions of ©Elsevier}.

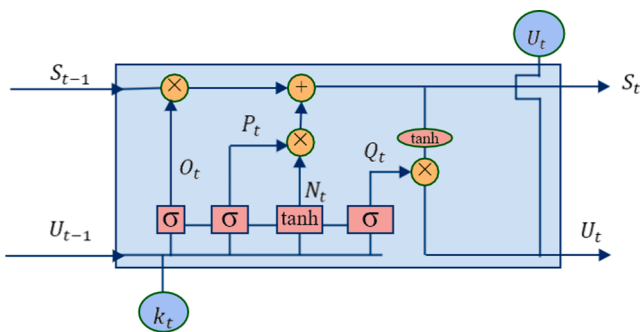


Fig. 22. Structure of a LSTM model.

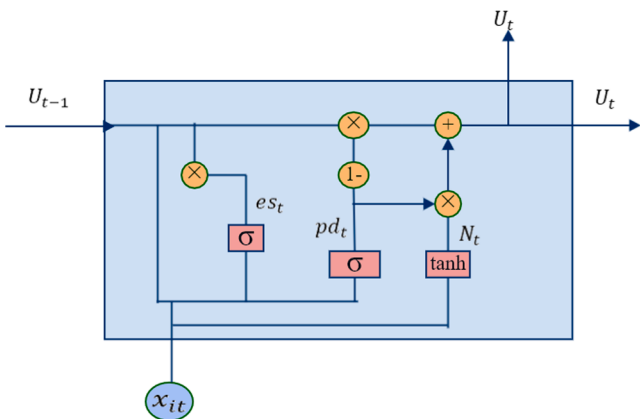


Fig. 23. Structure of the Gated Recurrent Unit (GRU).

4.11.7. Generative Adversarial networks (GAN)

GANs are category of deep learning models, which are based on generative modelling. The modelling approach is to understand the input data and generate the same patterns in unsupervised manner [160]. Now, GANs are supervised approach which increases the efficiency of the training task. Fig. 25(a) shows architecture of MatGAN for inorganic materials which consists of a generator that used to map the random vectors into the generated samples and a discriminator [161]. The generator generates very close training examples to the input data in order to fool the discriminator. The discriminator has to identify the

examples as real or fake. It is useful when the overall dataset is small. It is used in constructing 3D models, age photographs, improving the quality of images. The discriminator tries to differentiate real materials and generated ones. The encoder (shown in Fig. 25b) consists of convolutional and deconvolutional layers. The encoder solves the problem of identifying the materials composition in limited samples [161].

4.11.8. Decision tree

Random forest [142], is a popular implementation of decision tree which consists of many smaller trees which operates as an ensemble. Every tree that is formed portrays a decision (prediction) and decision having the highest votes becomes the model prediction. The power of the decision tree lies in the ensemble, a number of models working together to outperform a single prediction model. The height of the tree (i.e., nodes) depends on the data set's size. The various specifications can be optimized in order for both underfitting and overfitting to be avoided by reducing the validation set's prediction error (see Fig. 13).

4.11.9. Boosting method

Boosting is a category of ensemble learning, AdaBoost [162] and gradient boosting [163,164] is an example of boosting method. Both of these methods build a strong prediction model by aggregating weak learners. In this scenario, the performance mean of all weak models is provided for the expected output. Any poor learner would be sequentially included and trained by those inputs on which the learners are not able to perform well. The weight factor associated with each weak classifiers/learner is based on an actual forecast error of the assembled model following the addition of this weak classifiers [143].

4.12. Unsupervised machine learning

Unsupervised ML is employed to find different aspects of the input that can be defined objectively. It is a clustering technique that can be used to recognise distinctive data sets that appear more alike than others [147]. Typical unsupervised deep learning (DL) results in class-based data clusters where each cluster has homogenous samples [165]. The clusters found based on the inter-variable analysis are the right clusters. Clustering works well when working with two-dimensional input vectors Fig. 26. Three clusters are observed using the 2-dimensional data using K-means algorithm. Depending on the information's spatial scattering, these observations indicate three distinct concentrations (Fig. 26e) [166].

K-mean algorithm is one of the most often employed clustering algorithms [108,167–169]. The fundamental concept is to position K

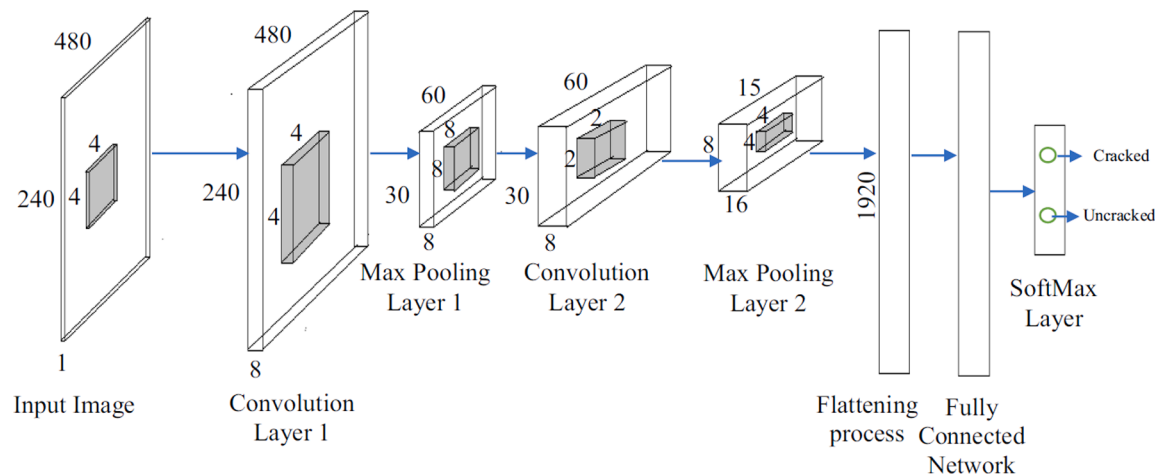


Fig. 24. Application of CNN model [159] {Permissions under ©Creative Commons CC-BY-NC-ND license}.

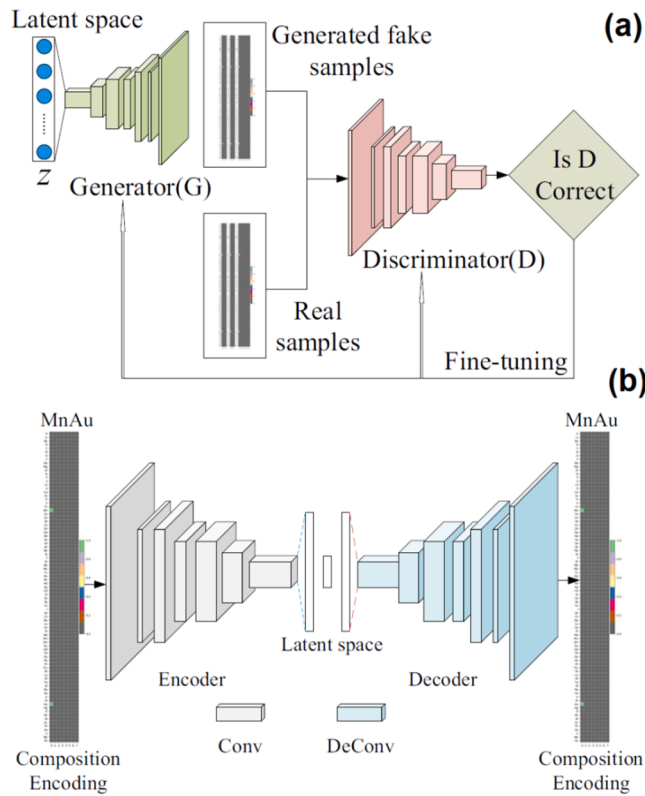


Fig. 25. Architecture of (a) MatGAN used for the inorganic materials and (b) GAN auto-encoder [161] {Permissions under ©Creative Commons Attribution 4.0 International license}.

clusters in the centre of the input area randomly. All data points on the first iteration are labelled with a Cluster ID centred on the centroid cluster in which the similarity is very high. The location of each centroid of a cluster is then upgraded depending on the mean of location of the labelled points that are a part of the cluster. It is then repeated until the centroid locations converge [108,170,171]. Please note the number of clusters K is determined in the K-mean algorithm and is a necessary input to the model. However, many approaches to calculate the best number of K-parameters [108] have been established, for example, Elbow [108] — the principle is that an optimum K-value can be selected for which any inclusion of centroids does not decrease cost-related work substantially e.g., the distances (squared sum) and its related centroid

[172,173]. A popular problem with it occurs during optimization it stays in local minima instead of global minima [174]. This constraint is partly solved by performing the multiple times, taking into consideration several random initial locations of the cluster centroids [174,175].

Density based spatial clustering of applications with noise (DBSCAN) is another type of clustering technique developed by Ester et al. [177] which performs the clustering on the basis of density. It is an unsupervised algorithm. The clustering of K-means may combine loosely related observations. Any sample would gradually become part of a certain cluster although the sample is far spread around the vector space. As clusters rely on the cluster elements' mean meaning, each data point plays a role in the cluster formation. The clustering result can be affected by minor changes in databases. This issue in DBSCAN is significantly reduced. Typically, this is not a major problem if we do not find any strange form results. An example of unsupervised ML applied for the identification and characterization of microstructures of 3D samples from MD simulations and experimental data is given in Fig. 27 [176].

5. Overview of ML techniques used for the development of new glasses

Glass fabrication techniques are especially delicate in industrial growth, manufacturing, buildings, and post-processing of glass. Though glass is a non-crystalline and fragile material and may cause catastrophic accidents during fabrication, processing, and assembling [178,179]. Moreover, in order to improve the material's brittleness, high-precision devices are used in glass and metalworking for their operations. The series of operations are washing, cutting, tempering (chemical or thermal), and lamination [178,179]. Right now, current approaches either struggle or are not appropriate for AI integration. The following explanations highlight how the ML may be used to produce glass goods at a higher pace with systematic approach than the conventional glass fabrication method. Table 3 represents the Machine learning based Molecular dynamics (MD) simulation techniques applied to the glasses. The detailed approaches of product development, processing, and inspecting are discussed follows.

5.1. Conventional models

In this section, conventional composition-property regression models are discussed. Researchers working on glass science and technology on composition development have so far used machine learning exclusively for property regression models. Pioneering activities have targeted the implementation of the artificial neural network [63,189,190,206]. Fig. 28(a) shows a typical ANN model with a hidden layer including 3 hidden nodes which used to predict the Solubility of

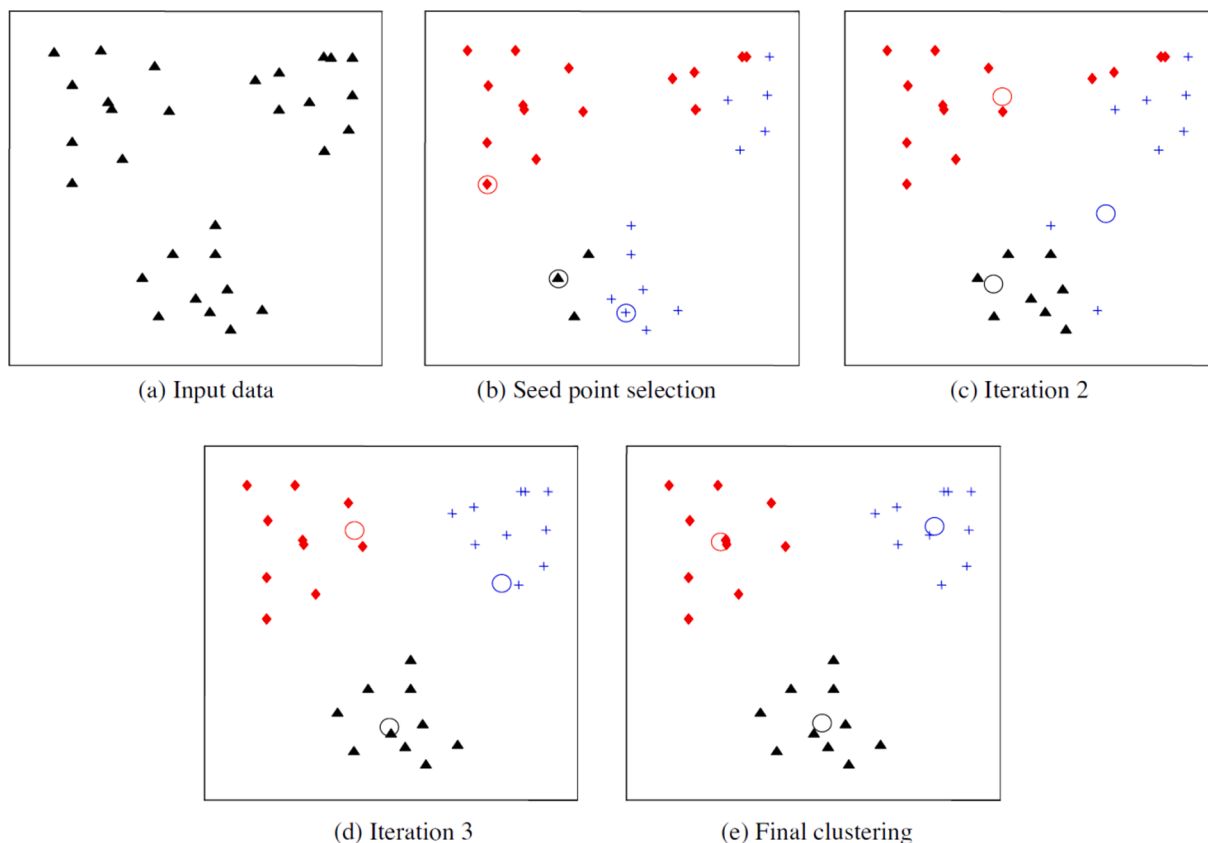


Fig. 26. K-means algorithm: (a) 2D input data with 3 clusters, (b) 3 seed points selected as the centres of cluster as an initial assignment, (c, d) updating of cluster labels and centres during intermediate iterations, and (e) optimal clustering at the end of convergence [169] {Permissions of ©Elsevier}.

P_2O_5 – CaO – MgO – Na_2O – TiO_2 . On the basis of literature, the first application of ML technique in glass was in the sense of solubility was performed by Brauer et al. [206] to predict the composition of P_2O_5 – CaO – Na_2O – TiO_2 glass. Fig. 28(b, c) distinguishes the predicted and experimentally measured data of glass composition. In all, the predictions showed close agreement with the experiments and the correlation coefficient R^2 was found as 0.999 [207]. Artificial neural networks have also been implemented to develop the different kinds of glasses with different properties and compositions [63,189,190].

Alcobaça et al. [95] used a dataset of 51,000 oxide glass compositions to predict the glass transition temperature. They used k -fold cross-validation to test and train the regression model. They mentioned that the ML model with tuned hyper-parameters showed better results as compared to default hyper-parameters tuning, as seen in Fig. 29. Fig. 28(c) illustrates the experimental and ANN predicted data of Young's modulus of several silicate glasses [63]. Artificial neural network showed excellent results for determining the Young's modulus ($R^2 = 0.991$) of silicate glasses as reported by Mauro et al. [63]. Artificial neural network has recently shown excellent results for determining the glass transition temperature i.e. T_g ($R^2 = 0.998$) as a function of glass composition (investigated by Casser et al. [190]), as shown in Fig. 28(d, e). The prediction of T_g is not consistently measured so it illustrates the dynamic details that the use of artificial neural networks is much feasible for complex datasets [190]. This implicates the thrust potential of artificial neural networks to extract the structure of data and to filter of the noise present in data (55,000 glass compositions) both at the same time. Thus, the artificial neural networks (i.e., "machine learning") are the promising prediction tool to predict the glass properties provided only by the study of existing datasets without any physical knowledge, as observed from Fig. 28.

5.2. Data-driven approach for development

At present time, there is a need for more flexible, more practical, and lower-cost, data-driven machine learning models in the field of glass design research, which is leading researchers to move beyond trial-and-error techniques in the design [208]. In this case, many innovative data-driven approaches are suitable because they utilises different models statistical as well as mathematical models and machine learning algorithms by using input database for training, testing, and validation. Another advantage of these approaches is to produce or procure cost-effective reference products at low cost. It is at least feasible to use first principle approaches to get an electronic band configuration, formation energy, and other thermodynamic parameters, but such measurements are prohibitively costly and will be almost too time-consuming. First principle approaches involves ab initio calculations, density functional theory, molecular dynamics, or lattice models etc. [75,76]. The optimization of new glasses can be achieved by an ML that can perform multi-objective optimization tasks with several constraints [209].

In recent years, computational technologies, databases, and data-mining algorithms have enabled researchers to discover new structural materials through AI, thus spending less time and money as compared to previous cases. Recently, Tandia et al. [208] reported a data-driven approach for a type of modern glass that was established based on statistical analysis. They mentioned the two most significant glass design characteristics are the liquidus temperature and the viscosity. The lack of reliable and quantitative models for glass liquidus temperature and viscosity continues to be a problem at present time. Tandia et al. [208] applied the Neural network (NN) of ML technique was used for the prediction of liquidus temperature and the viscosity. In the Fig. 30, we will see the imaginative and the predictive capacities of the NN are demonstrated [210]. The neural network-MYEGA (NN-MY) equation

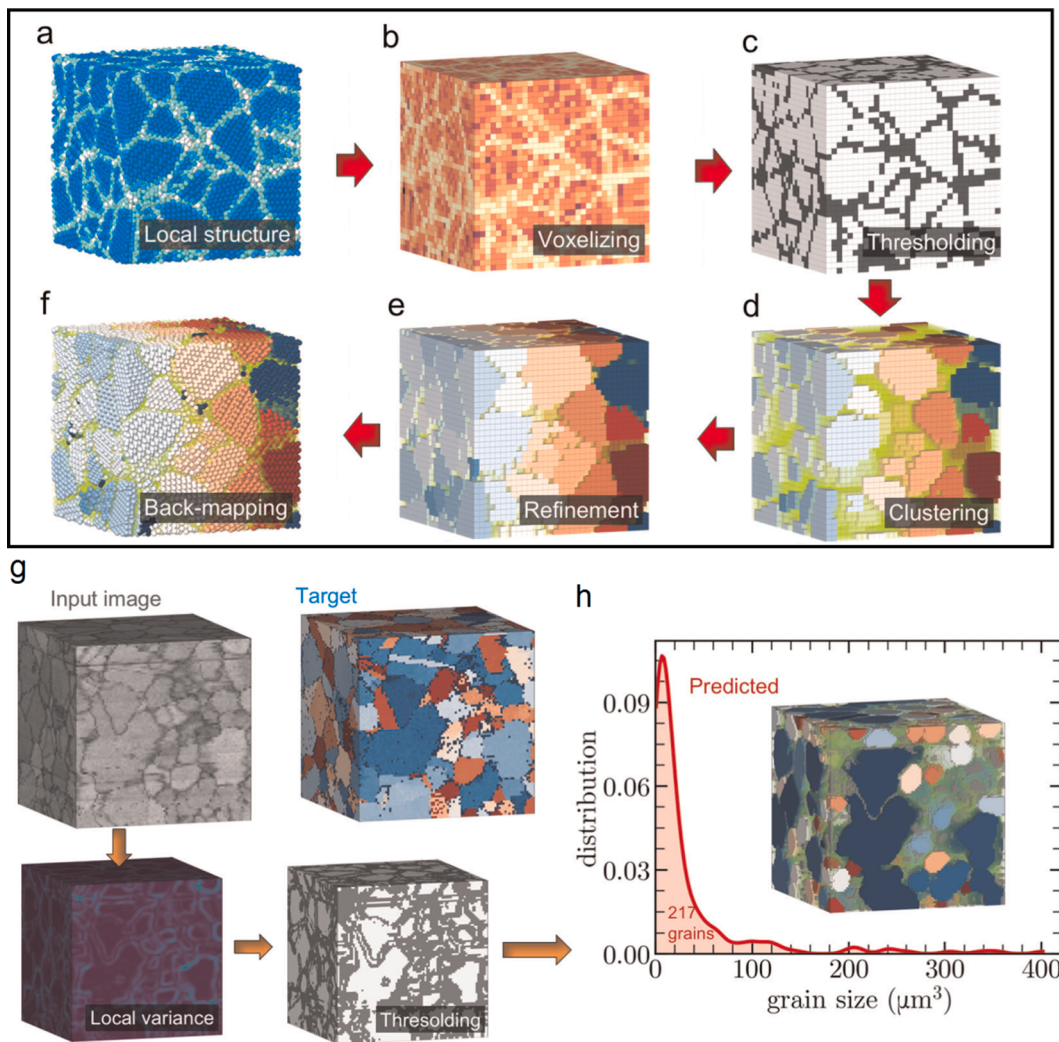


Fig. 27. (a-f) Steps involved in simulation of 3D samples and (b) Application of DBSCAN for the identification and characterization of microstructures of 3D samples from MD simulations and experimental data [176] {Permissions under ©Creative Commons Attribution 4.0 International license}.

produced a stronger predictor with low validation error than the other methods used models, and thus enabled for new glasses compositions at a lower cost in time and with reduced error [210]. More information on this problem can be found in study by Tandia et al. [208] and the other application of AI to glass production are reported by researchers [4,63].

Another typical example of data-driven CNN model is given in Fig. 31. A total of 32 filters convolved the microstructure, rectifier function activated the outputs, average assembled into 8 values and 256 features were generated. The learned model produced similar structure as desired for 3D model.

5.3. Physics informed models

Although data driven artificial intelligence approaches are ideally suited for precise forecasts on the other hand, these approaches (including blind machine learning (BML) and ANN) need a vast volume of existing data that is unavailable in some situations. Due to their complex structure, the artificial neural networks make it difficult to provide any new physical knowledge, although have excellent in terms of interpretation. Instead of “machine learning based on physics principles”, Liu et al. [188] proposed the theory of “physics-informed models”. It utilises a simple, analytical model (such as a polynomial function) that provides a suitable understanding of the model’s response, helps improve interpretability, and maintains linearity by

simplifying chemical properties, and also relies on relevant reduced-dimensional descriptors that encompass the atomic structure of glass [188,211]. This method was recently applied on a small dataset (~200 data points) to estimate the dissolution rate of silicate glasses i.e. $\text{Na}_2\text{O}_2\text{O}_3\text{-Al}_2\text{O}_3\text{-SiO}_2$ on the basis of their known compositions and pH value [188]. In Fig. 32, the variation between polynomial and physics-informed machine learning is shown. It was found that the optimal model for BML consists of a 5°polynomial function [188]. However, the training and test relative-root-mean-square-error values are low i.e. the training RRMMSE of 98% and the testing RRMMSE of 73% which means that this model results in weak predictions [211], as shown in Fig. 32(a). This means that BML (like polynomial regression model is used in this situation) requires sophisticated machine learning algorithms (e.g., artificial intelligence) to predict the dissolution rate for the variation of composition and pH [189,212]. Updated physics-informed model shown in Fig. 32(b) showed a much improved performance, the RRMSE values for the training and test sets were found as 2.32% and 3.77%, respectively [188]. This was largely guided by the physical and chemical knowledge of the silicate dissolution mechanism. The physical and chemical knowledge develops a linear relationship between the inputs (namely glass composition & pH value) and output namely dissolution rate. The model’s sophistication was significantly reduced in terms of polynomial degree i.e. 1 which was 5 during the BML. Furthermore, the amount of reduced-dimensionality descriptors that represents the

Table 3

Machine learning based Molecular dynamics (MD) simulation techniques applied to the glasses.

S. No	Classical approach + ML Technique	Materials	Results	Reference
Unsupervised Machine Learning	3D Random Material	• Grain Boundary Segmentation • Grain size distribution • Voids	[176]	
3D Convolutional Neural Network (CNN)	Data Driven approach 3D Model	59,000 microstructures	[180]	
Generative Adversarial Network (GAN)	Inorganic Materials	Chemical Composition Design	[161]	
Data driven predictive model (M5 Model Tree) + 3D MVE (Microsoft Volume Element)	High contract composite	Elastic strain	[181]	
Ensemble based regression				
Temporal Independent CNN	Brittle Materials	Temporal fracture path spall region	[182]	
Bi- Long Short-Term Memory Networks (Bi-LSTM)				
DEM REV RNN RVE FEM model (hybrid models containing RNN-LSS-ANN)	Multimobility porus media	Hydro-mechanical responses	[183]	
Gaussian process regression (GPR) technique	Oxide glasses (Ca AL silicate glass)	Young's modules	[137]	
K-nearest neighbour, Random forest, LASSO linear regression, SVM and ANN	2,485,824 oxides	Young's modules Shear modules Poison's ratio	[142]	
FSTS-SVM	Ge _x Se _{1-x} glass transition	Tg onset temperature x = 0.33	[184,185]	
Experimental method microscopy enabled Cracks of on cutting edges	Glass	Edges after polishing and grinding	[186]	
Experiment	Glasses	Semantic segmentation DL-UNET	[186]	
Topology informed Machine learning	Silicate glasses	Cracks, post fracture service life, crack pattern	[187]	
ML ANN linear regression	Silicate glasses	Dissolution kinetics	[188]	
Neural network	55,000 inorganic glass	R ² training = 0.850 R ² testing = 0.757 T _g	[189]	[190]
HT-MD ML using LAMMP package Experiments	Silicate glasses	Stiffness	[191]	
Computer code generation (Numerical Methods)	Aluminium borate glasses	Chemical durability of glass field strength [78]	[78,192,193]	
	Random material glasses	• Elastic constant • Young's modules • Poison's ratio	[194–196]	
	Low silica Ca Alumina			

Table 3 (continued)

S. No	Classical approach + ML Technique	Materials	Results	Reference
		silicate glass [194]		
	Experimental	Borosilicate alumina silicate glass	Mechanical properties under the effect of composition	[197]
	ML-SVM	Disordered solids	Structural flow defects	[198]
	Experimental	Glassy thin films	Structure and dynamics	[199]
	ab intio MD + ML forcefield (GPR, Bayesian)	Silicate glasses	Structure	[200]
	ML	Silicon	Bonds or pairs Bond angle	[201]
	ML	Carbon	Interatomic potential Interatomic potential	[202]
	ML, ANN, GPR and RF	Oxide glass	Tg	[95]
	Failure analytic method LEFM theory	Glass beans	Strength on out edge ground edge	[203]
	Experimental method	Glass	Analysis of glass fracture	[204]
	Experiment	Glass with polished	Edge strength and cutting-edge finishing	[205]
	Edge cutting spatial clustering technique	Glass	Cutting edge	[173]

topological constraints per atom (Σn_c) was added to quantify how the glass network's configuration governs its dissolution rate [77,78,192,193,212–214]. This significantly enhances the model's extrapolation capability to the initial set of training [188]. From the findings, it, this work indicates that embedding physical information within machine learning provides a promising route to increase the accessibility of models, which have been previously been in conflict with each other characteristics: consistency and interpretability [116]. However, in case of BML model, the consistency and interpretability doesn't often together [189,215]. From a practitioner's view, more reliable yet non-interpretable models (e.g., a random forest or artificial neural networks) are easy to use, while interpretable models (e.g., polynomial regression) are tougher to implement but offer greater precision [189,215], illustrated in Fig. 32. In general, models that are less likely to be subject to overfitting are preferable; for limited datasets, it is essential to choose more computationally-efficient models.

5.4. Models informed by high-throughput simulations

The accuracy of machine learning models irrespective of the algorithm depends on the abundance of reliable and consistent data to widen the compositional domain [188]. Extensive datasets of experimental data are rarely usable due to the availability of high-throughput molecular dynamic (HT-MD) simulations. The HT-MD can be used as a useful training set for machine learning algorithms due to their facilitation of consistent, and accurate datasets of glass properties in [4,191]. Traditionally, the classical MD based topological models were used to predict the Young's modulus of glasses. One of the models used for the prediction of Young's modulus (E in GPa) of poly-component glasses is Makishima-Mackenzie model [216] which was derived using electrostatic attraction energy of ionic crystals, written as:

$$E = 2V_t \sum_i G_i X_i \quad (25)$$

In the above equation, the V_t , G_i , and X_i represents the atomic

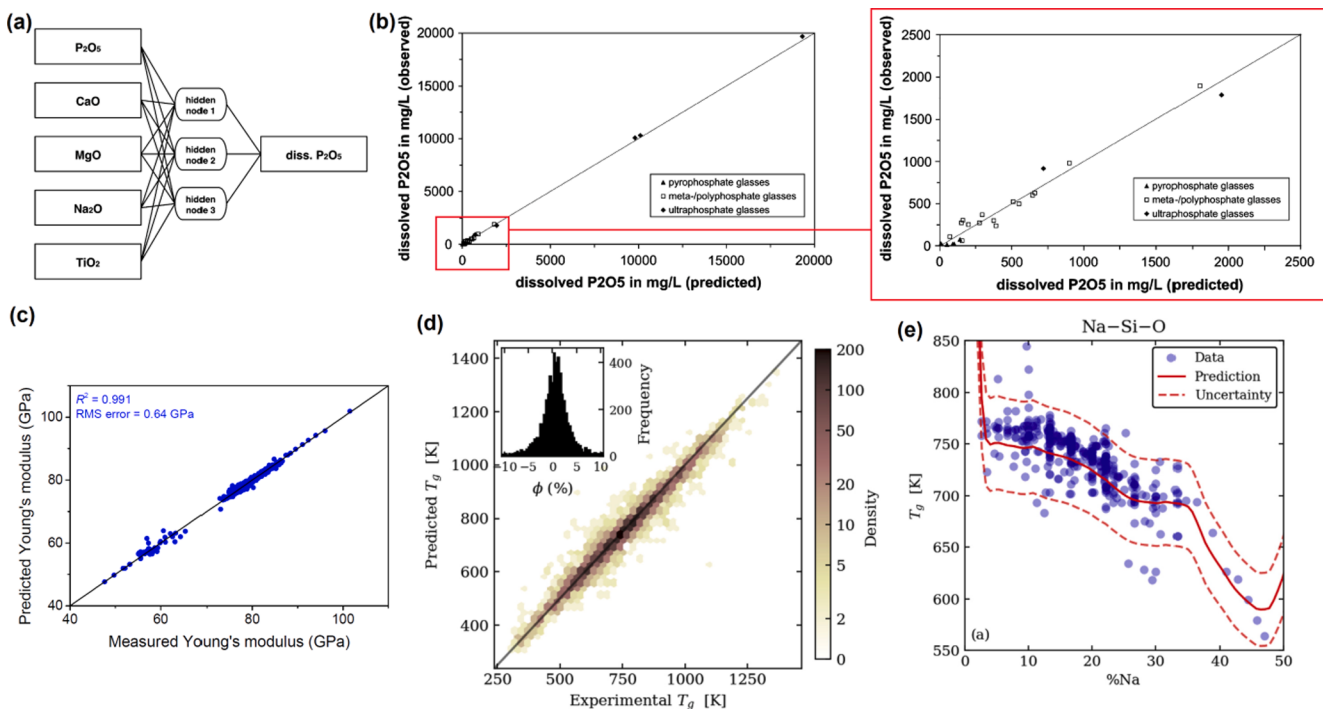


Fig. 28. (a) A typical ANN model with a hidden layer including 3 hidden nodes which used to predict the Solubility of P₂O₅–CaO–MgO–Na₂O–TiO₂ [206], Comparison between predicted and experimental properties: (b) glass solubility [206], (c) Young's modulus [63], (d) glass transition temperature of several glasses [190], and (e) glass transition temperature of sodium silicate glasses [190] {Permissions of ©American Chemical Society, ©Elsevier}.

packing fraction, dissociation energy per unit volume of the oxide component (i), and oxide mole fractions, respectively. Similarly, they have given a model for the prediction Young's modulus of multi-component glasses, written as:

$$E = 83.6V_i \sum_i G_i X_i \quad (26)$$

Makishima and Mackenzie [216] compared the measured Young's modulus with their MM model and found a good agreement with the measured results, as shown in Fig. 33.

Yang et al. [191] recently employed this to predict the Young's modulus for silicate glass with respect to composition. Young's modulus of CaO–Al₂O₃–SiO₂ glass ternary system as a function of composition was computed by HT-MD simulations is illustrated in Fig. 34(b). The composition domain can be efficiently explored with HT-MD simulations in a systematic and homogenous way. Accuracy and low noise-to-signal ratio are the keys to data-driven simulations. In Fig. 34(b), the ANN predicted results can be seen as depicted on the basis of data illustrated in Fig. 34(c). A comparison of MM model [216] predicted and MD simulations computed Young's modulus is shown in Fig. 34(d) which shows a R^2 of 0.556. However, the HT-MD simulations predicted Young's modulus showed a good agreement with MM model [216] as showed R^2 of 0.979, as shown in Fig. 34(e).

Yang et al. [191] also compared the ML models like Polynomial regression, ANN, LASSO, and Random forest (RF). A non-linear evolution of the Young's modulus as a feature of composition has been successfully modelled using an artificial neural network (ANN). However, it was noticed that the ANN successfully reduced the extraneous noise in the simulation results. ANN model showed the best results as compared to the other models. ANN showed a value of R^2 of 0.975 for the prediction of Young's modulus followed by PR (R^2 of 0.970), Lasso (R^2 of 0.966), and RF (R^2 of 0.965), as shown in Fig. 35(a-d).

From the Fig. 36, it's pointed out that the expected values fit very well with data. The measured stiffness value does not show much change even though the cooling rate differs from those observed in MD simulation—since it is mainly regulated by the interatomic potential's

curvature [195,196]. Predicted results shows the benefits by the machine learning with use of HT-MD simulations. Nonetheless, despite the simplicity of CaO–Al₂O₃–SiO₂ glasses and their technical importance, the available stiffness data is small for experimentation. Moreover, that much of the usable compositional data clustered in to unique small regions of the entire for example pure SiO₂, per-alkaline aluminosilicates, and calcium aluminate glasses. Additionally, the accessible results come with notable clustering is a serious issue. Furthermore, the Young's modulus of such glasses varies by 20 GPa as mentioned in studies [194,217]. Thus, machine learning methods cannot distinguish "true" trend from "noise" because of the large degree of background noise and data clustering in such a manner. As compared to performing comprehensive investigations, MD simulations produce quicker and cheaper performance. In spite of the fact that running MD simulations, the computations do not fully account for long-term ageing or dissolution kinetics of glasses. Thus, mathematical simulation (ranging from analytical to physics-based) often utilises many methods to bridge temporal time scales [4]. Though they also complement each other, data-driven learning and physics based simulations provide generating possibilities of developing novel glasses when used together.

Machine learning has the capacity to look for non-intuitive structural patterns in multi-dimensional details, and thus provides a potential route for discovering the unexpected structural rules for glass properties [79]. Recently, Cubuk et al. [217] have introduced a classification system of machine learning to detect the "high level structural fingerprints" which confines the dynamics of atoms reorganizations (also called softness) [79,80,198,199,227]. On a molecular level, atomic softness is an inherently non-intuitive property of structure, which is derived from the surrounding atmosphere of each atom [79]. It was determined through the classification of the atoms into "soft" (capable of moving) and "rigid" (fixed) and to put each atom's sign, mark, or rank. A variety of formal descriptors were then used to further develop the systematic structure of atoms. Finally, an SVM model of classification was employed to find the hyperplane in the input space that enables to differentiate soft atoms from hard ones. For any input, the orthogonal

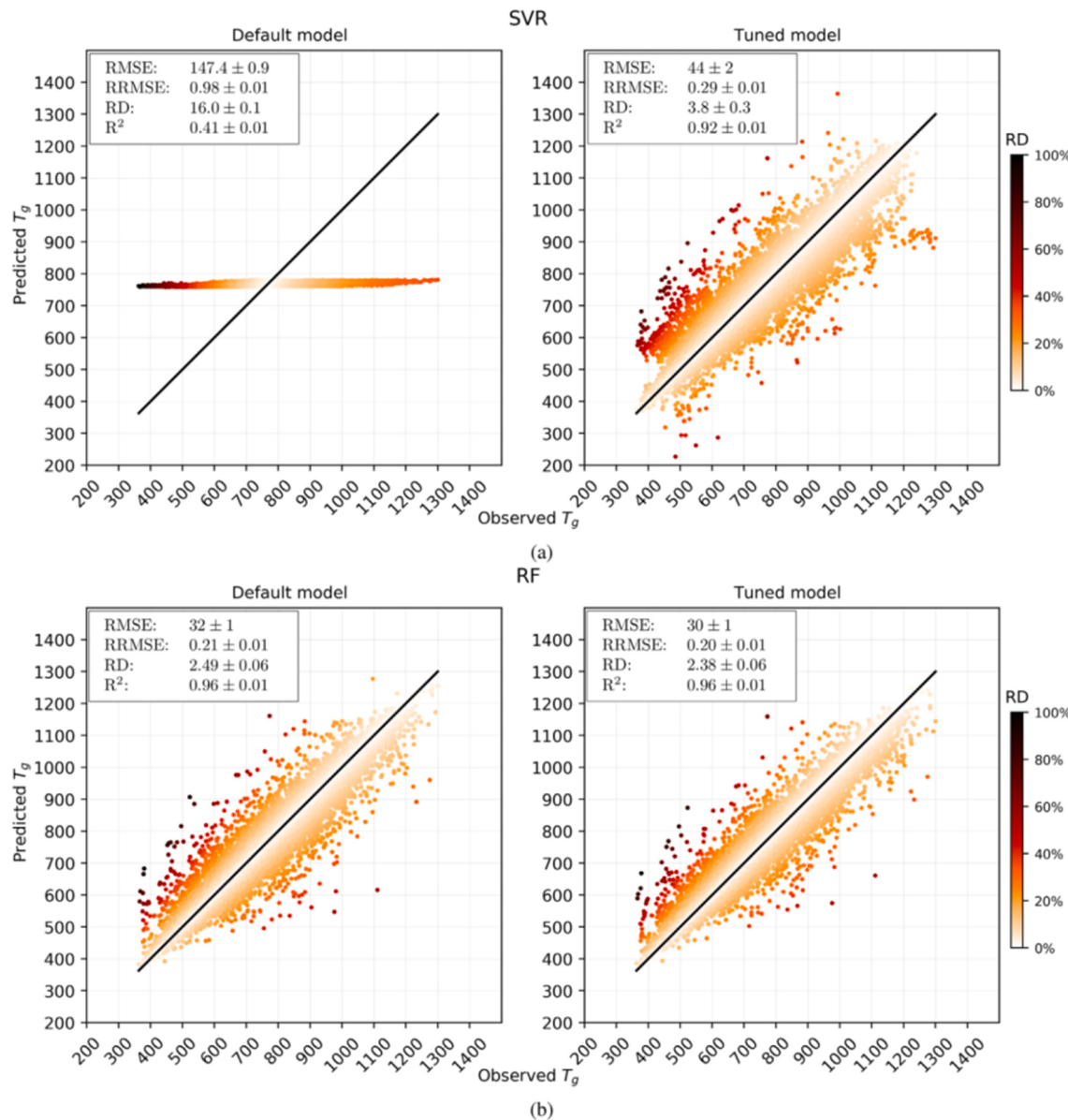


Fig. 29. Default vs. tuned hyperparameters for (a) Support Vector Regression and (b) Random Forest (RF) [95] {Permissions of ©Elsevier}.

spacing between inputs space and the hyperplane was established to define the atomic softness [198]. The rearrangement probability (P_R) of atoms likelihood is observed to be a logarithm feature of their softness (S) overcooled liquid system [227,228], as seen in Fig. 37. While the method has so far been used only for Lennard Jones glasses i.e. ‘toy’ model. This study helps to cover the way for machine learning structural fingerprints that refer to the atomic structure of glasses to glass properties like dynamics, plasticity, etc.

5.5. ML forcefields for glass modelling

The MD (or Monte Carlo) simulations are essential to identify the elemental composition of glasses, which helps scientists to understand how composition is related to the properties. In glass modelling, however, the interatomic forcefield has a high sensitivity to variables that restricts the inherent reproducibility [149]. Machine learning may be used to accurately create new interatomic fields for glass design [200]. So far, these machine learning techniques have only been effective in unanalytical interatomic force fields that show low interpretability and limited to simple monoatomic or diatomic systems [201,202,229].

Empirical forcefields built on analytical methods are able to render an accurate explanation of atoms arrangements in silicate glasses [26,71,81–84,200]. Empirical force-field parameterization, though, appears to be a complex process that requires intuition. The forcefield parameterization is typically relies on cost formulation that depends on a forcefield parameters [26,71,83]. Previously, Carré et al. [83] proposed a new cost function to optimize the design by measuring the differences between liquid’s simulations by initio molecular dynamics and that predicted by the forcefield. Finding the optimum force-field parameters minimises the cost function. Conventionally, the classical minimization algorithms were used for example steepest gradient descent methods [230]. In steepest gradient descent [230], one following the path of steepest gradient descent in the random initial parameter space (e.g., the direction of steepest gradient) until it becomes zero. However, such methods produce functions that are generally local rather than global minima, and, but as such the result is heavily influenced by these initial parameters, it is difficult to parameterize of forcefield due to bias output [83,230].

A flow chart of the ML based parametrization strategy with Gaussian process regression was proposed by Liu et al. [185] is illustrated in

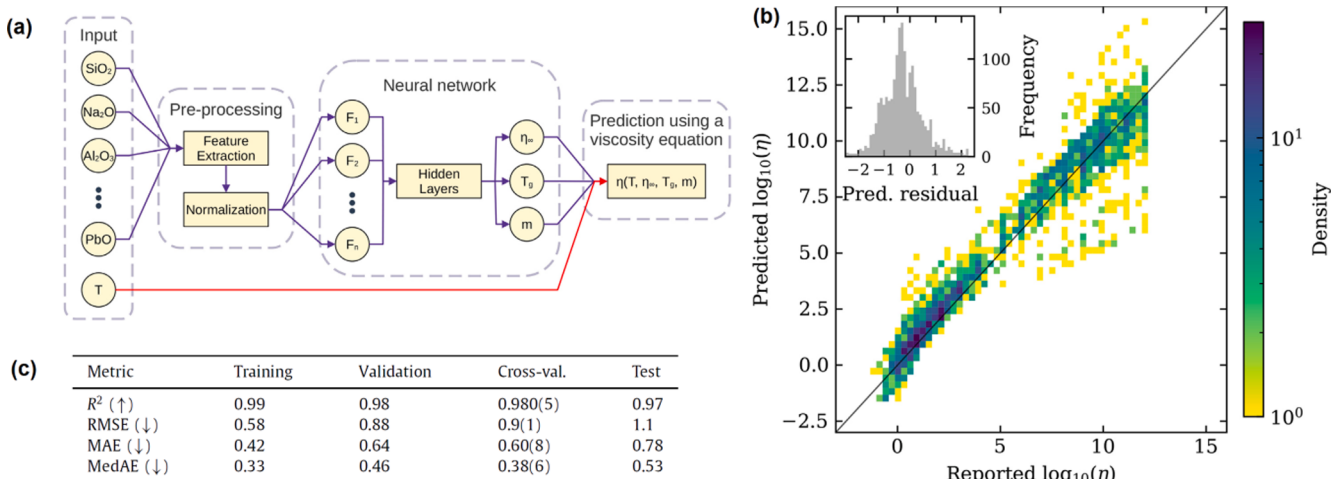


Fig. 30. (a) Architecture of ML pipeline, (b) Predicted versus reported values of $\log_{10}(\eta)$ for the test dataset, (c) errors during training–testing-validation [210] {Permissions of ©Elsevier}.

Fig. 38(a). **Fig. 38(b)** indicates a cost function (R_χ) for glassy silica which was varied with forcefield parameter to be reduced over time. Any other forcefields stay unchanged. A cost function (R_χ) for glassy silica is given by [185]:

$$R_\chi = \sqrt{\frac{\chi_{\text{SiO}}^2 + \chi_{\text{OO}}^2 + \chi_{\text{SiSi}}^2}{3}} \quad (27)$$

In the above equation, the $\chi_{\alpha\beta}^2$ represents the level of confidence between classical MD and AIMD pair distribution functions (PDFs), written as:

$$\chi_{\alpha\beta}^2 = \frac{\sum_r \left[g_{\alpha\beta}^{\text{AIMD}}(r) - g_{\alpha\beta}^{\text{MD}}(r) \right]^2}{\sum_r \left[g_{\alpha\beta}^{\text{AIMD}}(r) \right]^2} \quad (28)$$

Where, the terms $g_{\alpha\beta}^{\text{AIMD}}(r)$ and $g_{\alpha\beta}^{\text{MD}}(r)$ represent the pair distribution functions (PDFs) of atoms. In **Fig. 38(b, c)**, a total of nine forcefield parameters were fixed however, the Si atoms' partial charge (q_{Si}) was optimized.

Forcefield data for the value of the cost function (R_χ) is evaluated via the GPR method [200,231,232] on the basis of known inputs. The '95% confidence interval' uncertainty of prediction was observed. Bayesian optimization (BO) was employed while considering the GPR projections and the uncertainty which defines an optimum collection of forcefield parameters. Determining a feasible set that maximise the probability of yields an optimum collection of force field parameters that has the lowest expected cost function R_χ . The so-called anticipated change (see **Fig. 38c**) proposes the strongest compromise between 'exploitation' and 'exploration' [231]. The actual cost function R_χ is then calculated by MD simulations and then implemented in the training set that improves the GPR model. This is the optimum set of parameters. New optimum parameters for forcefields are then iteratively forecast until the cost function has reached a sufficient minimum, that is, when R_χ does not further drops. **Fig. 39(a)** illustrates this iterative optimization approach that represents a path explored by the Bayesian optimization method before a minimum of global value in the cost function (R_χ) is found. This method is investigated by the Bayesian optimization method. The parameterization approach is seen to produce a unique degree of agreement with ab initio simulations [200] and develop a forcefield for the glassy silicate. In general, machine learning is a promising way of speeding up the integration of new forcefields into complex and multi-component glasses. **Fig. 39(b)** illustrates the final conjugate gradient optimization (CGO) of R_χ in terms of q_{Si} and A_{SiO} . A total of eight forcefield parameters were fixed and the partial charge of the Si-atoms q_{Si} and the parameter A_{SiO} were optimized. **Fig. 39(c)** represents the

$\pm 0.5\%$, $\pm 0.25\%$, and $\pm 0.25\%$ of relative uncertainty in the cost function of the forcefields ML-SiO, ML, and ML-ALL respectively. Partial bond angle distributions (PBADs) of O–Si–O and Si–O–Si in liquid silica were predicted by the different machine learning forcefields that were parameterized at $T = 3600$ K, as shown in **Fig. 39(d, e)**.

6. Overview of conventional and ML techniques used for testing of glass properties

A lot of glass properties involved in manufacturing and inspection. The main failures in glass instalment in different applications are failure of edges, unfinished edges, glass cracking, unfinished chamfering, and poor polishing. The researchers have focused more on development of glasses on the basis of superior mechanical properties. Glass can be designed on the basis of composition and various mechanical properties like edge strength, shear strength, tensile strength, Young's modulus, Elastic modulus, delamination, etc. [3]. In earlier sections, the development of new glasses was discussed on the basis of various properties. In this section, the different aspects of glass engineering and technology are presented.

6.1. Inspection and testing

Currently, the additive manufacturing technique is widely used to form new types of glasses and other materials. Additive manufacturing technique requires minimum or no human involvement to verify the materials' quality, testing, and repeatability of the operations. Visual inspections are normally carried out to evaluate various macroscopic properties of glass, for example, for the consistency of the edges i.e. uncertainty of thermal tempering the glass [233], edge quality of cut glasses [186], neatness of glass during operations, and checking of the adhesion between the layers [234]. Visual inspections that enable the operator to view output across the whole manufacturing chain through the use of process-specific quality steps. Non-negligible statistical ambiguity occurs by human during visual testing, for example own biasness during testing [235].

The application of AI in the field of production management of glass seems encouraging on the basis of promising quality inspection and systematisation of glass development processes using an AI approach. In fact, the machine learning and deep learning already have been promising for similar fields, such as picture or video recognition, computer vision, etc. [100,103]. Pummel test is carried out through in order to organize and automate the visual product inspection for laminated glasses. Pummel value measures the interlayer adhesion between

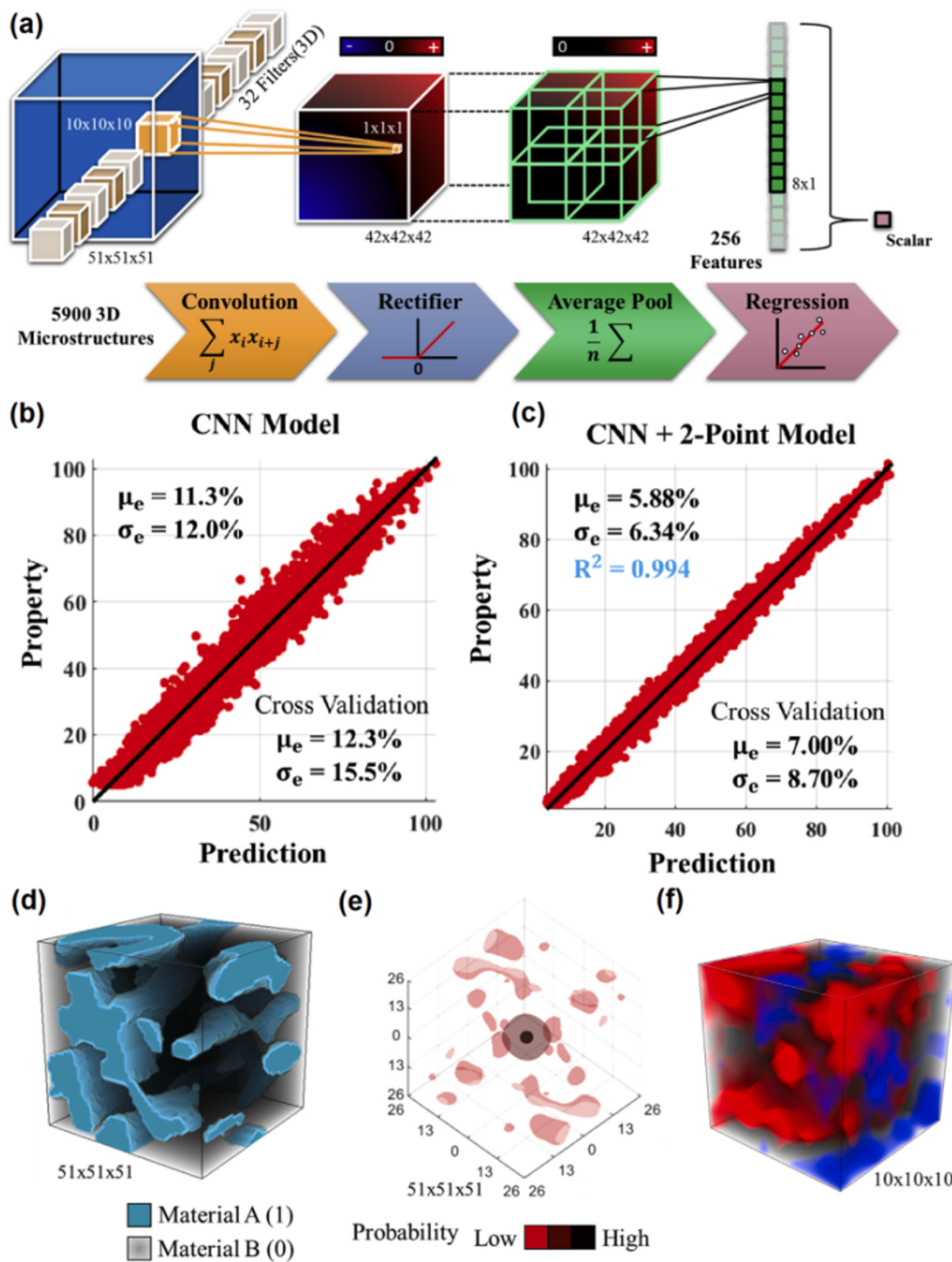


Fig. 31. (a) Architecture of Convolutional Neural Network (CNN) Data-Driven approach 3D Model (32 filters convolved the microstructure, rectifier function activated the outputs, average assembled into 8 values and 256 features were generated) (b, c) scatter plots and error metrics for: (b) CNN model and (c) CNN + 2-point unified statistical model, (d) a microstructure showing architectural features, (e) contrasting and their spatial statistics, (f) a selected subset of learned filters that distinguished the nearly architectural features [180] {Permissions under ©Creative Commons Attribution 4.0 International license}.

polymeric and the glass laminated sheets using an adhesive scale from 0 i.e. no adhesion to 10 [236]. For the Pummel examination, laminated glass includes two glass panes of float have a thickness of 24 mm (maximum). During the testing, the room temperature is kept 18 °C and glass laminate is exposed in this environment for 8 h. Then, the exposed laminate is put on an inclined metal block and beat with a hammer called pummel. After pummelling, the value of the Pummel is determined by a human inspector using a formula which calculates the area of

the polymer interlayer that is exposed. The details of pummel test are given in studies [178,234]. In this conventional test, so far the key problems of image-based computer vision research require vast quantities of image processing before features can be retrieved.

However, a proper output metric on the pummel images need to be chosen that doesn't differ greatly in the real-world conditions like thin cracks, surface roughness, shades, inadequate light in the room of pummel inspection etc., then the one can achieve only unclear results.

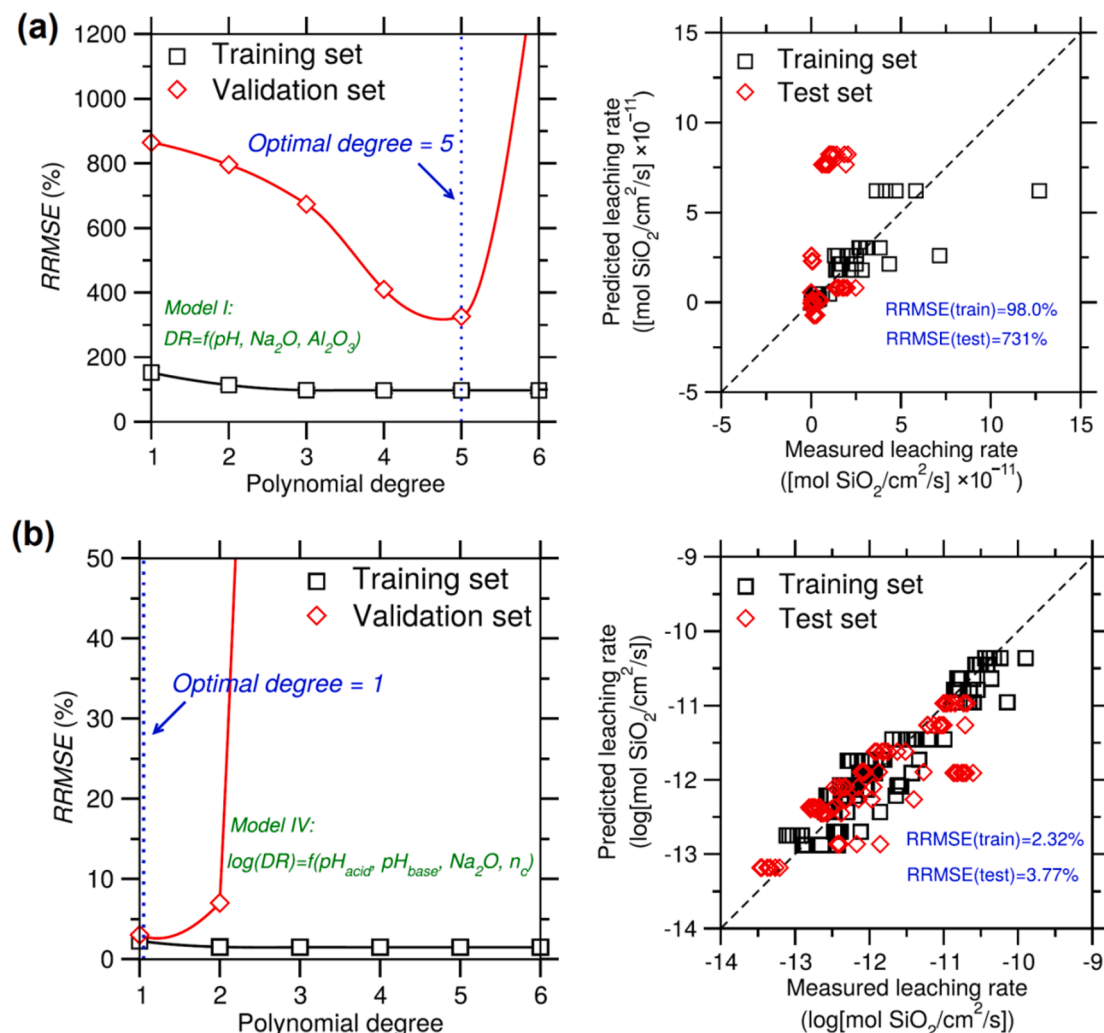


Fig. 32. Glass dissolution rates values: measured versus (a) Blind ML and (b) physics-informed ML predicted results. Polynomial regression models for the training and test sets [188] {Permissions under ©Creative Commons Attribution 4.0 International license}.

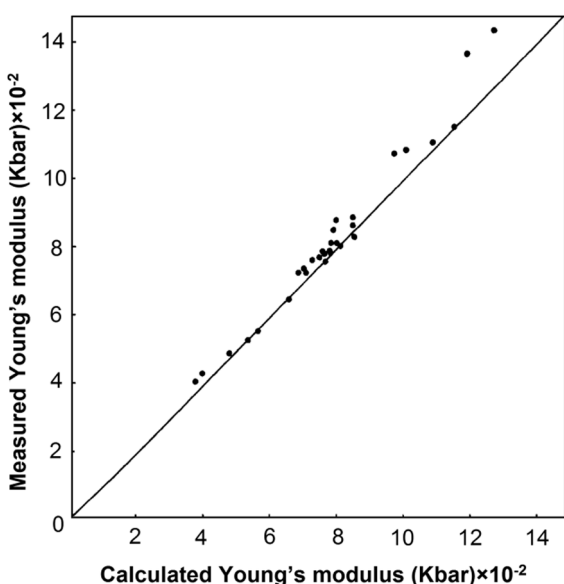


Fig. 33. Measured vs. MM model predicted Young's modulus [216] {Permissions of ©Elsevier}.

Moreover, due to the lack of large amounts of labelled training image data, it faces another challenge. An artificial intelligence based pummelled classification tool with deep convolution neural network is a data driven approach that can be used to resolve these issues. This tool can provides a more refined inspection by using interactive visualization through the completely automated pummel evaluation. Moreover, the human bias in terms of tuning before taking the pummel images can be rectified by using AI post processing. A typical proposed architecture of AI supported pummelled classification is illustrated in Fig. 40. Then the pummel pictures are pre-trained on the CNN [102,103]. The picture classifier can be trained on a previously quantified CNN to use for quantifying pre-defined probabilities that this analysis produces.

6.2. Young's modulus

By using the Mauro et al. [92] and Smedskjaer et al. [65] models, Yang et al. [64] proposed a new model for predicting the young's modulus. They used the statement of hardness, according to which, hardness is a linear function of the number of constraints (n_c) per atom:

$$E = \varepsilon_{BS}n_{BS} + \varepsilon_{BB}n_{BB} \quad (29)$$

Where, the subscripts BB and BS represent the bond-bending and bond-stretching respectively.

Wilkinson et al. [237] used a computation approach to evaluate the Young's modulus of $0.3\text{Na}_2\text{O}-0.7(\text{ySiO}_2\cdot(1-\text{y})\text{P}_2\text{O}_5)$ glass. They proposed

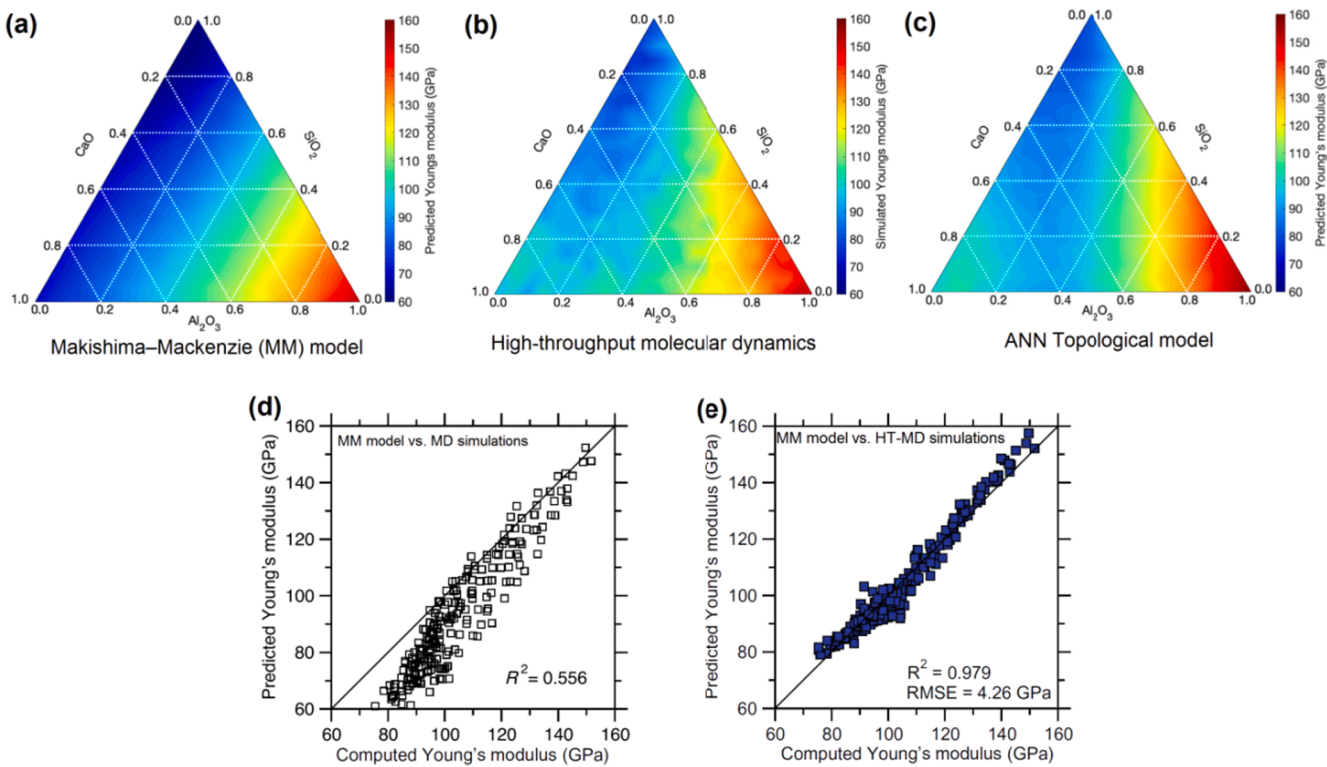


Fig. 34. Ternary diagrams of Young's modulus computed by (a) Makishima-Mackenzie model [191] (b) high-throughput molecular dynamics (HT-MD) simulations [64], (c) Topological model (MD) simulations [64], (d) MM model predicted vs. MD simulations [191], and (e) MM model predicted vs. HT-MD simulations [64] {Permissions under ©Creative Commons Attribution 4.0 International license and by ©Elsevier}.

a new model for the calculation of Young's modulus:

$$E = \frac{dE}{d\Delta F_c} [\Delta F_c(x) - \Delta F'_c] \quad (30)$$

They found that the model predicted root mean square error (RMSE) values for constraint density, free energy density and angular constraint density as 6.41, 3.13, and 7.74 GPa respectively, as seen in Fig. 41. They also predicted the temperature dependence of Young's modulus. The curve fitting was done for 14,000 points for the free parameters like vibrational frequency and the heating time. By using a least-squares method, the previously fitted data was fitted in equation (30). The cutting fitting depicted an R^2 of 0.94.

Shi et al. [238] modified the MM model [216] and developed a new model for the prediction of Young's modulus of glasses on the basis of the Rigid-Unit packing fraction (RUPF) and atomic packing fraction (APF), written as:

$$E = 2\eta_{RUPF} \frac{\sum_i G_i^{mole} X_i}{V_m} \quad (31)$$

$$E = 2\eta_{APF} \frac{\sum_i G_i^{mole} X_i}{V_m} \quad (32)$$

In the above equation, η_{RUPF} and η_{APF} represented the new Rigid-Unit packing fraction (RUPF) and atomic packing fractions (APF), respectively. Symbol G_i^{mole} represents the dissociation energy per mole for the oxide component i , X_i represents the oxide mole fraction, and V_m is the molar volume of glass. Young's model predicted by Shi et al. [238] models was compared with the measured Young's model for 155 glasses and shown the R^2 fitting of 0.998 as shown in Fig. 42.

6.3. Semantic segmentation of glass

Normally, in glass panel post processes, the annealed float and normal glass pane of are cut to size and then further refining takes place

before they are assembled. To form a fissure, a cutting wheel is first used to create a fissure on the surface of the glass. In the second stage, the cut is processed to bending stress, so as to cause it to open along the fissure. Many process parameters affect the cutting of glass, including the edge strength, which can be increased by adjusting the process variables of the cutting machine [239]. Yoshida [240] reported the phenomenon of cracking at the glass edge by using the Indentation fracture (IF) method. It was mentioned that two mechanisms namely indentation deformation and cracking plays in edge cracking of glass. Two types of cracks are mentioned in that study such as median crack and palmqvist crack. Asai et al. [241] mentioned that the tensile, compressive, and principal stresses develops in the glass due to indentation that causes glass failure.

This part focuses on machine-cut glass predictability using supervised machine learning, particularly for Extra Randomized Tree (ERT) process, also known as Extremely Random Trees [242]. In this technique, the process parameters of cutting machine are can be predicted. Müller-Braun et al. [243] investigated the cutting of architectural glass in two stages. In the Stage-I, slit was prepared using a cutting tool and a fluid. The cutting was performed with the cutting wheel. According to the thicknesses, height and properties of glass, the process parameters can be selected for example setting of optimum cutting wheel angle, cutting wheel diameter, cutting speed, cutting force, environmental conditions (temperature and relative humidity) at the time of cutting, and coolant used for cutting. Afterwards the cutting of glass, it is divided into two parts by applying some bending. As mentioned earlier, the edge strength of cut glass depends on the applied cutting parameters of machine. The input or process data obtained from cutting experiments can be used for the prediction purpose. Currently, there is unavailability of modelling technique that can be developed and trained to manage the high correlation results, so far. Vandebroek et al. [205] reported that the glass edge strength is a function of applied stress rate. From the above, literature it is clear that that the ML techniques can be used to economically predict the edge strength of glass by using the process parameters as an input. Extra Trees regressor is similar to the Random

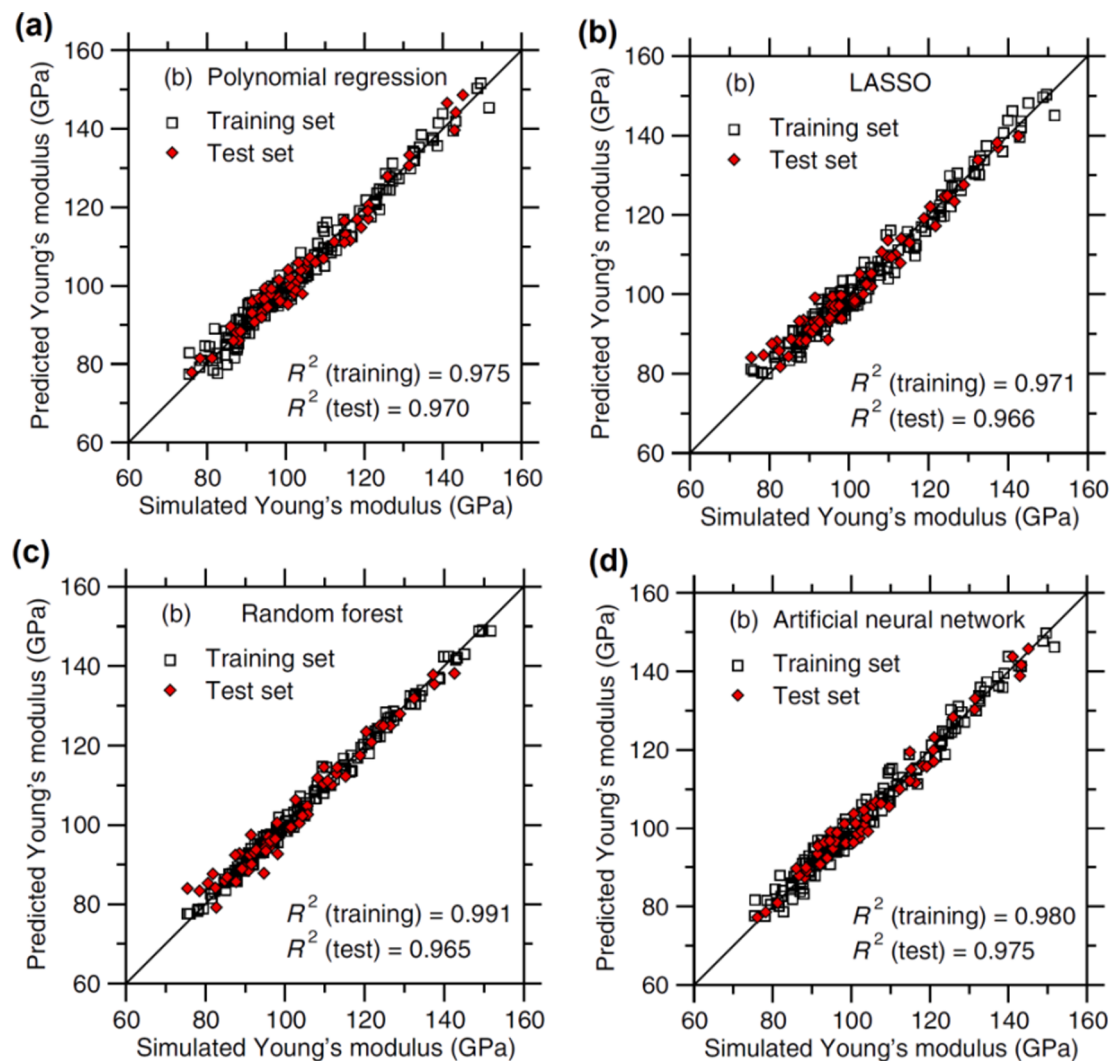


Fig. 35. MD simulated vs. (a) polynomial regression, (b) Lasso, (c) RF, and (d) ANN predicted Young's modulus [191] {Permissions under ©Creative Commons Attribution 4.0 International license}.

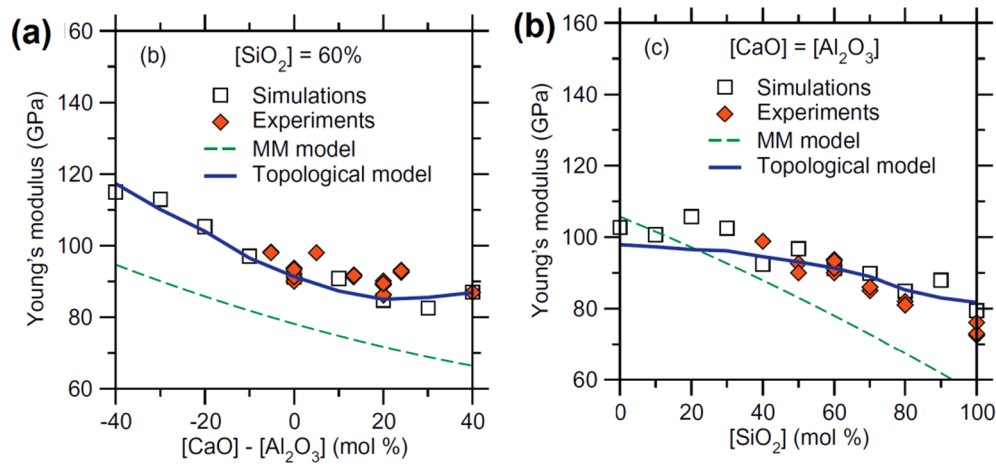


Fig. 36. Comparison between MD simulations computed and ANN predicted Young's modulus with available experimental data [194,197,218–216] for the compositions of (a) $(\text{CaO})_x(\text{Al}_2\text{O}_3)_x(\text{SiO}_2)_{100-2x}$, and (b) $(\text{CaO})_x(\text{Al}_2\text{O}_3)_{40-x}(\text{SiO}_2)_{60}$ [64] {Permissions of ©Elsevier}.

Forest regressor [242]. However, the SciKit-Learn is another ML tool which works with default hyperparameter settings of Extra Trees regressor [121]. In this technique, the single holdout method is used for

the training and testing of dataset and requires no further tuning of hyper-parameter.

The subsequent damage to the edge crack system can vary according

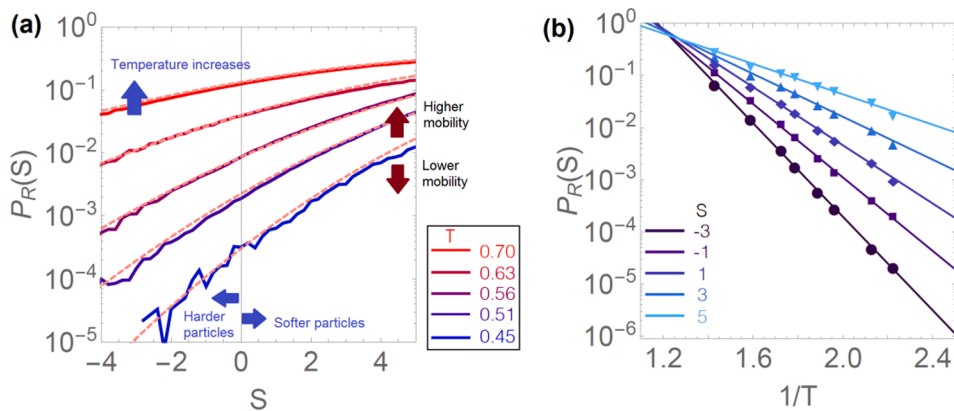


Fig. 37. Probability of rearrangement: (a) Arrhenius form of $P_R(S)$ vs. Softness (S) at different temperatures and (b) $P_R(S)$ as a function of $1/T$ for different softness values predicted by machine learning [228] {Permission under ©Creative Commons Attribution 3.0 licence}.

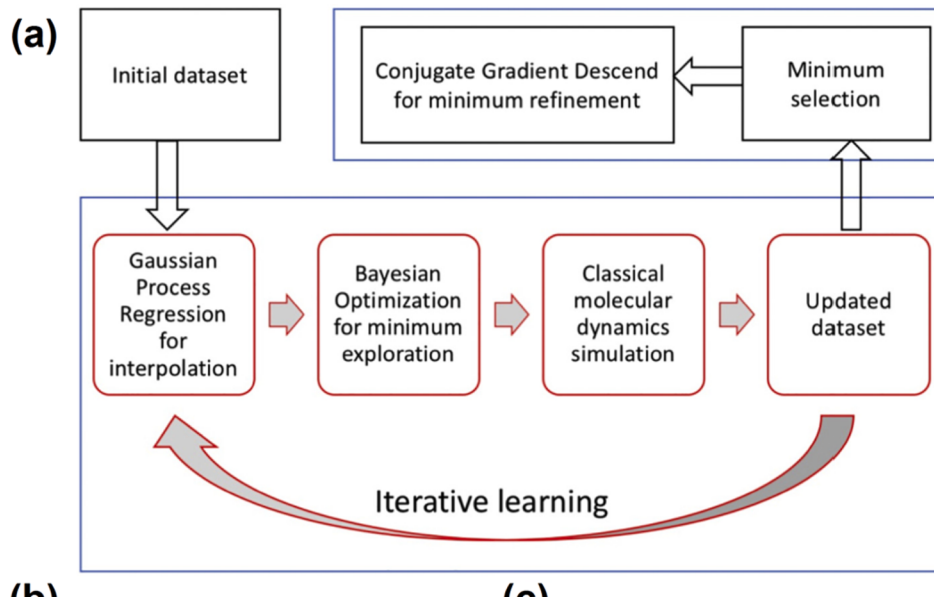
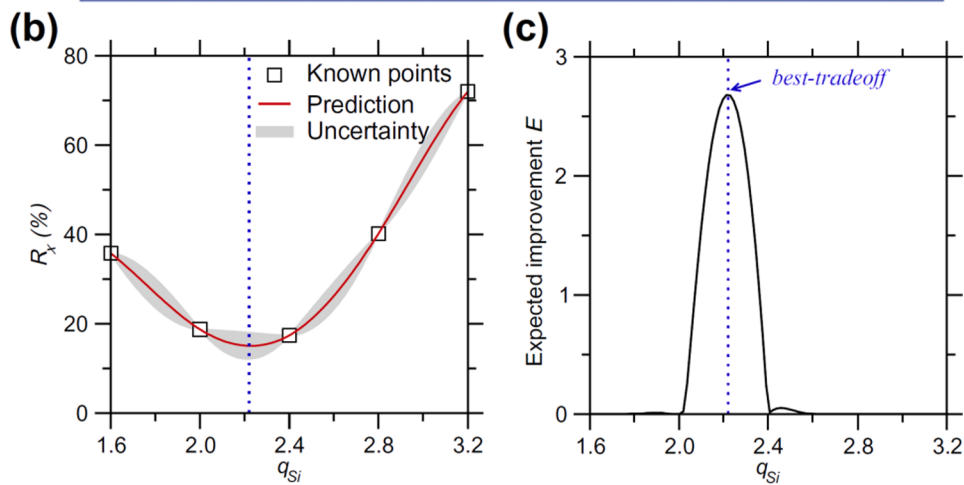


Fig. 38. (a) ML based parametrization strategy, (b, c) Bayesian optimization (BO) methods: [(b) Estimation of the R_x obtained from GPR (red line) in terms of q_{Si} . Training was done by taking 5 data points (black symbols), and validation was done in order to predict results with uncertainty (95% confidence interval) as represented in grey color area and (c) Expected Improvement (EI) function versus q_{Si} . EI predicted the set of parameters i.e. q_{Si} which sets the balance between ‘exploration’ (minimization of the uncertainty in the predictions of model) and ‘exploitation’ (minimization of R_x)] [185] {Permissions of ©Elsevier}. (For interpretation of the references to color in this figure legend, the reader is referred to the web version of this article.)



to cutting process parameters. Furthermore, this nature of crack system may be correlated with the strength of glass [243]. More particularly, the lateral cracks showed these characteristics. Fig. 43 show the flaw depth measured perpendicular to the edge for the calculation of glass edge strength [205]. Vandebroek et al. [205] presented an edge strength model for glass with polished and cut edge finishing and validated it

experimentally. However, the detection of lateral cracks faces a challenge related to accurate geometry. Currently, this is being done with the naked eye or by microscopic techniques due to the crack shape is difficult to detect using modern imaging technology. Then, the marked cracks are processed with image processing technique to take coloured contours. Moreover, the advanced techniques like SEM, TEM, AFM, etc.

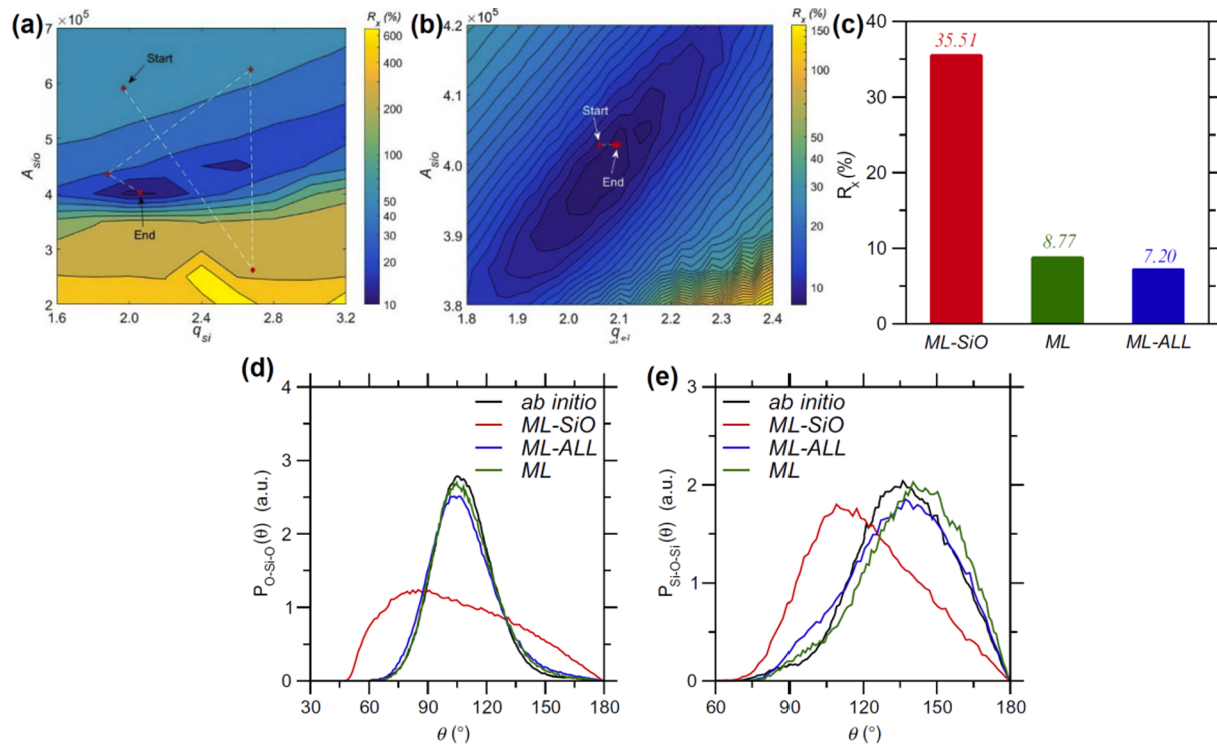


Fig. 39. (a) Iterative optimization approach that represents a path explored by the BO method before a minimum of global value in the cost function (R_χ) in terms of forcefield parameters q_{Si} and A_{SiO} while other forcefield parameters were fixed [Red symbols represent the parameter predicted at a particular iteration by utilizing a training set that involves in prediction of next points. The dotted line follows the path discovered by the BO method until the global minima in R_χ was identified] [185], (b) Final conjugate gradient optimization (CGO) of R_χ in terms of q_{Si} and A_{SiO} [Here, the dotted line represents a path explored by the CGO until the global minima in the R_χ was identified] [185], (c) Comparison of R_χ value so as to increase to complexity in: Si–O interactions (ML-SiO potential), Si–O & O–O interactions (ML potential), and Si–O, O–O, & Si–Si interactions (ML-ALL potential) [185], and (d, e) Comparison of ML predicted [185] and AIMD computed [84] PBADs for [(d) O–Si–O and (e) Si–O–Si] in liquid silica {Permissions of ©Elsevier}. (For interpretation of the references to color in this figure legend, the reader is referred to the web version of this article.)

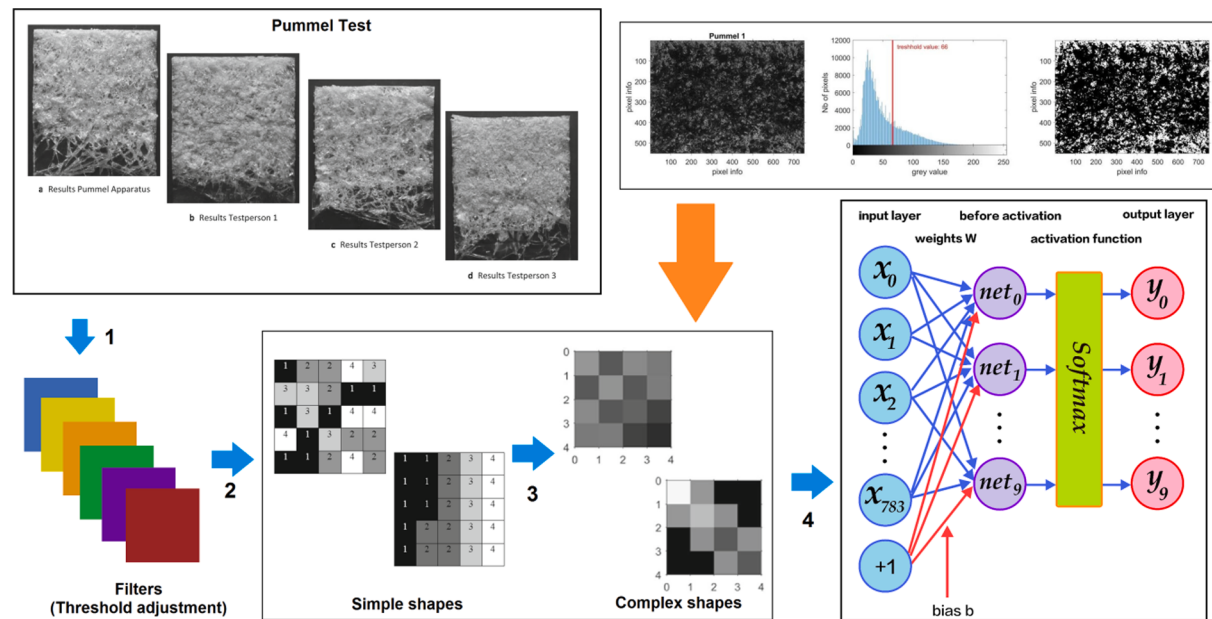


Fig. 40. Proposed architecture of AI supported Pummel test [Pictures of pummel test were taken from Ref. [234]] {Permissions under ©Creative Commons Attribution 4.0 International license}.

are much costlier for testing purpose.

AI and ML algorithms from the field of machine vision can be used to assist manual detection in stopping the glass-cutting methods. In

addition to the substantial time and financial benefits, the identification often comes from objectivity and reproducibility. One of the fields of computer vision and deep learning (DL) is strongly developed as image

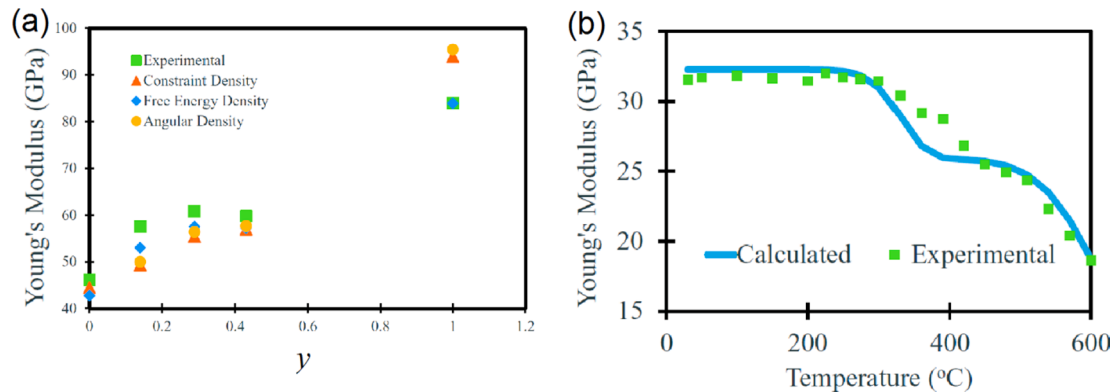


Fig. 41. (a) The Young's modulus prediction and experimentally determined values for $0.3\text{Na}_2\text{O}-0.7(y\text{SiO}_2.(1-y)\text{P}_2\text{O}_5)$ glass and (b) Temperature dependence of the Young's modulus from theory and experiment for $10\% \text{Na}_2\text{O} 90\% \text{B}_2\text{O}_3$ [237] {Permissions under ©Creative Commons CC-BY-NC-ND license}.

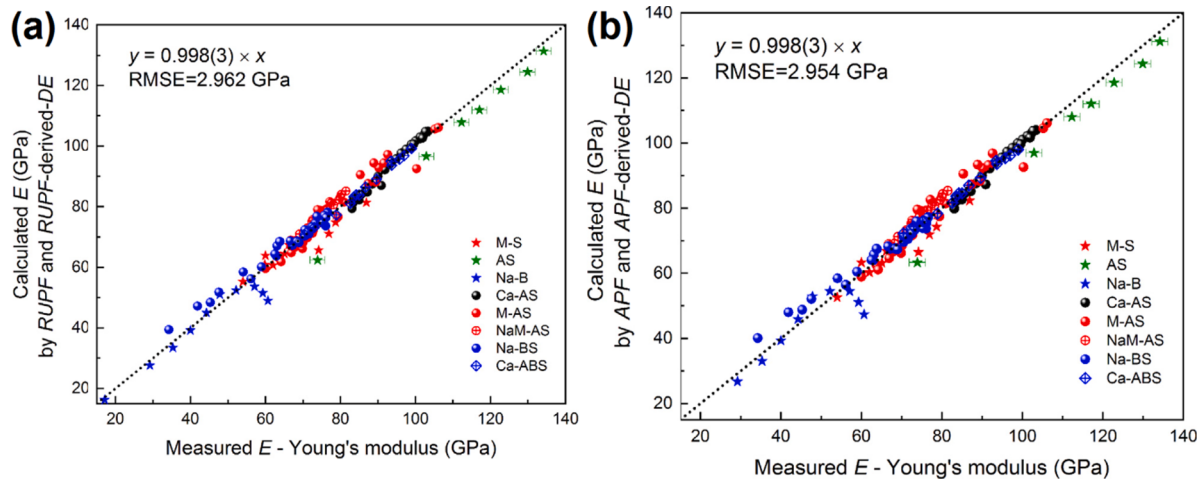


Fig. 42. Measured vs. Shi et al. [238] model predicted Young's modulus {Permissions of ©Elsevier}.

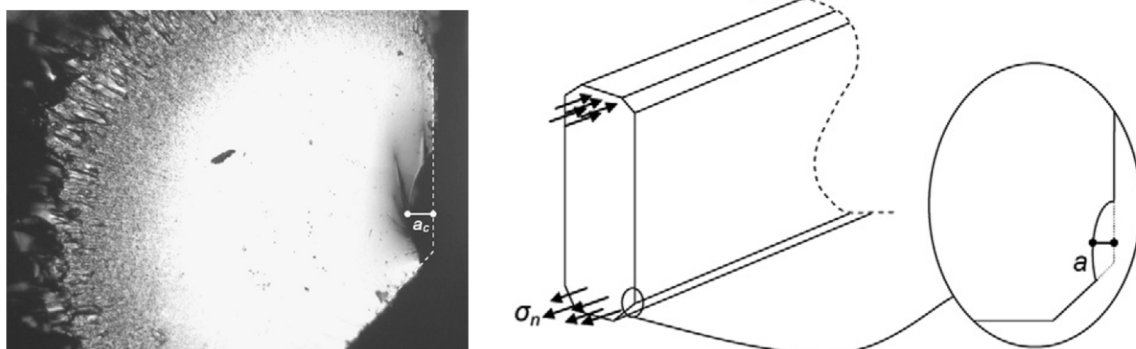
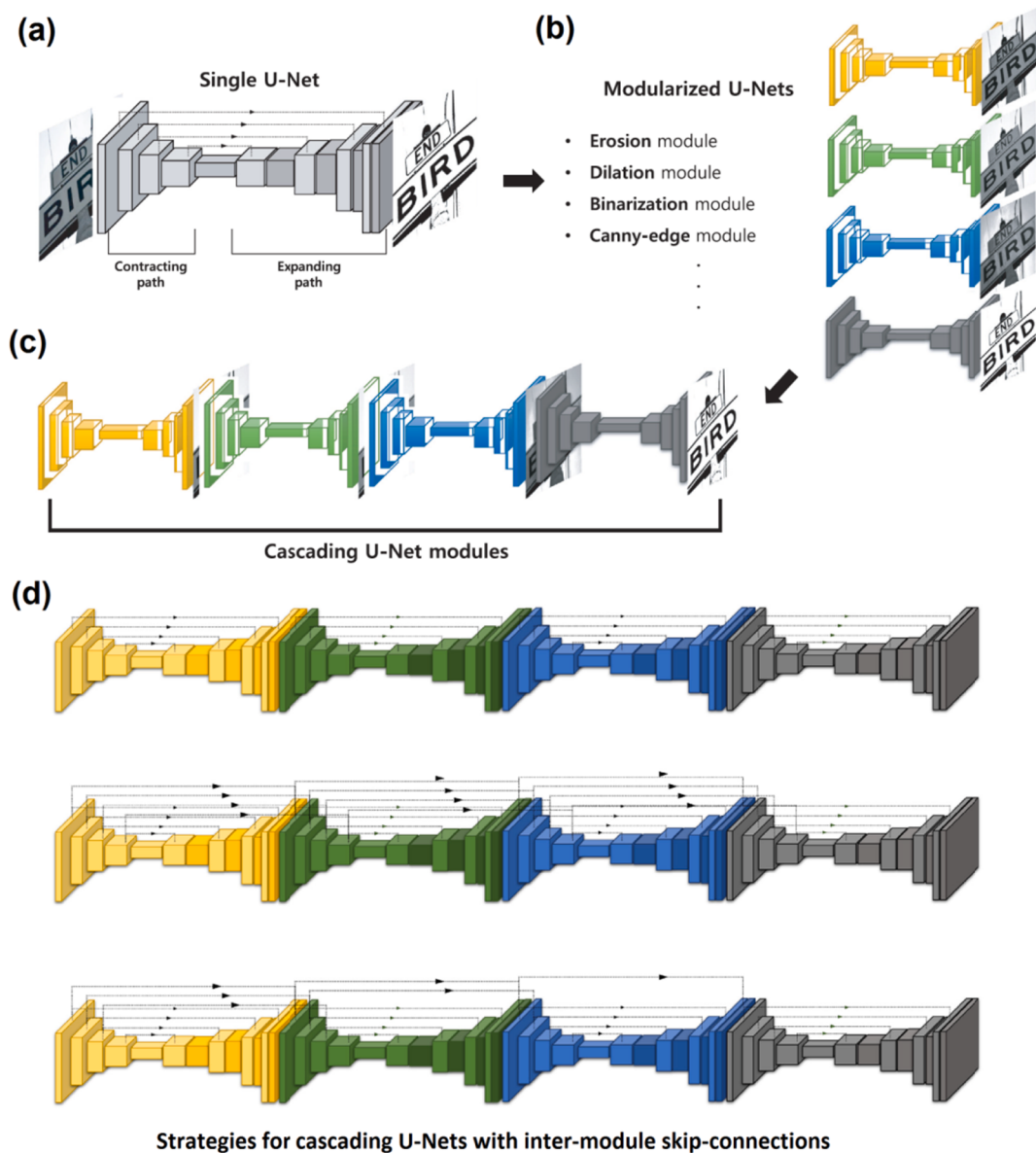


Fig. 43. (a) Picture and (b) schematic view of a broken edge of a glass (its flaw depth measured perpendicular to the edge for the calculation of glass edge) [205] {Permissions of ©Elsevier}.

classification [100]. Image classification is associated with the images i.e. is visual content. The ability to accurately identify an object is important to humans, but achieving that in computer vision applications is difficult [244]. Object identification can be used as an extension of image segmentation, e.g. sorting objects like boxes or frames into images. Semantic segmentation is distinguished from object recognition, which involves assigning a category to each pixel in an image [245]. To do semantic segmentation on an image, the task is to find the boundary between the objects that is called mask. Drass et al. [110,111] used AI and semantic segmentation to automatically produce mask images of

segments the cut edges of glass. Ronneberger et al. [246] also used deep learning model U-Net to create a mask for the edge of a glass cut without writing any programming code for it. In this method, the classification of cut edges of glass was done into “unbroken” and “broken” groups, i.e. binary segmentation was done by the U-Net architecture. According to this method, one can use the original image of the cut glass edges and represented as black colour in the mask, not the mask itself. A full technical description on the U-Net architecture, algorithm, and hyper-parameter tuning are provided by Kang et al. [99]. Fig. 44 shows a typical U-Net architecture [99]. Each U-Net module is developed to



Strategies for cascading U-Nets with inter-module skip-connections

Fig. 44. (a) A proposed model of individual U-Net, (b) U-Net modules used to train the specific image processing task, (c) cascading of U-Net modules (each U-Net model is interconnected with skip-connections), and (d) Cascading strategies with skip-connections [99] {Permissions of ©Elsevier}.

process particular image functions by algorithmic training. The connection components are then cascaded and inter-module skip-connected. A well trained DL U-Net is used to reconstruct a photo-realistic data masks from unlabelled data without the need for more human interference. This shows that the accuracy of the mask image via AI possessed 99% accuracy [99].

7. Conclusions and discussions

In general, machine learning technology provides a rare ability to replace existing glass modelling approaches—a method which has stayed mostly empirical up to now and dependent on past practise. In combination with physics-based simulation, machine learning enables the prevision of glass properties and design according to the structure to be interpolated and extrapolated reliably and robustly and thus dramatically accelerates the innovation of new glass formulations with customised functionality. It can be emphasised that various properties will raise different complexities and levels of difficulty in the adoption of machine learning. The complexity of a given property may be defined

with various parameters, for example:

- Is the composition based on a linear or non-linear basis?
- Is the glass structure of short-range order, or is it still susceptible to the medium range, largely applicable?
- Are such changes in the thermal background of glass greatly influenced example cooling rate?
- How the physical or chemical nature of glass can be perceived?
- How many current data points for particular property are present for experiment or simulation?

There is obviously little gap in the prediction of properties of various levels of complexity by different machine learning algorithms, for instance by polynomial regression predicts simple properties but advanced algorithms (e.g., artificial neural network) are needed to model more “unique and complex properties.” Furthermore, it usually requires larger initial training sets to predict more complicated properties. Despite these obstacles, the potential uses of glass science and technology are exciting and endless. First, machine-learning can predict

the compositional evolution of nearly all glass properties, if sufficient data points are accessible. High performance atomic simulations provide a promising way to produce massive, consistent, precise data, which can be used as training sets for machine learning. Machine learning strategies provide a rare ability in order to create new collections of dependable, convenient, and computationally efficient strength fields for atomic modelling. Around the same time, there are also several advances to be made in the development of modern techniques for using current physical and chemical information of the glass state to inform machine learning for example balance between preciseness, complication, and interpretability. Furthermore, the machine learning will give new physical insight into the essence of the state of the glass, which has been obscured so far owing to the dynamic, disorderly, out of equilibrium framework of glass, through excellence when detecting non-intuitive trends in complex, multi-dimensional datasets. It is believed that further success in these methods would depend heavily on greater cooperation between researchers and innovators that concentrate on trials, theory, simulations and data analysis. In fact, efficient potential implementations of MLM would probably involve interconnected closed loop approaches where (a) the experimental or simulation data are used for training MLMs, (b) MLMs are used to identify promising glass compositions, and (c) tests are carried out for these predictions, or data-led models are refined. We hope that this study will help encourage engineering in glass science and technology to embrace ML technology.

Declaration of Competing Interest

The authors declare that they have no known competing financial interests or personal relationships that could have appeared to influence the work reported in this paper.

References

- [1] E.D. Zanotto, F.A.B. Coutinho, How many non-crystalline solids can be made from all the elements of the periodic table? *J. Non. Cryst. Solids* 347 (1–3) (2004) 285–288, <https://doi.org/10.1016/j.jnoncrysol.2004.07.081>.
- [2] E.D. Zanotto, J.C. Mauro, The glassy state of matter: Its definition and ultimate fate, *J. Non. Cryst. Solids* 471 (March) (2017) 490–495, <https://doi.org/10.1016/j.jnoncrysol.2017.05.019>.
- [3] K. Zheng, Recycled glass concrete, vol. 2010, Woodhead Publishing Limited, 2013.
- [4] J.C. Mauro, Decoding the glass genome, *Curr. Opin. Solid State Mater. Sci.* 22 (2) (2018) 58–64, <https://doi.org/10.1016/j.cossms.2017.09.001>.
- [5] J. Du, Challenges in Molecular Dynamics Simulations of Multicomponent Oxide Glasses, in: *Molecular Simulations of Disordered Materials*, Springer S., vol. 215, C. Massobrio, J. Du, M. Bernasconi, and P. S. Salmon, Eds. Springer International Publishing AG Switzerland, 2015, pp. 157–180.
- [6] X. Li, et al., Cooling rate effects in sodium silicate glasses: Bridging the gap between molecular dynamics simulations and experiments”, *J. Chem. Phys.* 147 (7) (2017) <https://doi.org/10.1063/1.4998611>.
- [7] A.W.K. Hastings, Monte Carlo sampling methods using Markov chains and their applications, *Biometrika* 57 (1) (1970) 97–109, <https://doi.org/10.1093/biomet/57.1.97>.
- [8] M.N. Rosenbluth, Genesis of the Monte Carlo Algorithm for Statistical Mechanics, in: AIP THE MONTE CARLO METHOD IN THE PHYSICAL SCIENCES: Celebrating the 50th Anniversary of the Metropolis Algorithm - Los Alamos, New Mexico (USA) (9–11 June 2003)] AIP Conference Proceedings - Genesis of the Monte Carlo Algorithm for Statistical Mechanics, 2003, pp. 22–30, 10.1063/1.1632112.
- [9] B.J. Alder, T.E. Wainwright, Studies in molecular dynamics. I. General method, *J. Chem. Phys.* 31 (2) (1959) 459–466, <https://doi.org/10.1063/1.1730376>.
- [10] J.B. Gibson, A.N. Goland, M. Milgram, G.H. Vineyard, Dynamics of radiation damage, *Phys. Rev.* 120 (4) (1960) 1229–1253, <https://doi.org/10.1103/PhysRev.120.1229>.
- [11] A. Rehman, Correlations in the motion of atoms in liquid argon, *Phys. Rev.* 136 (2A) (1964) A405–A411, <https://doi.org/10.1007/s002149900020>.
- [12] W.B. Streett, D.J. Tildesley, G. Saville, Multiple time-step methods in molecular dynamics, *Mol. Phys.* 35 (3) (1978) 639–648, <https://doi.org/10.1080/0026897800100471>.
- [13] B. Roux, T. Simonson, Implicit solvent models, *Biophys. Chem.* 78 (1–2) (1999) 1–20, [https://doi.org/10.1016/S0301-4622\(98\)00226-9](https://doi.org/10.1016/S0301-4622(98)00226-9).
- [14] R.E. Skynner, J.L. McDonagh, C.R. Groom, T. Van Mourik, J.B.O. Mitchell, A review of methods for the calculation of solution free energies and the modelling of systems in solution, *Phys. Chem. Chem. Phys.* 17 (9) (2015) 6174–6191, <https://doi.org/10.1039/c5cp00288e>.
- [15] W. Mai, et al., Prism-Based DGTD with a simplified periodic boundary condition to Analyze FSS with D2n symmetry in a rectangular array under normal incidence, *IEEE Antennas Wirel. Propag. Lett.* 18 (4) (2019) 771–775, <https://doi.org/10.1109/LAWP.2019.2902340>.
- [16] L. Zheng, A.A. Alhossary, C.K. Kwoh, Y. Mu, Molecular dynamics and simulation, *Encycl. Bioinforma. Comput. Biol. ABC Bioinforma.* vol. 1–3, no. V (2018) 550–566, <https://doi.org/10.1016/B978-0-12-809633-8.20284-7>.
- [17] C.C. Morris, R.M. Stark, *Fundamentals of calculus*, 1st ed., Wiley, Hoboken, New Jersey, 2015.
- [18] R.A. Lippert, et al., Accurate and efficient integration for molecular dynamics simulations at constant temperature and pressure, *J. Chem. Phys.* 139 (16) (2013), <https://doi.org/10.1063/1.4825247>.
- [19] H. A. Posch, W. G. Hoover, F. J. Vesely, “the Nose oscillator: Stability, order, 33 (6) (1986) 4253–4265.
- [20] G.J. Martyna, M.L. Klein, M. Tuckerman, Nosé–Hoover chains: The canonical ensemble via continuous dynamics, *J. Chem. Phys.* 97 (1992) 2635, <https://doi.org/10.1063/1.463940>.
- [21] H.J.C. Berendsen, J.P.M. Postma, W.F. Van Gunsteren, A. Dinola, J.R. Haak, Molecular dynamics with coupling to an external bath, *J. Chem. Phys.* 81 (8) (1984) 3684–3690, <https://doi.org/10.1063/1.448118>.
- [22] H.C. Andersen, Molecular dynamics simulations at constant pressure and/or temperature, *J. Chem. Phys.* 72 (4) (1980) 2384–2393, <https://doi.org/10.1063/1.439486>.
- [23] X. Shang, M. Kröger, Time correlation functions of equilibrium and nonequilibrium Langevin dynamics: derivations and numerics using random numbers, *arXiv* 62 (4) (2018) 901–935.
- [24] M.J. Uline, D.S. Corti, Molecular dynamics at constant pressure: Allowing the system to control volume fluctuations via a ‘shell’ particle, *Entropy* 15 (9) (2013) 3941–3969, <https://doi.org/10.3390/e15093941>.
- [25] R. Zhou, Replica exchange molecular dynamics method for protein folding simulation, *Methods Mol. Biol.* 350 (November) (2007) 205–223, <https://doi.org/10.1385/1-59745-189-4:205>.
- [26] L. Deng, J. Du, Development of boron oxide potentials for computer simulations of multicomponent oxide glasses, *J. Am. Ceram. Soc.* 102 (5) (2019) 2482–2505, <https://doi.org/10.1111/jace.16082>.
- [27] V.G. Ruiz, W. Liu, A. Tkatchenko, Density-functional theory with screened van der Waals interactions applied to atomic and molecular adsorbates on close-packed and non-close-packed surfaces, *Phys. Rev. B* 93 (3) (2016) 1–17, <https://doi.org/10.1103/PhysRevB.93.035118>.
- [28] M. Park, I.H. Lee, Y.S. Kim, Lattice thermal conductivity of crystalline and amorphous silicon with and without isotopic effects from the ballistic to diffusive thermal transport regime, *J. Appl. Phys.* 116 (4) (2014), <https://doi.org/10.1063/1.4891500>.
- [29] J. Kolafa, J.W. Perram, Cutoff errors in the ewald summation formulae for point charge systems, *Mol. Simul.* 9 (5) (1992) 351–368, <https://doi.org/10.1080/08927029208049126>.
- [30] P. Taylor, Monte Carlo studies of the dielectric properties of water-like models, *Mol. Phys.* 26 (3) (1973) 789–792, <https://doi.org/10.1080/00268977300102101>.
- [31] A.J. Schultz, D.A. Kofke, Sixth, seventh and eighth virial coefficients of the Lennard-Jones model, *Mol. Phys.* 107 (21) (2009) 2309–2318, <https://doi.org/10.1080/00268970903267053>.
- [32] P.G. Huray, *Maxwell’s equations*, Wiley, 2010.
- [33] F.J.A.L. Cruz, J.N. Canongia Lopes, J.C.G. Calado, M.E. Minas Da Piedade, A molecular dynamics study of the thermodynamic properties of calcium apatites. 1. Hexagonal phases, *J. Phys. Chem. B* 109 (51) (2005) 24473–24479, <https://doi.org/10.1021/jp054304p>.
- [34] R.A. Buckingham, The classical equation of state of gaseous helium, neon and argon, *Proc. R. Soc. London. Ser. A. Math. Phys. Sci.* 168 (933) (1938) 264–283, <https://doi.org/10.1098/rspa.1938.0173>.
- [35] J.F. Justo, M.Z. Bazant, E. Kaxiras, Interatomic potential for silicon defects and disordered phases, *Phys. Rev. B - Condens. Matter Mater. Phys.* 58 (5) (1998) 2539–2550, <https://doi.org/10.1103/PhysRevB.58.2539>.
- [36] F. Cleri, V. Rosato, Tight-binding potentials for transition metals and alloys, *Phys. Rev. B* 48 (1) (1993) 22–33, <https://doi.org/10.1103/PhysRevB.48.22>.
- [37] M.S. Daw, S.M. Foiles, M.I. Baskes, The embedded-atom method : a review of theory and applications, *Mater. Sci. Rep.* 9 (June) (1992, 1993,) 251–310.
- [38] J.J.P. Stewart, Optimization of parameters for semiempirical methods II. Applications, *J. Comput. Chem.* 10 (2) (1989) 221–264, <https://doi.org/10.1002/jcc.540100209>.
- [39] R. Hoffmann, An extended Hückel theory. I. Hydrocarbons, *J. Chem. Phys.* 39 (6) (1963) 1397–1412, <https://doi.org/10.1063/1.1734456>.
- [40] D. Lide, *Handbook of Chemistry and Physics*, The Chemical Rubber Publishing Company (CRC), Florida, 1998.
- [41] K. Koperwas, K. Adrjanowicz, Z. Wojnarowska, A. Jedrzejowska, J. Knapik, M. Paluch, Glass-forming tendency of molecular liquids and the strength of the intermolecular attractions, *Sci. Rep.* 6 (November) (2016) 1–10, <https://doi.org/10.1038/srep36934>.
- [42] J.S. Bender, M. Zhi, M.T. Cicerone, M.T. Cicerone, The polarizability response of a glass-forming liquid reveals intrabasin motion and interbasin transitions on a potential energy landscape, *Soft Matter* 16 (24) (2020) 5588–5598, <https://doi.org/10.1039/c9sm02326g>.
- [43] M. Baer, Born – Oppenheimer Approach : Diabatization, in: *Beyond Born–Oppenheimer: Conical Intersections and Electronic Nonadiabatic Coupling Terms*, John Wiley & Sons, Inc, 2006, pp. 26–57.
- [44] S. Kmiecik, D. Gront, M. Kolinski, L. Wieteska, A.E. Dawid, A. Kolinski, Coarse-grained protein models and their applications, *Chem. Rev.* 116 (14) (2016) 7898–7936, <https://doi.org/10.1021/acs.chemrev.6b00163>.

- [45] D.S. Simmons, J.F. Douglas, Nature and interrelations of fast dynamic properties in a coarse-grained glass-forming polymer melt, *Soft Matter* 7 (22) (2011) 11010–11020, <https://doi.org/10.1039/c1sm06189e>.
- [46] J.D. Vienna, J.O. Kroll, P.R. Hrma, J.B. Lang, J.V. Crum, Submixture model to predict nepheline precipitation in waste glasses, *Int. J. Appl. Glas. Sci.* 8 (2) (2017) 143–157, <https://doi.org/10.1111/ijag.12207>.
- [47] D.A. Leach, *Molecular Modelling: Principles and Applications*, 2nd ed., Prentice Hall, Hoboken, New Jersey, Harlow, 2001.
- [48] D.J. Allen, P. Michael, Tildesley, *Computer Simulation of Liquids*, 2nd ed., Oxford University Press, 2017.
- [49] L. Verlet, Computer 'Experiments' on Classical Fluids. I. Thermodynamical Properties of Lennard-Jones Molecules, *Phys. Rev.* 19 (1) (1967) 98–103, <https://doi.org/10.1088/0022-3727/9/2/008>.
- [50] J. Butcher, *Numerical Methods for Ordinary Differential Equations*, John Wiley & Sons, New York, 2008.
- [51] D. Beeman, Some multistep methods for use in molecular dynamics calculations, *J. Comput. Phys.* 20 (2) (1976) 130–139, [https://doi.org/10.1016/0021-9991\(76\)90059-0](https://doi.org/10.1016/0021-9991(76)90059-0).
- [52] V. Kräutler, W.F. Van Gunsteren, P.H. Hünenberger, A fast SHAKE algorithm to solve distance constraint equations for small molecules in molecular dynamics simulations, *J. Comput. Chem.* 22 (5) (2001) 501–508, [https://doi.org/10.1002/1096-987X\(20010415\)22:5<501::AID-JCC1021>3.0.CO;2-V](https://doi.org/10.1002/1096-987X(20010415)22:5<501::AID-JCC1021>3.0.CO;2-V).
- [53] W. Mattson, B.M. Rice, Near-neighbor calculations using a modified cell-linked list method, *Comput. Phys. Commun.* 119 (2) (1999) 135–148, [https://doi.org/10.1016/S0010-4655\(98\)00203-3](https://doi.org/10.1016/S0010-4655(98)00203-3).
- [54] M. Di Pierro, R. Elber, B. Leimkuhler, A stochastic algorithm for the isobaric-isothermal ensemble with ewald summations for all long range forces, *J. Chem. Theory Comput.* 11 (12) (2015) 5624–5637, <https://doi.org/10.1021/acs.jctc.5b00648>.
- [55] S. Toxvaerd, J.C. Dyre, Communication: Shifted forces in molecular dynamics, *J. Chem. Phys.* 134 (8) (2011) 2–6, <https://doi.org/10.1063/1.3558787>.
- [56] A.Y. Toukmaji, J.A. Board, Ewald summation techniques in perspective: a survey, *Comput. Phys. Commun.* 95 (2–3) (1996) 73–92, [https://doi.org/10.1016/0010-4655\(96\)00016-1](https://doi.org/10.1016/0010-4655(96)00016-1).
- [57] M. Born, R. Oppenheimer, Zur Quantentheorie der Moleküle, *Ann. Phys.* 389 (20) (1927) 457–484, <https://doi.org/10.1002/andp.19273892002>.
- [58] D.J.E. Callaway, A. Rahman, Microcanonical ensemble formulation of lattice gauge theory, *Phys. Rev. Lett.* 49 (9) (1982) 613–616, <https://doi.org/10.1103/PhysRevLett.49.613>.
- [59] S. Hassani, *Mathematical Methods: For Students of Physics and Related Fields*, 2nd ed., Springer-Verlag, London, 2008.
- [60] J.C. Mauro, E.D. Zanotto, Two centuries of glass research: historical trends, current status, and grand challenges for the future, *Int. J. Appl. Glas. Sci.* 5 (3) (2014) 313–327, <https://doi.org/10.1111/ijag.12087>.
- [61] J.C. Mauro, C.S. Philip, D.J. Vaughn, M.S. Pambianchi, Glass science in the United States: current status and future directions, *Int. J. Appl. Glas. Sci.* 5 (1) (2014) 2–15, <https://doi.org/10.1111/ijag.12058>.
- [62] S.S. Fouad, Topology of covalent non-crystalline solids: Short-range order in SeyGexSb_{1-x-y} alloys, *Phys. B Phys. Condens. Matter* 215 (2–3) (1995) 213–216, [https://doi.org/10.1016/0921-4526\(95\)00390-U](https://doi.org/10.1016/0921-4526(95)00390-U).
- [63] J.C. Mauro, A. Tandia, K.D. Vargheese, Y.Z. Mauro, M.M. Smedskjaer, Accelerating the design of functional glasses through modeling, *Chem. Mater.* 28 (12) (2016) 4267–4277, <https://doi.org/10.1021/acs.chemmater.6b01054>.
- [64] K. Yang, B. Yang, X. Xu, C. Hoover, M.M. Smedskjaer, M. Bauchy, Prediction of the Young's modulus of silicate glasses by topological constraint theory, *J. Non. Cryst. Solids* 514 (March) (2019) 15–19, <https://doi.org/10.1016/j.jnoncrysol.2019.03.033>.
- [65] M.M. Smedskjaer, J.C. Mauro, Y. Yue, Prediction of glass hardness using temperature-dependent constraint theory, *Phys. Rev. Lett.* 105 (11) (2010) 10–13, <https://doi.org/10.1103/PhysRevLett.105.115503>.
- [66] R.L. McGreevy, L. Puszta, Reverse Monte Carlo simulation: a new technique for the determination of disordered structures, *Mol. Simul.* 1 (6) (1988) 359–367, <https://doi.org/10.1080/089270288080958>.
- [67] R.L. McGreevy, Reverse Monte Carlo modelling, *J. Phys. Condens. Matter* 13 (46) (2001), <https://doi.org/10.1088/0953-8984/13/46/201>.
- [68] A.K. Soper, Partial structure factors from disordered materials diffraction data: an approach using empirical potential structure refinement, *Phys. Rev. B - Condens. Matter Mater. Phys.* 72 (10) (2005) 1–12, <https://doi.org/10.1103/PhysRevB.72.104204>.
- [69] A. Zandonà, C. Patzig, B. Rüdinger, O. Hochrein, J. Deubener, TiO₂(B) nanocrystals in Ti-doped lithium aluminosilicate glasses, *J. Non-Crystalline Solids X* 2 (December) (2019) 100025, <https://doi.org/10.1016/j.jncox.2019.100025>.
- [70] R. Sen, N.N.G. Boetti, M. Hokka, L. Petit, Optical, structural and luminescence properties of oxyfluoride phosphate glasses and glass-ceramics doped with Yb³⁺, *J. Non-Crystalline Solids X* 1 (January) (2019) 100003, <https://doi.org/10.1016/j.jncox.2018.100003>.
- [71] M. Wang, N.M. Anoop Krishnan, B. Wang, M.M. Smedskjaer, J.C. Mauro, M. Bauchy, A new transferable interatomic potential for molecular dynamics simulations of borosilicate glasses, *J. Non. Cryst. Solids* 498 (December 2017) (2018) 294–304, <https://doi.org/10.1016/j.jnoncrysol.2018.04.063>.
- [72] M. Bauchy, Structural, vibrational, and thermal properties of densified silicates: insights from molecular dynamics, *J. Chem. Phys.* 137 (4) (2012) 15733, <https://doi.org/10.1063/1.4738501>.
- [73] R. Atta-Fynn, D.A. Drabold, P. Biswas, First principles modeling of the structural, electronic, and vibrational properties of Ni 40 Pd 40 P 20 bulk metallic glass,
- [74] J. Non-Crystalline Solids X 1 (October 2018) (2019) 100004, <https://doi.org/10.1016/j.jncox.2018.100004>.
- [75] W. Takeda, C.J. Wilkinson, S.A. Feller, J.C. Mauro, Topological constraint model of high lithium content borate glasses, *J. Non-Crystalline Solids X* 3 (June) (2019) 100028, <https://doi.org/10.1016/j.jncox.2019.100028>.
- [76] M. Benoit, S. Ispas, P. Jund, R. Jullien, Model of silica glass from combined classical and ab initio molecular-dynamics simulations, *Eur. Phys. J. B* 13 (4) (2000) 631–636, <https://doi.org/10.1007/s100510050079>.
- [77] R.M. Van Ginneken, H. Jónsson, L.R. Corrales, Silica glass structure generation for ab initio calculations using small samples of amorphous silica, *Phys. Rev. B - Condens. Matter Mater. Phys.* 71 (2) (2005) 1–15, <https://doi.org/10.1103/PhysRevB.71.024208>.
- [78] T. Oey, et al., Topological controls on the dissolution kinetics of glassy aluminosilicates, *J. Am. Ceram. Soc.* 100 (2017) 5521–5527, <https://doi.org/10.1111/jace.15122>.
- [79] T. Oey, et al., The role of the network-modifier's field-strength in the chemical durability of aluminoborate glasses, *J. Non. Cryst. Solids* 505 (October 2018) (2019) 279–285, <https://doi.org/10.1016/j.jnoncrysol.2018.11.019>.
- [80] E.D. Cubuk, S.S. Schoenholz, E. Kaxiras, A.J. Liu, Structural properties of defects in glassy liquids, *J. Phys. Chem. B* 120 (26) (2016) 6139–6146, <https://doi.org/10.1021/acs.jpcb.6b02144>.
- [81] X. Ma, et al., Heterogeneous activation, local structure, and softness in supercooled colloidal liquids, *Phys. Rev. Lett.* 122 (2) (2019) 28001, <https://doi.org/10.1103/PhysRevLett.122.028001>.
- [82] M. Bauchy, Structural, vibrational, and elastic properties of a calcium aluminosilicate glass from molecular dynamics simulations: The role of the potential, *J. Chem. Phys.* 141 (2) (2014), <https://doi.org/10.1063/1.4886421>.
- [83] S. Sundaraman, L. Huang, S. Ispas, W. Kob, New optimization scheme to obtain interaction potentials for oxide glasses, *J. Chem. Phys.* 148 (19) (2018), <https://doi.org/10.1063/1.5023707>.
- [84] A. Carré, S. Ispas, J. Horbach, W. Kob, Developing empirical potentials from ab initio simulations: the case of amorphous silica, *Comput. Mater. Sci.* 124 (2016) 323–334, <https://doi.org/10.1016/j.commatsci.2016.07.041>.
- [85] A. Carré, J. Horbach, S. Ispas, W. Kob, New fitting scheme to obtain effective potential from Car-Parrinello molecular-dynamics simulations: application to silica, *Epl* 82 (1) (2008), <https://doi.org/10.1209/0295-5075/82/17001>.
- [86] S. Lan, et al., Hidden amorphous phase and reentrant supercooled liquid in Pd-Ni-P metallic glasses, *Nat. Commun.* 8 (2017) 1–8, <https://doi.org/10.1038/ncomms14679>.
- [87] B.J. Nordell, et al., Topological constraint theory analysis of rigidity transition in highly coordinate amorphous hydrogenated boron carbide, *Front. Mater.* 6 (October) (2019) 1–11, <https://doi.org/10.3389/fmats.2019.00264>.
- [88] J.C. Mauro, Topological constraint theory of glass, *Am. Ceram. Soc. Bull.* 90 (4) (2011) 31–37.
- [89] J.C. Phillips, M.F. Thorpe, Constraint theory, vector percolation and glass formation, *Solid State Commun.* 53 (8) (1985) 699–702, [https://doi.org/10.1016/0038-1098\(85\)90381-3](https://doi.org/10.1016/0038-1098(85)90381-3).
- [90] M. Micoulaut, J.C. Phillips, Onset of rigidity in glasses: From random to self-organized networks, *J. Non. Cryst. Solids* 353 (18–21) (2007) 1732–1740, <https://doi.org/10.1016/j.jnoncrysol.2007.01.078>.
- [91] H. He, M.F. Thorpe, Elastic properties of glasses, *Phys. Rev. Lett.* 42 (19) (1985) 2107–2110, <https://doi.org/10.1111/j.1151-2916.1959.tb12953.x>.
- [92] M. Smedskjaer, J.C. Mauro, S. Sen, Y. Yue, Quantitative design of glassy materials using temperature-dependent constraint theory, *Chem. Mater.* 22 (18) (2010) 5358–5365, <https://doi.org/10.1021/cm1016799>.
- [93] J.C. Mauro, P.K. Gupta, R.J. Loucks, Composition dependence of glass transition temperature and fragility. II. A topological model of alkali borate liquids, *J. Chem. Phys.* 130 (23) (2009), <https://doi.org/10.1063/1.3152432>.
- [94] S. Koritala, et al., The glass transition temperature of lithium-alkali borates, *J. Non. Cryst. Solids* 134 (3) (1991) 277–286, [https://doi.org/10.1016/0022-3093\(91\)90386-K](https://doi.org/10.1016/0022-3093(91)90386-K).
- [95] J. Marchwinski, Architectural evaluation of switchable glazing technologies as sun protection measure, *Energy Procedia* 57 (2014) 1677–1686, <https://doi.org/10.1016/j.egypro.2014.10.158>.
- [96] E. Alcobaça, et al., Explainable machine learning algorithms for predicting glass transition temperatures, *Acta Mater.* 188 (2020) 92–100, <https://doi.org/10.1016/j.actamat.2020.01.047>.
- [97] D.S. Bulgarevich, S. Tsukamoto, T. Kasuya, M. Demura, M. Watanabe, Pattern recognition with machine learning on optical microscopy images of typical metallurgical microstructures, *Sci. Rep.* 8 (1) (2018) 3–9, <https://doi.org/10.1038/s41598-018-20438-6>.
- [98] G. Shobha and S. Rangaswamy, Machine Learning, first ed., vol. 38. Elsevier B.V., 2018.
- [99] J. Frochte, *Maschinelles Lernen: Grundlagen und Algorithmen in Python*, Carl Hanser Verlag GmbH Co KG 2020.
- [100] A. Ferreyra-Ramirez, C. Aviles-Cruz, E. Rodriguez-Martinez, J. Villegas-Cortez, A. Zuñiga-Lopez, An Improved Convolutional Neural Network Architecture for Image Classification, in: *Pattern Recognition, 11th Mexican Conference, MCPR 2019 Querétaro, Mexico, June 26–29, 2019 Proceedings*, Lecture No., J. A. Carrasco, J. F. Martínez, J. A. Olvera, and J. Salas, Eds. Cham: Springer Nature Switzerland AG, 2020, pp. 89–104.

- [101] S. Raschka, Model evaluation, model selection, and algorithm selection in machine learning, *arXiv*, 2018.
- [102] Y. Lecun, Y. Bengio, G. Hinton, Deep learning, *Nature* 521 (7553) (2015) 436–444, <https://doi.org/10.1038/nature14539>.
- [103] A. Vouliodimos, N. Doulamis, A. Doulamis, E. Protopapadakis, Deep learning for computer vision: a brief review, *Comput. Intell. Neurosci.* 2018 (2018), <https://doi.org/10.1155/2018/7068349>.
- [104] J. Brownlee, Machine learning mastery with python: understand your data, create accurate models, and work projects end-to-end, V1.20, *Machine Learning Mastery* (2021).
- [105] S. Vyas, S.S. Jain, I. Choudhary, A. Chaudhary, Study on Use of AI and Big Data for Commercial System, *Proc. - 2019 Amity Int. Conf. Artif. Intell. AICAI 2019*, pp. 737–739, 2019, 10.1109/AICAI.2019.8701361.
- [106] O. Rusu, et al., Converting unstructured and semi-structured data into knowledge, *Proc. - RoEduNet IEEE Int. Conf.*, November 2015 (2013), <https://doi.org/10.1109/RoEduNet.2013.6511736>.
- [107] M. Pathirana, N. Lam, S. Perera, L. Zhang, D. Ruan, E. Gad, Risks of failure of annealed glass panels subject to point contact actions, *Int. J. Solids Struct.* 129 (2017) 177–194, <https://doi.org/10.1016/j.ijsolstr.2017.09.001>.
- [108] K. Varmuza, *Clustering Methods, Data Mining And Knowledge Discovery handbook* 1980 (May 2014) 92–96.
- [109] S. Burrows, B. Stein, J. Frochte, D. Wiesner, K. Müller, Simulation data mining for supporting bridge design, *Conf. Res. Pract. Inf. Technol. Ser.* 121 (2010) 163–170.
- [110] M. Drass, M.A. Kraus, Semi-probabilistic calibration of a partial material safety factor for structural silicone adhesives - Part I: derivation, *Int. J. Struct. Glas. Adv. Mater. Res.* 4 (1) (2020) 56–68, <https://doi.org/10.3844/sgamrsp.2020.56.68>.
- [111] M. Drass, H. Berthold, M.A. Kraus, S. Müller-Braun, Semantic segmentation with deep learning: detection of cracks at the cut edge of glass, *Glas. Struct. Eng.* 6 (1) (2021) 21–37, <https://doi.org/10.1007/s40940-020-00133-7>.
- [112] M. Kuhn, K. Johnson, Applied predictive modeling. (2013).
- [113] E. Hancer, B. Xue, M. Zhang, A survey on feature selection approaches for clustering, *Artif. Intell. Rev.* 53 (6) (2020) 4519–4545, <https://doi.org/10.1007/s10462-019-09800-w>.
- [114] M.I. Jordan, T.M. Mitchell, Machine learning: Trends, perspectives, and prospects, *Science* (80-.). 349 (6245) (2015) 255–260.
- [115] S. Efronovich, *The Multivariate Normal Distribution*, Springer Series in Statistics, Springer-Verlag, Ney York, 1999.
- [116] Y. Liu, T. Zhao, W. Ju, S. Shi, S. Shi, S. Shi, Materials discovery and design using machine learning, *J. Mater.* 3 (3) (2017) 159–177, <https://doi.org/10.1016/j.jmat.2017.08.002>.
- [117] C.J. Wilmott, K. Matsuura, Advantages of the mean absolute error (MAE) over the root mean square error (RMSE) in assessing average model performance, *Clim. Res.* 30 (1) (2005) 79–82, <https://doi.org/10.3354/cr030079>.
- [118] M. Hagan, M.T. Menhaj, Training feedforward networks with the Marquardt algorithm, *IEEE Trans. Neural Netw.* 5 (1994) 989–993.
- [119] L.C. Lee, C.Y. Liong, A.A. Jemain, Validity of the best practice in splitting data for hold-out validation strategy as performed on the ink strokes in the context of forensic science, *Microchem. J.* 139 (2018) 125–133, <https://doi.org/10.1016/j.microc.2018.02.009>.
- [120] F. Emmert-Streib, M. Dehmer, Evaluation of regression models: model assessment, model selection and generalization error, *Mach. Learn. Knowl. Extr.* 1 (1) (2019) 521–551, <https://doi.org/10.3390/make1010032>.
- [121] F. Pedregosa, et al., Scikit-learn: machine learning in python, *J. Mach. Learn. Res.* 12 (2011) 2825–2830, <https://doi.org/10.1289/EHP4713>.
- [122] E. Halilaj, A. Rajagopal, M. Fiterau, J.L. Hicks, T.J. Hastie, S.L. Delp, Machine learning in human movement biomechanics: Best practices, common pitfalls, and new opportunities, *J. Biomech.* 81 (2018) 1–11, <https://doi.org/10.1016/j.jbiomech.2018.09.009>.
- [123] M.-W. Chang, et al., *Artificial Intelligence*, 4th ed., Pearson Education Inc, Hoboken, New Jersey, 2020.
- [124] Z. Xiong, Y. Cui, Z. Liu, Y. Zhao, M. Hu, J. Hu, Evaluating explorative prediction power of machine learning algorithms for materials discovery using k-fold forward cross-validation, *Comput. Mater. Sci.* 171 (2019) (2020), <https://doi.org/10.1016/j.commatsci.2019.109203>.
- [125] Z.Y. Algamaal, Shrinkage parameter selection via modified cross-validation approach for ridge regression model, *Commun. Stat. Simul. Comput.* 49 (7) (2020) 1922–1930, <https://doi.org/10.1080/03610918.2018.1508704>.
- [126] R.R. Wilcox, Multicollinearity and ridge regression: results on type I errors, power and heteroscedasticity, *J. Appl. Stat.* 46 (5) (2019) 946–957, <https://doi.org/10.1080/02664763.2018.1526891>.
- [127] N. Li, H. Yang, J. Yang, Nonnegative estimation and variable selection via adaptive elastic-net for high-dimensional data, *Commun. Stat. - Simul. Comput.* (2019) 1–17, <https://doi.org/10.1080/03610918.2019.1642484>.
- [128] Y. Wang, X.G. Yang, Y. Lu, Informative gene selection for microarray classification via adaptive elastic net with conditional mutual information, *Appl. Math. Model.* 71 (February) (2019) 286–297, <https://doi.org/10.1016/j.apm.2019.01.044>.
- [129] E.A. Hunter, R.J. Brook, G.C. Arnold, Applied regression analysis and experimental design, *Appl. Stat.* 35 (1) (1986) 77, <https://doi.org/10.2307/2347870>.
- [130] G. G. V. Douglas C. Montgomery, Elizabeth A. Peck, Introduction to linear regression analysis, 5th Editio. Wiley series in probability and Statistics, 2012.
- [131] G.M. Nielson, Some Piecewise Polynomial alternatives to splines under tension, no. 044, ACADEMIC PRESS, INC., 1974.
- [132] H.J. Motulsky, L.A. Ransnas, Fitting curves nonlinear regression : review a practical, *FASEB J.* 1 (5) (1987) 365–374.
- [133] P. Čížek, S. Sadıkoglu, Robust nonparametric regression: a review, *Wiley Interdiscip. Rev. Comput. Stat.* 12 (3) (2020) 1–16, <https://doi.org/10.1002/wics.1492>.
- [134] N.S. Altman, An introduction to kernel and nearest-neighbor nonparametric regression, *Am. Stat.* 46 (3) (1992) 175–185, <https://doi.org/10.1080/00031305.1992.10475879>.
- [135] D. Fan, X. Zhang, Short-term traffic flow prediction method based on balanced binary tree and K-nearest neighbor nonparametric regression, *Adv. Intell. Syst. Res.* 132 (2017) 118–121, <https://doi.org/10.2991/msam-17.2017.27>.
- [136] M. Raissi, P. Perdikaris, G.E. Karniadakis, Machine learning of linear differential equations using Gaussian processes, *J. Comput. Phys.* 348 (2017) 683–693, <https://doi.org/10.1016/j.jcp.2017.07.050>.
- [137] S. Bishnoi, et al., Predicting Young's modulus of oxide glasses with sparse datasets using machine learning, *J. Non. Cryst. Solids* vol. 524, no. August (2019), 119643, <https://doi.org/10.1016/j.jnoncrysol.2019.119643>.
- [138] E. Ostertagová, Modelling using polynomial regression, *Procedia Eng.* 48 (2012) 500–506, <https://doi.org/10.1016/j.proeng.2012.09.545>.
- [139] Z. Rustam, F. Yaurita, Insolvency prediction in insurance companies using support vector machines and fuzzy kernel C-means, *J. Phys. Conf. Ser.* 1028 (1) (2018), <https://doi.org/10.1088/1742-6596/1028/1/012118>.
- [140] G. Villarrubia, J.F. De Paz, P. Chamoso, F. De la Prieta, Artificial neural networks used in optimization problems, *Neurocomputing* 272 (2018) 10–16, <https://doi.org/10.1016/j.neucom.2017.04.075>.
- [141] J.S. Raj, V. Ananth, Recurrent Neural Networks and LSTM explained, *J. Soft Comput. Paradig.*, 01(01), pp. 33–40, 2019, [Online]. Available: <https://medium.com/@purnasaiiguandikula/recurrent-neural-networks-and-lstm-explained-7f51c7f6bbb9>.
- [142] B. Deng, Machine learning on density and elastic property of oxide glasses driven by large dataset, *J. Non. Cryst. Solids* 529 (November 2019) (2020), <https://doi.org/10.1016/j.jnoncrysol.2019.119768>.
- [143] J.H. Friedman, Greedy functional approximation: a gradient boosting machine, *Ann. Stat.* 29 (5) (2001) 1189–1232, <https://doi.org/10.1214/aos/1013203451>.
- [144] A.L. Pomerantsev, Confidence intervals for nonlinear regression extrapolation, *Chemom. Intell. Lab. Syst.* 49 (1) (1999) 41–48, [https://doi.org/10.1016/S0169-7439\(99\)00026-X](https://doi.org/10.1016/S0169-7439(99)00026-X).
- [145] Y. Wei, F. Yang, M.J. Wainwright, Early stopping for kernel boosting algorithms: a general analysis with localized complexities, *IEEE Trans. Inf. Theory* 65 (10) (2019) 6685–6703, <https://doi.org/10.1109/TIT.2019.2927563>.
- [146] D. Cittanti, A. Ferraris, A. Airale, S. Fiorot, S. Scavuzzo, M. Carello, Modeling Li-ion batteries for automotive application: A trade-off between accuracy and complexity, in: International Conference of Electrical and Electronic Technologies for Automotive, Turin, Italy, 2017, pp. 1–8, 10.23919/EETA.2017.7993213.
- [147] Z. Wang, et al., Fully memristive neural networks for pattern classification with unsupervised learning, *Nat. Electron.* 1 (2) (2018) 137–145, <https://doi.org/10.1038/s41928-018-0023-2>.
- [148] R. Gholami, N. Fakhri, SUPPORT vector machine : principles, parameters, and applications, in: *Handbook of Neural Computation*, 1st ed., Elsevier Inc., 2017, pp. 515–535.
- [149] B.G. Horne, Progress in supervised neural networks, *Signal Process. Mag. IEEE* 10 (1) (1993) 8–39.
- [150] R. Pascanu, T. Mikolov, Y. Bengio, On the difficulty of training recurrent neural networks Razvan, *International conference on machine learning (2013)* 1310–1318.
- [151] L. Liu, W. Huang, C. Wang, Hyperspectral image classification with kernel-based least-squares support vector machines in sum space, *IEEE J. Sel. Top. Appl. Earth Obs. Remote Sens.* 11 (4) (2018) 1144–1157, <https://doi.org/10.1109/JSTARS.2017.2768541>.
- [152] Y. Liu, J. Wu, G. Yang, T. Zhao, S. Shi, Predicting the onset temperature (T_g) of Ge_xSe_{1-x} glass transition: a feature selection based two-stage support vector regression method, *Sci. Bull.* 64 (16) (2019) 1195–1203, <https://doi.org/10.1016/j.scib.2019.06.026>.
- [153] C. Bai, L. Huang, X. Pan, J. Zheng, S. Chen, Optimization of deep convolutional neural network for large scale image retrieval, *Neurocomputing* 303 (2018) 60–67, <https://doi.org/10.1016/j.neucom.2018.04.034>.
- [154] J. Ortegon, R. Ledesma-Alonso, R. Barbosa, J. Vázquez Castillo, A. Castillo Atoche, Material phase classification by means of Support Vector Machines, *Comput. Mater. Sci.* 148 (2018) 336–342, <https://doi.org/10.1016/j.commatsci.2018.02.054>.
- [155] S. Hochreiter, J. Schmidhuber, Long short-term memory, *Neural Comput.* 9 (8) (1997) 1735–1780, <https://doi.org/10.17582/journal.pjz/2018.50.6.2199.2207>.
- [156] M. T. Camacho Olmedo, M. Paegelow, J. F. Mas, F. Escobar, Geomatic Approaches for Modeling Land Change Scenarios. An Introduction, no. January 2020. Cham, Switzerland: Springer Nature, 2018.
- [157] C.C.J. Kuo, Understanding convolutional neural networks with a mathematical model, *J. Vis. Commun. Image Represent.* 41 (2016) 406–413, <https://doi.org/10.1016/j.jvcir.2016.11.003>.
- [158] F.A. Spanhol et al., Breast Cancer Histopathological Im1. Spanhol FA, Oliveira LS, Petitjean C, Heutte L. Breast Cancer Histopathological Image Classification using Convolutional Neural Networks, in: *Int J Conf Neural Networks (IJCNN 2016)*. 2016.age Classification using Convolut, *Int. Jt. Conf. Neural Networks (IJCNN 2016)*, vol. 2017-Janua, pp. 1868–1873, 2017.
- [159] M. Kouzehgar, Y. Krishnasamy Tamilselvam, M. Vega Heredia, M. Rajesh Elara, Self-reconfigurable façade-cleaning robot equipped with deep-learning-based crack detection based on convolutional neural networks, *Autom. Constr.* 108 (January) (2019), 102959, <https://doi.org/10.1016/j.autcon.2019.102959>.

- [160] I. Goodfellow, et al., Generative adversarial networks, *Commun. ACM* 63 (11) (2020) 139–144, <https://doi.org/10.1145/3422622>.
- [161] Y. Dan, Y. Zhao, “Generative adversarial networks (GAN) based efficient sampling of chemical composition space for inverse design of inorganic materials, *npj Comput Mater.* 6 (84) (2020) 1–7, <https://doi.org/10.1038/s41524-020-00352-0>.
- [162] A. Taherkhani, G. Cosma, T.M. McGinnity, AdaBoost-CNN: An adaptive boosting algorithm for convolutional neural networks to classify multi-class imbalanced datasets using transfer learning, *Neurocomputing* 404 (2020) 351–366, <https://doi.org/10.1016/j.neucom.2020.03.064>.
- [163] A.C. Benabdellah, A. Benghabrit, I. Bouhaddou, A survey of clustering algorithms for an industrial context, *Procedia Comput. Sci.* 148 (2019) 291–302, <https://doi.org/10.1016/j.procs.2019.01.022>.
- [164] P. Nerurkar, A. Shirke, M. Chandane, S. Bhirud, Empirical analysis of data clustering algorithms, *Procedia Comput. Sci.* 125 (2018) 770–779, <https://doi.org/10.1016/j.procs.2017.12.099>.
- [165] B. Basaran, F. Günes, Data clustering, *Intell. Multidimens. data Clust. Anal.* 31 (3) (2016) 28–72, <https://doi.org/10.4018/978-1-5225-1776-4.ch002>.
- [166] J. Yu, H. Huang, S. Tian, Cluster validity and stability of clustering algorithms, *Lect. Notes Comput. Sci. (including Subser. Lect. Notes Artif. Intell. Lect. Notes Bioinformatics)* 3138 (3) (2004) 957–965, https://doi.org/10.1007/978-3-540-27868-9_105.
- [167] M.G.H. Omran, A.P. Engelbrecht, A. Salman, An overview of clustering methods, *Intell. Data Anal.* 11 (6) (2007) 583–605, <https://doi.org/10.3233/ida-2007-11602>.
- [168] P. Kumar, D. Sirohi, Comparative analysis of FCM and HCM algorithm on Iris data set, *Int. J. Comput. Appl.* 5 (2) (2010) 33–37, <https://doi.org/10.5120/888-1261>.
- [169] A.K. Jain, Data clustering: 50 years beyond K-means, *Pattern Recognit. Lett.* 31 (8) (2010) 651–666, <https://doi.org/10.1016/j.patrec.2009.09.011>.
- [170] A. Kumar, S. Kumar, Density based initialization method for K-means Clustering algorithm, *Int. J. Intell. Syst. Appl.* 9 (10) (2017) 40–48, <https://doi.org/10.5815/ijisa.2017.10.05>.
- [171] A. Likas, N. Vlassis, J.J. Verbeek, The global k-means clustering algorithm, *Pattern Recognit.* 36 (2) (2003) 451–461, [https://doi.org/10.1016/S0031-3203\(02\)00060-2](https://doi.org/10.1016/S0031-3203(02)00060-2).
- [172] R. Saha, M.T. Tariq, M. Hadi, Y. Xiao, Pattern recognition using clustering analysis to support transportation system management, operations, and modeling, *J. Adv. Transp.* 2019 (2019), <https://doi.org/10.1155/2019/1628417>.
- [173] A. Aksac, T. Özyer, R. Alhajj, CutESC: cutting edge spatial clustering technique based on proximity graphs, *Pattern Recognit.* 96 (2019), 106948, <https://doi.org/10.1016/j.patcog.2019.06.014>.
- [174] J. Qi, Y. Yu, L. Wang, J. Liu, Y. Wang, An effective and efficient hierarchical K-means clustering algorithm, *Int. J. Distrib. Sens. Networks* 13 (8) (2017) 1–17, <https://doi.org/10.1177/1550147717728627>.
- [175] V.P. Murugesan, P. Murugesan, A new initialization and performance measure for the rough k-means clustering, *Soft Comput.* 24 (15) (2020) 11605–11619, <https://doi.org/10.1007/s00500-019-04625-9>.
- [176] H. Chan, M. Cherukara, T.D. Loeffler, B. Narayanan, S.K.R.S. Sankaranarayanan, Machine learning enabled autonomous microstructural characterization in 3D samples, *Comput. Mater.* 6 (2020) 1, <https://doi.org/10.1038/s41524-019-0267-z>.
- [177] M. Daszykowski, B. Walczak, Density-Based Clustering Methods, *Compr. Chemom.* 2 (2009) 635–654, <https://doi.org/10.1016/B978-044452701-1.00067-3>.
- [178] J. Schneider, J. Kuntsche, S. Schula, F. Schneider, *Glasbau*.
- [179] G. Sedlacek, K. Blank, W. Laufs, J. Güssgen, Glass in structural engineering: Brochure, Berlin: Verlag: Ernst & Sohn 1999., Berlin: Verlag: Ernst & Sohn, p. 220, 1999.
- [180] A. Cecen, H. Dai, Y.C. Yabansu, S.R. Kalidindi, L. Song, Material structure-property linkages using three-dimensional convolutional neural networks, *Acta Mater.* 146 (2018) 76–84, <https://doi.org/10.1016/j.actamat.2017.11.053>.
- [181] R. Liu, Y.C. Yabansu, A. Agrawal, S.R. Kalidindi, A.N. Choudhary, Machine learning approaches for elastic localization linkages in high-contrast composite materials, *Integr. Mater. Innov.* 4 (1) (2015) 192–208, <https://doi.org/10.1186/s40192-015-0042-z>.
- [182] Y. Wang, et al., Stressnet: Deep learning to predict stress with fracture propagation in brittle materials, *arXiv* (2020) 1–10, <https://doi.org/10.1038/s41529-021-00151-y>.
- [183] K. Wang, W. Sun, A multiscale multi-permeability poroplasticity model linked by recursive homogenizations and deep learning, *Comput. Methods Appl. Mech. Engrg.* 334 (2018) 337–380, <https://doi.org/10.1016/j.cma.2018.01.036>.
- [184] H. Liu, Z. Fu, Y. Li, N.F.A. Sabri, M. Bauchy, Parameterization of empirical forcefields for glassy silica using machine learning, *MRS Commun.* 9 (2) (2019) 593–599, <https://doi.org/10.1557/mrc.2019.47>.
- [185] H. Liu, Z. Fu, Y. Li, N.F.A. Sabri, M. Bauchy, Balance between accuracy and simplicity in empirical forcefields for glass modeling: Insights from machine learning, *J. Non. Cryst. Solids* 515 (January) (2019) 133–142, <https://doi.org/10.1016/j.jnoncrysol.2019.04.020>.
- [186] P. Bukieda, K. Lohr, J. Meiberg, B. Weller, Study on the optical quality and strength of glass edges after the grinding and polishing process, *Glas. Struct. Eng.* 5 (3) (2020) 411–428, <https://doi.org/10.1007/s40940-020-00121-x>.
- [187] M. Engelmann, B. Weller, Residual load-bearing capacity of spanglglass-beams: effect of post-tensioned reinforcement, *Glas. Struct. Eng.* 4 (1) (2019) 83–97, <https://doi.org/10.1007/s40940-018-0079-4>.
- [188] H. Liu, et al., Predicting the dissolution kinetics of silicate glasses by topology-informed machine learning, *npj Mater. Degrad.* 3 (1) (2019), <https://doi.org/10.1038/s41529-019-0094-1>.
- [189] N.M. Anoop Krishnan, S. Mangalathu, M.M. Smedskjaer, A. Tandia, H. Burton, M. Bauchy, Predicting the dissolution kinetics of silicate glasses using machine learning, *J. Non. Cryst. Solids* 487 (February) (2018) 37–45, <https://doi.org/10.1016/j.jnoncrysol.2018.02.023>.
- [190] D.R. Cassar, A.C.P.L.F. de Carvalho, E.D. Zanotto, Predicting glass transition temperatures using neural networks, *Acta Mater.* 159 (2018) 249–256, <https://doi.org/10.1016/j.actamat.2018.08.022>.
- [191] K. Yang, et al., Predicting the Young's modulus of silicate glasses using high-throughput molecular dynamics simulations and machine learning, *Sci. Rep.* 9 (1) (2019) 1–11, <https://doi.org/10.1038/s41598-019-45344-3>.
- [192] N. Mascaraque, M. Bauchy, M.M. Smedskjaer, Correlating the network topology of oxide glasses with their chemical durability, *J. Phys. Chem. B* 121 (5) (2017) 1139–1147, <https://doi.org/10.1021/acs.jpcb.6b11371>.
- [193] N. Mascaraque, M. Bauchy, J.L.G. Pierro, S.J. Rzoska, M. Bockowski, M. M. Smedskjaer, Dissolution kinetics of hot compressed oxide glasses, *J. Phys. Chem. B* 121 (38) (2017) 9063–9072, <https://doi.org/10.1021/acs.jpcb.7b04535>.
- [194] L.G. Hwa, K.J. Hsieh, L.C. Liu, Elastic moduli of low-silica calcium aluminosilicate glasses, *Mater. Chem. Phys.* 78 (1) (2003) 105–110, [https://doi.org/10.1016/S0252-0584\(02\)00331-0](https://doi.org/10.1016/S0252-0584(02)00331-0).
- [195] T. Rouxel, Elastic properties and short-to medium-range order in glasses, *J. Am. Ceram. Soc.* 90 (10) (2007) 3019–3039, <https://doi.org/10.1111/j.1551-2916.2007.01945.x>.
- [196] J.F. Lutsko, Generalized expressions for the calculation of elastic constants by computer simulation, *J. Appl. Phys.* 65 (8) (1989) 2991–2997, <https://doi.org/10.1063/1.342716>.
- [197] R.J. Eagan, J.C. Swareengen, Effect of composition on the mechanical properties of Aluminosilicate and Borosilicate Glasses, *J. Am. Ceram. Soc.* 61 (1–2) (1978) 27–30.
- [198] E.D. Cubuk, et al., Identifying structural flow defects in disordered solids using machine-learning methods, *Phys. Rev. Lett.* 114 (10) (2015) 1–5, <https://doi.org/10.1103/PhysRevLett.114.108001>.
- [199] D.M. Sussman, S.S. Schoenholz, E.D. Cubuk, A.J. Liu, Disconnecting structure and dynamics in glassy thin films, *Proc. Natl. Acad. Sci. U. S. A.* 114 (40) (2017) 10601–10605, <https://doi.org/10.1073/pnas.1703927114>.
- [200] H. Liu, Z. Fu, Y. Li, F.A. Sabri, M. Bauchy, Machine learning forcefield for silicate glasses, *arXiv* (2019) 1–18.
- [201] A.P. Bartók, J. Kermode, N. Bernstein, G. Csányi, Machine learning a general-purpose interatomic potential for silicon, *Phys. Rev. X* 8 (4) (2018) 41048, <https://doi.org/10.1103/PhysRevX.8.041048>.
- [202] V.L. Deringer, G. Csányi, Machine learning based interatomic potential for amorphous carbon, *Phys. Rev. B* 95 (9) (2017) 1–15, <https://doi.org/10.1103/PhysRevB.95.094203>.
- [203] S. Agnelli, Strength on cut edge and ground edge glass beams with the failure analysis method, *Frat. ed Integrita Strutt.* 26 (2013) 31–40, <https://doi.org/10.3221/IGF-ESIS.26.04>.
- [204] J.B. Ward, Analysis of glass fractures, *Mater. Des.* 8 (2) (1987) 100–103, [https://doi.org/10.1016/0261-3069\(87\)90114-2](https://doi.org/10.1016/0261-3069(87)90114-2).
- [205] M. Vandebroek, J. Belis, C. Louter, G. Van Tendeloo, Experimental validation of edge strength model for glass with polished and cut edge finishing, *Eng. Fract. Mech.* 96 (2012) 480–489, <https://doi.org/10.1016/j.engfracmech.2012.08.019>.
- [206] D.S. Brauer, C. Rüssel, J. Kraft, Solubility of glasses in the system $P_2O_5\text{-CaO}\text{-MgO}\text{-Na}_2O\text{-TiO}_2$: Experimental and modeling using artificial neural networks, *J. Non. Cryst. Solids* 353 (3) (2007) 263–270, <https://doi.org/10.1016/j.jnoncrysol.2006.12.005>.
- [207] J. Lee Rodgers, W. Alan Nice Wander, Thirteen ways to look at the correlation coefficient, *Am. Stat.* 42 (1) (1988) 59–66, <https://doi.org/10.1080/00031305.1988.10475524>.
- [208] J. C. Tandia, A. Onbasli, M.C. Mauro, Machine learning for glass modeling, in: L. Musgraves, J.D., Hu, J., Calver (Eds.) *Springer Handbook of Glass*, Berlin: Springer, 2019, pp. 1157–1192.
- [209] J. Hill, G. Mulholland, K. Persson, R. Seshadri, C. Wolverton, B. Meredig, Materials science with large-scale data and informatics: Unlocking new opportunities, *MRS Bull.* 41 (5) (2016) 399–409, <https://doi.org/10.1557/mrs.2016.93>.
- [210] D.R. Cassar, ViscNet: Neural network for predicting the fragility index and the temperature-dependency of viscosity, *Acta Mater.* 206 (2021), 116602, <https://doi.org/10.1016/j.actamat.2020.116602>.
- [211] J.D. Vienna, J.J. Neeway, J.V. Ryan, S.N. Kerisit, “Impacts of glass composition, pH, and temperature on glass forward dissolution rate, *npj Mater. Degrad.* 2 (1) (2018) 1–12, <https://doi.org/10.1038/s41529-018-0042-5>.
- [212] P. Frugier, C. Martin, I. Ribet, T. Advocat, S. Gin, The effect of composition on the leaching of three nuclear waste glasses: R7T7, AVM and VRZ, *J. Nucl. Mater.* 346 (2–3) (2005) 194–207, <https://doi.org/10.1016/j.jnucmat.2005.06.023>.
- [213] I. Pignatelli, A. Kumar, M. Bauchy, G. Sant, Topological control on silicates’ dissolution kinetics, *Langmuir* 32 (18) (2016) 4434–4439, <https://doi.org/10.1021/acs.langmuir.6b00359>.
- [214] T. Oey, et al., Rate controls on silicate dissolution in cementitious environments, *RILEM Tech. Lett.* 2 (2017) 67–73, <https://doi.org/10.21809/rilemttechlett.2017.35>.

- [215] E. Aragues, I. Gilboa, A. Postlewaite, D. Schmeidler, Accuracy vs. Simplicity: a complex trade-off, SSRN Electron. J. (2005), <https://doi.org/10.2139/ssrn.332382>.
- [216] A. Makishima, J.D. Mackenzie, Direct Calculation of Young's Modulus of Glass, *J. Non. Cryst. Solids* 12 (1973) 35–45.
- [217] K.D. Koshigan, et al., Structure-property relationships from universal signatures of plasticity in disordered solids, *Glas. Mater.* 1037 (November) (2017) 1033–1037.
- [218] T.M. Gross, M. Tomozawa, A. Koike, A glass with high crack initiation load : Role of fictive temperature-independent mechanical properties, *J. Non. Cryst. Solids* 355 (9) (2009) 563–568, <https://doi.org/10.1016/j.jnoncrysol.2009.01.022>.
- [219] S. Inaba, S. Oda, K. Morinaga, Equation for estimating the thermal diffusivity, specific heat and thermal conductivity of oxide glasses, *J. Jpn. Inst. Met.* 65 (2001) 680–687, https://doi.org/10.2320/jinstmet1952.65.8_680.
- [220] S. Inaba, S. Todaka, Y. Ohta, K. Morinaga, Equation for estimating the Young's Modulus shear modulus and vickers hardness of aluminosilicate glasses, *J. Japan Inst. Met.* 64 (3) (2000) 177–183, https://doi.org/10.2320/jinstmet1952.64.3_177.
- [221] J.E. Shelby, Formation and properties of calcium aluminosilicate glasses, *J. Am. Ceram. Soc.* 68 (1985) 155–158, <https://doi.org/10.1111/j.1151-2916.1985.tb09656.x>.
- [222] C. Ecolivet, P. Verdier, Proprietes élastiques et indices de refraction de verres azotes, *Mat. Res. Bull.* 19 (1984) 227–231, [https://doi.org/10.1016/0025-5408\(84\)90094-1](https://doi.org/10.1016/0025-5408(84)90094-1).
- [223] C. Weigel, et al., Elastic moduli of XAlSiO₄ aluminosilicate glasses: effects of charge-balancing cations, *J. Non. Cryst. Solids* 447 (2016) 267–272, <https://doi.org/10.1016/j.jnoncrysol.2016.06.023>.
- [224] Y.L.J. Rocherulle, C. Ecolivet, M. Poulaïn, P. Verdier, Elastic moduli of oxynitride glasses: extension of Makishima and Mackenzie's theory, *J. Non. Cryst. Solids* 108 (1989) 187–193.
- [225] N.P. Company, A. Glasses, Coordination number of aluminum ions in alkali-free aluminosilicate glasses, *J. Non. Cryst. Solids* 52 (1982) 217–226, [https://doi.org/10.1016/0022-3093\(82\)90297-6](https://doi.org/10.1016/0022-3093(82)90297-6).
- [226] S. Sugimura, S. Inaba, H. Abe, K. Morinaga, Compositional Dependence of Mechanical Phosphate Properties Glasses in Aluminosilicate, Borate and of Applied Science for Electronics and Materials, Interdisciplinary Graduate of Engineering Science, Kyushu University, Fukuoka 816–8580 of Engineering, *J. Ceram. Soc. Jpn.* 110 (2002) 1103–1106, <https://doi.org/10.2109/jcersj.110.1103>.
- [227] S.S. Schoenholz, E.D. Cubuk, D.M. Sussman, E. Kaxiras, A.J. Liu, A structural approach to relaxation in glassy liquids, *Nat. Phys.* 12 (5) (2016) 469–472, <https://doi.org/10.1038/nphys3644>.
- [228] S.S. Schoenholz, Combining machine learning and physics to understand glassy systems, *J. Phys. Conf. Ser.* 1036 (1) (2018), <https://doi.org/10.1088/1742-6596/1036/1/012021>.
- [229] M. Hellström, J. Behler, Neural network potentials in materials modeling, *Handb. Mater. Model.* (2018) 1–20, https://doi.org/10.1007/978-3-319-42913-7_56-1.
- [230] J. R. Shewchuk, An Introduction to the Conjugate Gradient Method without the Agonizing Pain, 1994. [Online]. Available: <https://www.cs.cmu.edu/~quake-papers/painless-conjugate-gradient.pdf>.
- [231] P.I. Frazier, J. Wang, Bayesian optimization for materials design, in: T. Lookman, Francis J. Alexander, K. Rajan (Eds.) *Information Science for Materials Discovery and Design*, vol. 225, no. 45–75, Cham: Springer International Publishing AG Switzerland, 2016.
- [232] C.E. Rasmussen, C.K.I. Williams, *Adaptive Computation and Machine Learning*, vol. 7, no. 5. MIT Press, 2006.
- [233] M. Ilguth, C. Schuler, Bucak, The effect of optical anisotropies on building glass façades and its measurement methods, *Front. Archit. Res.* 4 (2) (2015) 119–126, <https://doi.org/10.1016/j.foar.2015.01.004>.
- [234] M. Schuster, J. Schneider, T.A. Nguyen, Investigations on the execution and evaluation of the Pummel test for polyvinyl butyral based interlayers, *Glas. Struct. Eng.* 5 (3) (2020) 371–396, <https://doi.org/10.1007/s40940-020-00120-y>.
- [235] A.A.Z. Nordfeldt, The aspect of the human bias in decision making within quality management systems & LEAN Theory, *Int. J. Psychol. Behav. Sci.* 7 (12) (2013) 2536–2541.
- [236] W. Beckmann, R. Knackstedt, Process for the production of modified, partially acetalized polyvinyl alcohol films, 4, 144, 1979.
- [237] C.J. Wilkinson, Q. Zheng, L. Huang, J.C. Mauro, “Topological constraint model for the elasticity of glass-forming systems, *J. Non-Crystalline Solids* X 2 (December 2018) (2019), <https://doi.org/10.1016/j.nocx.2019.100019>.
- [238] Y. Shi, A. Tandia, B. Deng, S.R. Elliott, M. Bauchy, Acta Materialia Revisiting the Makishima à Mackenzie model for predicting the young 's modulus of oxide glasses, *Acta Mater.* 195 (2020) 252–262, <https://doi.org/10.1016/j.actamat.2020.05.047>.
- [239] F. Ensslen, S. Müller-Braun, Kantfestigkeit von Floatglas in Abhängigkeit von wesentlichen Schneidprozessparametern, *Ce/Papers* 1 (1) (2017) 189–202, <https://doi.org/10.1002/cepa.20>.
- [240] S. Yoshida, Indentation deformation and cracking in oxide glass –toward understanding of crack nucleation, *J. Non-Crystalline Solids* X 1 (2019), 100009, <https://doi.org/10.1016/j.nocx.2019.100009>.
- [241] K. Asai, S. Yoshida, A. Yamada, J. Matsuoka, A. Errapart, C.R. Kurkjian, Microphotoelastic evaluation of indentation-induced stress in glass, *Mater. Trans.* 60 (8) (2019) 1423–1427, <https://doi.org/10.2320/matertrans.MD201903>.
- [242] P. Geurts, D. Ernst, L. Wehenkel, Extremely randomized trees, *Mach. Learn.* 63 (1) (2006) 3–42, <https://doi.org/10.1007/s10994-006-6226-1>.
- [243] S. Müller-Braun, M. Seel, M. König, P. Hof, J. Schneider, M. Oechsner, Cut edge of annealed float glass: crack system and possibilities to increase the edge strength by adjusting the cutting process, *Glas. Struct. Eng.* 5 (1) (2020) 3–25, <https://doi.org/10.1007/s40940-019-00108-3>.
- [244] O. Russakovsky, et al., ImageNet large scale visual recognition challenge, *Int. J. Comput. Vis.* 115 (3) (2015) 211–252, <https://doi.org/10.1007/s11263-015-0816-y>.
- [245] K. Guo, Z. Yang, C.-H. Yu, M.J. Buehler, Artificial intelligence and machine learning in design of mechanical materials, *Mater. Horizons* (2021), <https://doi.org/10.1039/d0mh01451f>.
- [246] O. Ronneberger, P. Fischer, T. Brox, U-Net: Convolutional Networks for Biomedical Image Segmentation, in: H. Taniguchi, N. Kohira, T. Ohnishi, H. Kawahira, M. von und zu Fraunberg, J. E. Jääskeläinen, M. Hauta-Kasari, Y. Iwadate, H. Haneishi (Eds.) *Lecture Notes in Computer Science (including subseries Lecture Notes in Artificial Intelligence and Lecture Notes in Bioinformatics)*, vol. 9351, Springer International Publishing Switzerland, 2015, pp. 234–241.